POLITECNICO
MILANO 1863

SCUOLA DI INGEGNERIA INDUSTRIALE
E DELL'INFORMAZIONE

EXECUTIVE SUMMARY OF THE THESIS

Joule-Brayton Pumped Thermal Electricity Storage based on packed beds

TESI MAGISTRALE IN ENERGY ENGINEERING – INGEGNERIA ENERGETICA

AUTHOR: SIMONE SAVA'

ADVISOR: PAOLO CHIESA

ACADEMIC YEAR: 2020-2021

1 Introduction

The higher penetration of renewable sources poses a significant challenge in shifting the provision of a base-load electricity generation to an intermittent one and thus on the energy network stability. This calls for highly flexible, low-cost, energy and resource-efficient energy storage technologies. The emerging Pumped Thermal Electricity Storage (PTES) technology provides a potentially low-cost and site-independent solution for electricity storage from medium to large scale. In this context, a first attempt is made to investigate the cyclic dynamic behaviour of the Joule–Brayton PTES system shown in Figure 1. The plant operates as a heat pump during the charge phase, converting electricity into high-grade thermal power, stored in the Hot Reservoir (HR) packed bed. The recovering of the pressure rise is done by the use of an expander. The cold gas will be sent to a cold reservoir (CR) packed bed to recover the low temperature produced by the expansion. During the discharge phase, the plant operates as a heat engine, powered by the Joule-Brayton cycle, with the HR and CR acting as primary hot and cold sinks.

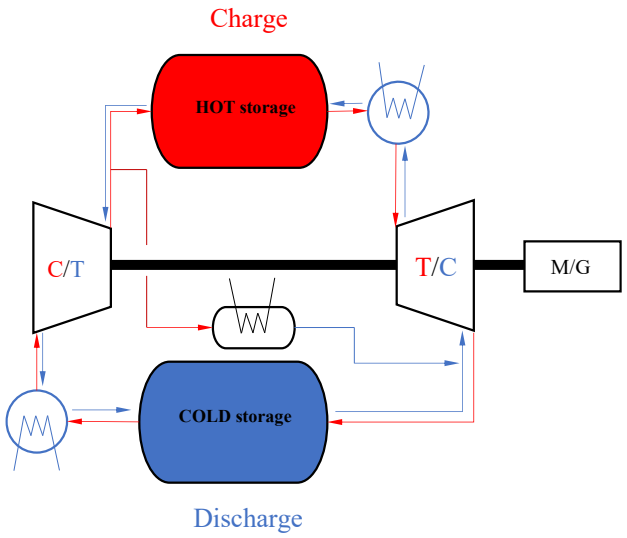

Figure 1: Plant layout during charge

The two additional heat exchangers are used to dissipate the irreversibility of compression and expansion, stabilizing the system over time. The

BV instead is employed to maintain the pressure constant at the inlet of the compressor, compensating for the mass variation in the system. In particular, a 16 MW/5h charge 2h discharge system is treated with a dynamic analysis method for the coupling of the dynamics, heat transfer and thermodynamics of the components for a complete charge and discharge cycle. The focus will be on the influencing mechanism of the main design parameters, and the optimization of the selected configuration.

1.1 Performance parameters of ES systems

The following parameters are the most important and useful to assess the performance of a PTES and, in general, for all the energy storage systems:
Round-Trip Efficiency (RTE): defined as the ratio between the energy produced during discharge and the energy absorbed during charge. It is the most important performance index, and it represents the overall efficiency of the storage system.

$$RTE = \frac{E_{el,disch}}{E_{el,ch}} \tag{1.1}$$

Work Ratio (WR): defined as the ratio between expansion work and compression work, which can be computed for both charge and discharge periods. Having high work ratios enables the installation of smaller machines and the achievement of a higher RTE for the same power requirement.

$$WR = \frac{w_C}{w_E} \tag{1.2}$$

Energy and Power density (ρ_E, ρ_P): The maximization of such parameters decreases the specific cost per unit of energy stored and per unit of power capacity. Energy density is defined as the ratio between the maximum (nominal) electrical energy that can be delivered by the expander during discharge and the total volume of the storage system (kWh/m^3). The power density instead, is defined as the ratio between the maximum (nominal) power delivered by the system and the maximum volumetric flow rate of the working fluid, which is computed at the outlet of the turbine during discharge (kW/m^{3}s^{-1} or kJ/m^3).

$$\rho_E = \frac{E_{el,disch}}{V_{tot}}, \quad \rho_P = \frac{\dot{W}_{max,disch}}{\dot{V}_{max,disch}} \tag{1.3}$$

Considering first the ideal reversible cycle, both the energy and power density are monotonically increasing functions of the temperature ratio λ (isentropic temperature ratio of the compressor), which depends on the pressure ratio and the isentropic index (γ) of the gas. It is for this reason that a monoatomic gas like Argon is proposed as the working fluid rather than Air, since the same value of λ can be achieved at a lower pressure ratio due to Argon's higher isentropic index [1].

2 Steady-state analysis

A first analysis, even if still simplified, is performed to provide the baseline design parameters used in the subsequent section (4). The assumptions for the analysis are:

- Steady-state operation, which implies no mass imbalance in the bed (no BV employed)
- Constant gas temperature at the outlet of HXs
- Ideal heat transfer between solid and working gas
- Pressure losses accounted for HXs and reservoirs

The main design parameters, which characterize and influence the overall performance of the system are: working gas flow rate (both charge and discharge), isentropic efficiency of the machines, pressure ratio, particle diameter and void fraction. Once selected the geometry of the tanks, the filler material and the outlet temperature of the heat exchangers (typically the ambient one), all the thermodynamic quantities can be computed. Regarding the filler material, to minimize the storage volume, high density and high heat capacity per unit of mass, as well as thermal stability and price are key parameters for a good storage media. For these reasons, the filler selected is Basalt in spherical pebbles. The properties of the material are listed in Table 1.

Table 1: Basalt properties [2]

Filler	Basalt	-
ϱ_s	3011	kg/m^3
k_s	1.5	W/mK

Only the specific heat capacity is found to depend heavily on temperature:

$$\begin{cases} C_S = 0.2681 + 0.001519T \quad [100 - 400\ K] \\ C_S = 2.337 + 22020/T^2 - 29{,}76/T^{0.5} \quad [400 - 1000\ K] \end{cases} \tag{2.1}$$

Only for this section, an average value between the maximum and minimum temperature in each of the storage tanks (cold and hot) is considered, respectively 950 /550 J/kgK for the HR and CR. The numerical calculation routine is iterative since the pressure losses within the tanks are dependent on the thermophysical properties of the gas.

Method

The Argon mass flow rate is considered constant in each point of the system and different from charge to discharge cycle to gain the specified discharge time, once the storage volume is fixed.

$$\dot{m}_{disch} = \frac{(1-\varepsilon)c_s\rho_s\left(T_{out,bed} - T_{in,bed}\right)V_{tank}}{\left(H_{out,bed} - H_{in,bed}\right)t_{disch}} \quad (2.2)$$

The minimum pressure of the system is set to 1.05 bar. Compressor and turbine thermodynamic transformation are considered by the adiabatic irreversible process, described by the value of isentropic efficiency. The minimum storage volume for cold and hot TES is defined from the energy balance between gas and solid:

$$V_{min} = \frac{\dot{m}\left(H_{out,bed} - H_{in,bed}\right)t_{ch}}{(1-\varepsilon)\overline{c_s\rho_s}\left(T_{out,bed} - T_{in,bed}\right)} \quad (2.3)$$

The volume computed is the minimum because it is referred to an ideal heat transfer between solid and gas (no temperature difference). The total storage volume is divided into N parallel tanks, 6 for the CR and 4 for the HR, to increase reliability and to limit pressure drops. This model assumes no temperature difference between the solid sphere and the working fluid, so the gas temperature in the outlet section of the bed equals the initial temperature of the solid bed. Heat exchangers are considered counter-current, able to control the outlet gas temperature (assumed equal to 25°C), with a continuous flow of water. The bed's diameter is chosen to be 4 m, to minimise the number of beds and limit pressure losses. The pressure drop in a fixed bed of uniform spherical particles is evaluated employing the semi-empirical relationship known as Ergun's law [3].

$$\frac{\Delta P}{L_{bed}} = 150\frac{(1-\varepsilon)^2}{\varepsilon^3}\frac{\mu\, u_s}{{d_p}^2} + 1.75\frac{1-\varepsilon}{\varepsilon^3}\frac{\rho_g\ {u_s}^2}{d_p} \quad (2.4)$$

Results

As the compression ratio increases, the performance indices increase, due to a considerable increase in maximum and minimum cycle temperature. As the isentropic efficiency is increased, at the same compression ratio, power density and RTE grow up. If the expander isentropic efficiency is reduced, a stronger drop in performance compared to a reduction in the compressor efficiency is noticed. This is because irreversibility in the compressor leads to a higher outlet temperature and some of the extra work required is converted to useful high-grade heat that can be stored during the charge phase. For a compression ratio higher than 20 with Argon as working fluid, considering realistic values of turbomachinery efficiency (0.87 for compressor and 0.94 for turbine), the maximum cycle temperature would exceed 820°C, while the minimum one would fall below -170°C approaching the practical maximum temperature ratio within typically achieved industrial axial flow compressor pressure ratios (i.e., up to 30) [4]. Fixing the Argon flow rate at 50 kg/s, a compression ratio of 20 to limit temperatures, a void fraction of 0.4 and a particle diameter of 5 mm, it is possible to obtain a storage system with a nominal net power absorbed in the charging phase of 16 MW(heat exchanger relative pressure drops is considered 2%). To obtain a discharge time of 2h, considering fixed storage volumes, a flow rate of 125 kg/s is required. This leads to a decrease in the expected RTE compared to the case where equal charge and discharge times are considered (5 h), bringing the RTE from an expected value of 70.35% (with 5 h charge and discharge) to 64.48%. The performance parameters with the selected configuration are in line with the one obtained by White [1] and Davenne [5] on similar plant layouts:

Table 2: Resulting parameters

PTES parameter		
HR storage volume	250	m^3
CR storage volume	475	m^3
Compression ratio	20	-
Charge time	5	h
Discharge time	2	h
Charge flow rate	50	kg/s
Discharge flow rate	125	kg/s
N° of vessels	6/4	-
D	4	m
dp	5	mm
ε	0.4	-
RTE	64.73	%
ϱE	72.56	kWh/m^3
ϱP	328.8	kJ/m^3

The higher cold tank number is mainly to reduce the flow speed and to limit pressure drop because

of the lower gas density in the CR. The storage density for the latter is notably lower so that typically the CR needs to be about twice the size; this accords with the average solid heat capacity's being roughly a factor of 2 lower compared to the one in the HR.

3 Plant modelling

Each component of the storage system is treated and discussed in this section. In comparison with the previous one, the modelling is more realistic and reliable.

Compressor model

For a given family of compressors, for which γ, inlet diameter, gas constant and geometry do not vary, and at high enough Reynolds number (>3e5), β and η_c can be correlated in terms of reduced quantities: $(\beta_C, \eta_c) = f\left(\frac{\dot{m}\sqrt{T_{T,in}}}{P_{T,in}}, \frac{n}{\sqrt{T_{T,in}}}\right)$. The performance map of axial-flow compressors displays the variation of total pressure ratio across a compressor, as a function of reduced mass flow (usually expressed as a per cent of design value) and reduced speed (nr_c). The axial flow compressor adiabatic efficiency (η_c) is represented by different islands on the performance map (Figure 4). It is reasonable, when building such a map, to assume a compressor designed to operate with a special working fluid like Argon, whose operating curve will show a similar trend as the one of an air compressor, with some difference due to the difference in the specific heat ratio. The Argon axial compressor map was built, starting from the maps available here [4]. The preliminary sizing and verification of the design adiabatic efficiency are evaluated according to a design procedure developed in Excel® proposed by the author during a bachelor project. For a more detailed description of the method, the reader can refer to here. The discharge compressor characteristics will be obtained with the same procedure mentioned before, after the discharge cycle optimization (4). The operation in off-design condition cannot be predicted with the Excel paper proposed and need to be studied separately. For sake of simplicity, according to [6], the efficiency in off-design condition (represented by the two different efficiency islands) is the nominal one reduced respectively by 3% and 5.5%.

Table 3: Charge compressor parameters

Compressor parameter	Charge	
Inlet flow rate	50	kg/s
Inlet pressure	105	kPa
Inlet temperature	25	°C
Nominal pressure ratio	20	-
Nominal speed	10500	rpm
Mean diameter	0.695	m
Number of stages	13	-
Efficiency islands	86/84/82	%
Nominal power	20.8	MW

Turbine model

Similar to the axial compressors, also for axial flow expanders of assigned geometry, given the properties of the motor fluid, a tern of values $\left(\frac{\dot{m}\sqrt{T_{T,in}}}{P_{T,in}}, \frac{n}{\sqrt{T_{T,in}}}, \beta_t\right)$ identifies operating conditions that comply with the similarity criteria. Therefore, for a compressible flow, the representation of the characteristics (work vs. flow rate) as the speed varies should be replaced by the more general representation of the characteristics: $(\beta_t, \eta_t) = f\left(\frac{\dot{m}\sqrt{T_{T,in}}}{P_{T,in}}, \frac{n}{\sqrt{T_{T,in}}}\right)$. The validation of the discharge turbine geometry and its equivalent resulting isentropic efficiency has been implemented using Axtur software, an *in-house* optimization code for axial and radial flow turbines. For a more detailed description of the software, the reader can refer to [7]. Considering the above outcomes, the characteristic curves of the expander are built, defined by the classic law of the ellipse in the compression ratio/reduced flow rate. Both the characteristic curves of the turbines in charge and discharge mode have been constructed from the graph in [8], considering the variation of the dimensionless parameters in the two phases, but maintaining the same trend (as done for the compressor).

Table 4: Chrage turbine parameters

Turbine parameter	Charge	
Inlet flow rate	50	kg/s
Inlet pressure	1950	kPa
Inlet temperature	25	°C
Expansion ratio	18.5	-
Nominal speed	10500	rpm
Mean diameter	0,34	m
Number of stages	3	-
Design efficiency	93.58	%
Nominal power	5	MW

Packed bed ideal model

During the charging or discharging process, the heat transfer zone between gas and solid, called the thermocline, moves respectively downwards or upwards inside the storage. Upstream from the thermocline, a new zone at a relatively uniform

temperature is generated. The outlet temperature of packed-bed storage is constant as long as the thermocline remains in the tank. An ideal reservoir would be one for which there are no irreversibilities due to heat transfer or fluid friction. Thermodynamic losses associated with irreversible heat transfer will be reduced using very small particles and a high heat transfer coefficient. As $h \to \infty \; and \; d_p \to 0$, the gas-solid temperature difference disappears, and the progress of the thermal front is ideal. The nominal speed of the heat front can be computed as :

$$V_n = \frac{\dot{m}\overline{cp_g}}{N_{tank}A(1-\varepsilon)\rho_s\overline{c_s}}$$

The position of the temperature wave at a time t is found by simply progressing each part of the initially discontinuous profile by a distance z = V_n t (Figure 2).

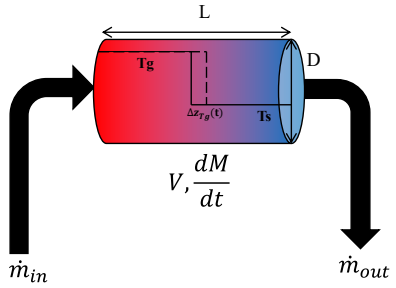

Figure 2: Ideal thermal front progression

During the charge/discharge process, a large amount of gas is stored or released in the pore volume of packed beds due to the change in gas density owing to the translation of thermocline. In the PTES system, since the HR is pressurized, its mass variation is predominant, in absolute terms. The mass variation in the packed bed certainly causes an unbalanced mass flow rate between the inflow and outflow.

$$\dot{m}_{in} - \dot{m}_{out} = \frac{h_{bed}\,\pi\,\frac{D^2}{4}[\rho_g(t) - \rho_g(t = t_0)]}{t - t_0} \qquad (3.1)$$

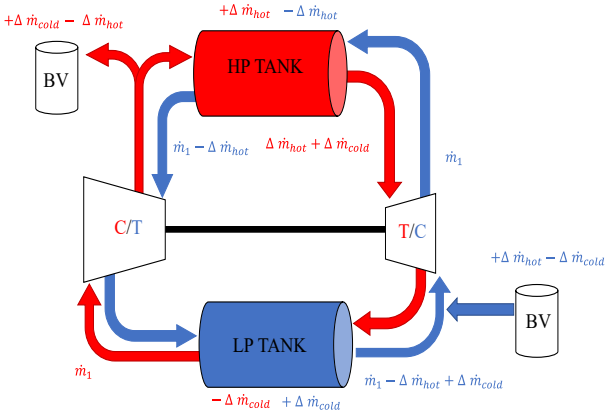

Figure 3: Flow rate scheme during charge/discharge

In closed-loop PTES systems, this implies different gas flow rates between compressor and expander [9]. The buffer vessel is required to store/release gas to stabilize the system pressure during the cycle, balancing the changes of mass in the two reservoirs, as shown in Figure 3.

Heat exchangers

Without this component, cyclic operation between charge and discharge won't be possible since the bed initial temperature will increase with respect to the design one, due to irreversible expansion and compression process during discharge. They are assumed to be counter-current. High RTEs require a gas cooler with a heat transfer efficiency > 97%. Fixing a water flow rate of 50 kg/s, and an overall heat transfer coefficient of 0.07 kW/K, it is possible to achieve overall effectiveness of 98.2% for the worst condition (turbine discharge outlet with 1.1 bar pressure) with an overall heat transfer area of 5000 m².

Turbine-compressor fluid dynamic matching

Once the design of the machines has been defined and the characteristic curves of the compressor and expander are known, it is possible to determine the operating point of the machine by solving the fluid-dynamic coupling of the components since both are placed on the same shaft. This means to evaluate the quantities (flow rates, pressures, temperatures, rotational speed) which make it possible to identify the operating point of each machine on its characteristic curve. In this case, the parallelism of the generator ensures a constant rotational speed. The characteristic curves of the turbine present a common trait characterized by the constant reduced flow rate that is realized when choking conditions are reached: $\frac{\dot{m}\sqrt{T_{T,in}}}{P_{T,in}} = K$. The determination of the equilibrium operating point of the system is done iteratively by arbitrarily fixing a point on the plane of the compressor, considering fixed rotational speed; in this way, the following parameters can be evaluated immediately : $\left(\frac{\dot{m}\sqrt{T_{T,1}}}{P_{T,1}}, \frac{N}{\sqrt{T_{T,1}}}, \beta c, \eta c\right)$. Remember that turbine and compressor inlet temperatures are constant and set by the initial condition of the tanks during the two different phases (considering the ideal thermocline). It is possible, once calculated the pressure losses of the hot storage (form thermodynamic state at compressor outlet), assuming those in the cold storage and the flow rate to/from the buffer vessel,

to report the turbine curve on the compressor plane as:

$$\beta = \frac{\dot{m}_{rid,c}(1 + (\Delta\dot{m}_{BV} - \Delta\dot{m}_{HOT,tes})/\dot{m}_1)\frac{\sqrt{T_{T,4}}}{\sqrt{T_{T,1}}}}{K(1 - \frac{\Delta P_{HOT,tes}}{P_2})} \quad (3.2)$$

In this way, it is possible to determine the value of the compression ratio that represents the only degree of freedom of the system (Figure 4). The numerical routine is iterative and considers convergence for the pressure losses values and flow rate delivered to/from the BV.

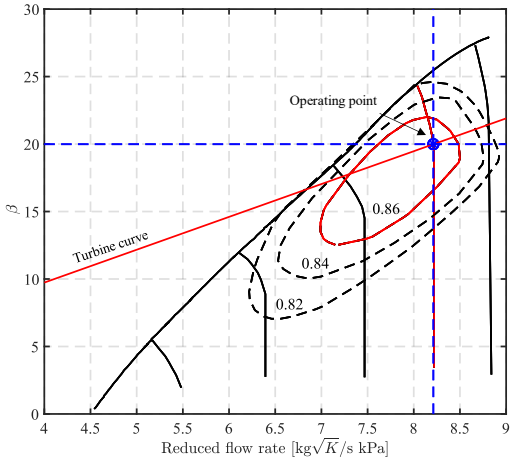

Figure 4: Compressor-turbine matching

4 Dynamic analysis

The operation of the system in dynamic regime will be analysed. After the charging process, the compression ratio of the delivery period can be reset by storing some gas in the BV. The purpose of this analysis is to investigate the behaviour of the operating parameters during the time and to set the optimum compression ratio for the discharge phase which maximises the RTE. The numerical routine is iterative and considers the convergence described for the matching between turbine and compressor.

Results

It can be found that the pressure loss in the CR decreases during the charging and increases during the discharging process, while the opposite phenomenon is observed in the case of the HR. This is because, during the charging period, the cold region in the CR grows gradually, owning to higher density which results in a decrease in the pressure loss. During the discharging process instead, the cold region retracts gradually, and the pressure loss increases. For similar reasons, the increase of the hot region in the HR leads to a higher volume flow rate, hence increasing the pressure loss during the charging and decreasing it during the delivery. The mass flow imbalance between the two machines stays always below 0.25 kg/s, and its effect on the matching between turbine and compressor is minimal. During the charge, taking into account the small pressure drop in the HR (<0.1 bar), the compression ratio (Figure 5) results rather stable, while the expansion ratio(Figure 6) increases due to a decrease in cold tank pressure drop and a slight increase in the flow processed. Similar deductions can be done for the delivery period, but with inverse trends.

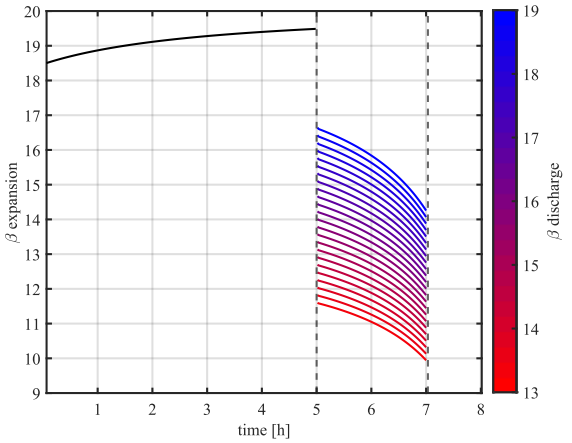

Figure 5: Expansion ratio over time

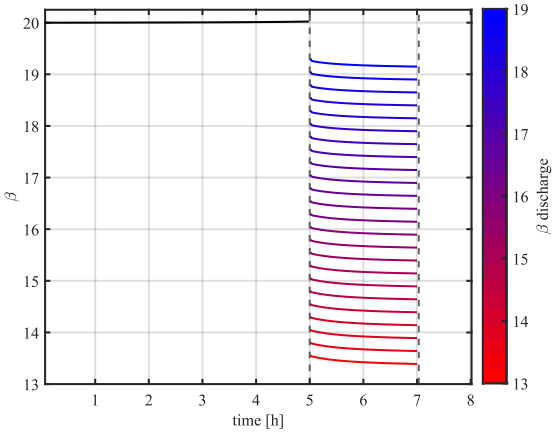

Figure 6: Compression ratio over time

Final considerations must be done regarding the RTE. An optimum efficiency can be found at a pressure ratio of 15.75 during the discharge. The shaft power to be higher compared to a compression ratio of 20, because the variation amplitude of the compression power is greater than that of the expansion power when the discharging compression ratio increases from 15.75 to 20. The unbalanced flow rate and the variation

of the pressure drops during time causes a reduction in power output during discharge, which causes a decrease in the RTE with respect to the one expected without considering the dynamic behaviour of the system. Figure 7 shows that the powers of the PTES compressor, expander and shaft are rather stable during the charging process, while, during the delivery process, the expander power decrease gradually, thus leading to a decrease in shaft power, following the pressure ratios trend. The final rating parameters are: ● RTE=62.99%; ●Average power density=326.83 kJ/m³; ● Energy density= 69.36 kWh/ m³

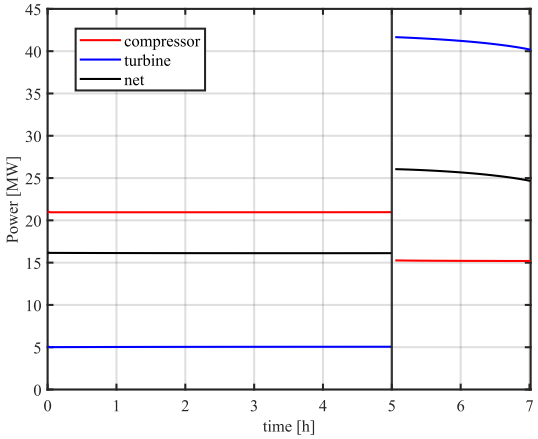

Figure 7: Power level of the PTES over time

5 Packed bed dynamic model

In this fifth chapter, the numerical model used to predict packed-bed energy storage performance is presented.

The Schumann model

The Schumann model is a reference for many authors. This one-dimensional two-phase model of heat transfer in porous media was originally developed by Schumann, 1929 [10]. It consists of two energy equations, one for the fluid and the other for the solid, linked by a convective heat exchange term. The straightforward energy balance between gas and solid gives:

$$\dot{m}_g c_{p,g} \frac{\partial T_g}{\partial z} + A\varepsilon\rho_g c_{p,g} \frac{\partial T_g}{\partial t} = hA(1-\varepsilon)\frac{6}{d_p}\left(T_s - T_g\right) \quad (5.1)$$

$$\rho_s A(1-\varepsilon) c_s \frac{\partial T_s}{\partial t} = hA(1-\varepsilon)\frac{6}{d_p}\left(T_s - T_g\right) \quad (5.2)$$

The Schumann model is valid under the following conditions: ● Negligible thermal gradient inside the solid (Bi<0.1); ●Homogeneous porous medium, ●1D system with fluid circulating according to plug-flow;●Adiabatic storage; ●Negligible diffusion compared to convection; ●Uniform HTC around the solid particles.

White numerical model

The Schumann model has been chosen for this thesis as a simplified but accurate method for gaseous fluid. Neglecting the unsteady pressure term, Schumann equations may then be expressed in the normalised form according to [11]:

$$\frac{\partial \vartheta_g}{\partial \xi} = \vartheta_s - \vartheta_g;\ \frac{\partial \vartheta_s}{\partial \eta} = \vartheta_g - \vartheta_s \quad (5.3)$$

Where $\vartheta_{g,s} = \left(T_{g,s} - T_{in,s}\right)/\left(T_{in,gas} - T_{in,s}\right)$ and ξ and Φ are the dimensionless lengths and time variables are: $\xi = \frac{z}{l}$; $\Phi = \frac{t}{\tau}$. The length and time scales used for this normalisation are, respectively: $l = \frac{\dot{m}\, c_{p,g}}{hA(1-\epsilon)S_v}$; $\tau = \frac{\rho_s c_s}{hS_v}$. The fluid/solid HTC is a key parameter that governs the thermal stratification of the storage. Regarding the determination method, the correlation of Wakao et al. [12] was developed on a large range of experimental data from different setups, is easy to implement, widely used in the literature and in the average of the other correlations.

$$Nu = 2 + 1.1\, Pr^{0.33}\, {Re_p}^{0.6}$$
$$Re_p = \frac{\rho_g u_s}{d_p}\ ,\ P_r = \frac{\mu_g c_{p,g}}{k_g}\ ,h = \frac{Nu\, k_g}{d_p} \quad (5.4)$$

Its range of validity is from Re_p between 15 and 8500 in laminar regime. The numerical method used to integrate is similar to that presented in [11] but stability and computational efficiency have been improved by employing a semi-analytical approach developed by White [13] with some modifications to decrease computational time. To build a solid numerical routine, a space and time grid is necessary to integrate the governing equations. The computational grid is shown in Figure 8.

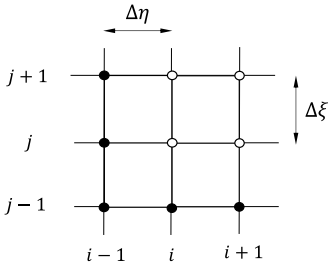

Figure 8: Computational grid; i represents the time step and j the spatial step. Temperatures are known at nodes marked with ● and unknowns at nodes market with ○

Starting from Eq. 5.3 the task is thus to obtain values of temperatures in the unknown nodes. This is achieved by integrating the first equation between nodes $(j-1\,,\,i)$ and $(j\,,\,i)$ and the second one between $(j\,,\,i-1)$ and $(j\,,\,i)$, holding Ts and Tg constant at their average values. The resulting pair of equations may be expressed in the form of a linear system. By inverting a 2x2 matrix is possible to evaluate the solid and gas temperature at node $(j\,,i)$.

$$\begin{pmatrix} 1 & 0.5\left(e^{-\Delta\xi}-1\right) \\ 0.5\left(e^{-\Delta\Phi}-1\right) & 1 \end{pmatrix}\begin{pmatrix} \vartheta_{g,j}^{i} \\ \vartheta_{s,j}^{i} \end{pmatrix} = \begin{pmatrix} 0.5\left(1-e^{-\Delta\xi}\right)\vartheta_{s,j-1}^{i}+e^{-\Delta\xi}\vartheta_{g,j-1}^{i} \\ 0.5\left(1-e^{-\Delta\Phi}\right)\vartheta_{g,j}^{i-1}+e^{-\Delta\Phi}\vartheta_{s,j}^{i-1} \end{pmatrix} \quad (5.5)$$

Generally, solutions are 'grid' independent for space and time steps less than 20% of l and τ respectively. Finally, the mass flow varies very slightly through the reservoir due to the change in the mass of stored gas brought about by the passage of the thermal front.

$$\dot{m}_{g,j}^{i}=\dot{m}_{g,j-1}^{i}+\varepsilon A\frac{\Delta z}{\Delta t}\left(\rho_{g,j}^{i-1}-\rho_{g,j}^{i}\right) \quad (5.6)$$

Model validation

The model has been validated using previously published experimental results by this group [14], on an air-based packed bed of rocks, as done also by Hänchen et al. [15]. The numerically modelled and experimentally measured gas temperature profiles across the pilot storage tank are shown in Figure 9. The correlation by Coutier et al. [16] is used to compute the HTC.

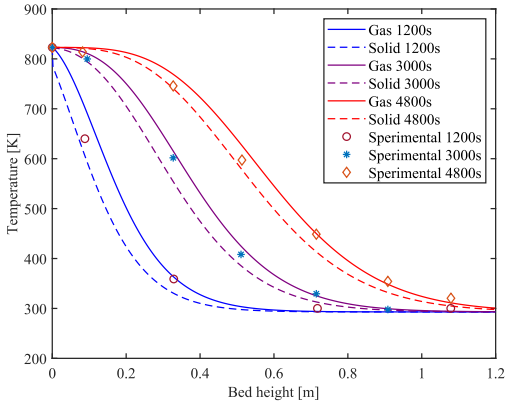

Figure 9: Model validation

Results

For the HR, during charge, the velocity of the thermal front decreases as time proceeds, leading to a change in the front length as shown in Figure 10. The wave speed depends on the solid specific heat capacity which increases with temperature and on the flow rate, which increases layer by layer. The overall effect is dominated by the specific heat capacity, which leads to a spreading of the front. The spreading is significant due to the huge difference in maximum and minimum temperature inside the reservoir itself (ΔT_{hot}=795°C) with the consequent huge increase of specific heat capacity of the solid (from 0.61 kJ/kgK to 1.2 kJ/kgK). The difference between solid and gas temperature is about 5°C due to the heat transfer characteristics of the stratified thermocline and the small particle diameter.

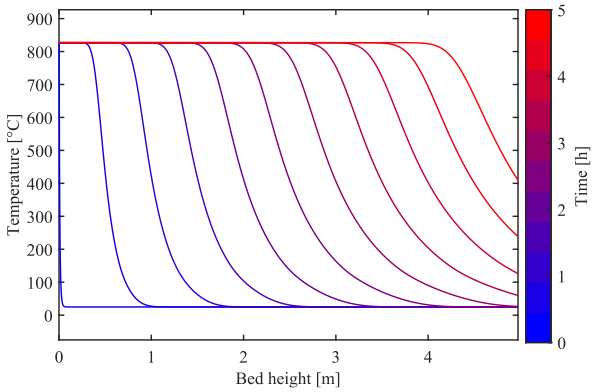

Figure 10: Gas thermal front in the HR (charge)

For the CR instead (Figure 11), the velocity of the thermal front increases during the charge, since the flow rate decreases layer by layer but the effect of the decrease in the specific heat capacity with temperature is predominant, steepening the temperature profile. The difference between solid and gas temperature profiles stays around 5°C. The thermal front is steeper than the one in HR due to the lower specific heat capacity of the solid (from 0.42 kJ/kgK to 0.61 kJ/kgK) and the smaller difference in maximum and minimum temperature inside the reservoir itself (ΔT_{cold}=201°C).

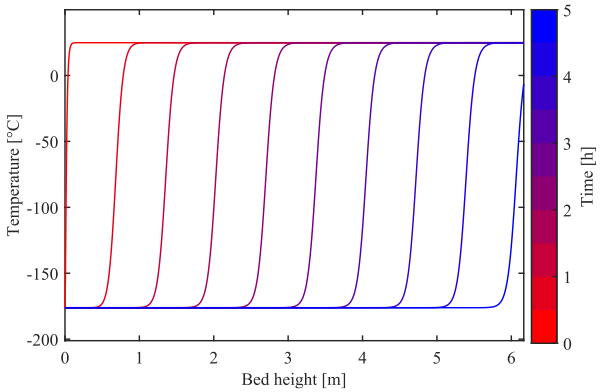

Figure 11: Gas thermal front in the CR (charge)

Table 5: Reservoirs data

Packed bed	HR	CR	
D	4	4	m
N° vessels	4	6	-
Bed height	5.1	6.3	m
$\dot{m}_{ch/disch}$	50/125	50/125	kg/s
Grid points	4000	4000	-
T_{max}	820	25	°C
T_{min}	25	-171	°C
Inlet pressure	2000	107	kPa

Parametric study

The following sub-section will evaluate the influence of different operating parameters on the thermal performance of the packed bed, including the fluid flow rate and particle diameter.

Flow rate

The nominal speed of the thermal front increases with the flow rate, decreasing the nominal time to discharge the reservoir with a fixed volume. Higher flow rates lead to better heat transfer between the two phases, but higher pressure drop inside the vessel. Regarding the HR, the temperature profiles during charge are shown in Figure 12. With the increase in the flow rate from 50 kg/s for the charge period to 125 kg/s, the overall effect is a steepening of the temperature profile minute by minute caused by the increase in the front speed and the cooling of the tank. For the CR instead (Figure 13), the overall effect is a spreading of the temperature profile minute by minute, caused by the heating of the tank and the increase in flow rate.

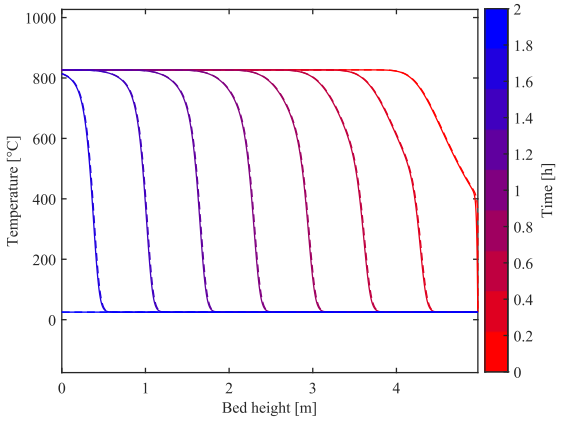

Figure 12: Thermal front steepening in HR during discharge; —— Gas temperature – – – Solid temperature

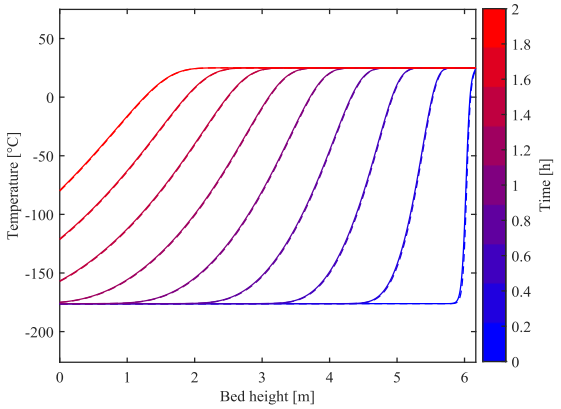

Figure 13: Thermal front spreading in CR during discharge —— Gas temperature – – – Solid temperature

Particle diameter

Figure 14 shows the temperature distributions of the solid and fluid phases across the storage height at half of the discharge cycle with different particle sizes varied in the range between 5÷20 mm.

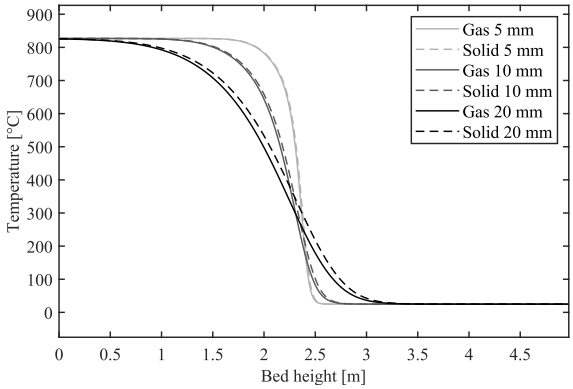

Figure 14: Temperature distributions (HR) for varying particle diameter t=1h (discharge)

Smaller particle diameter leads to a steeper temperature profile. Moreover, the difference between the solid and fluid temperature noticeably narrows for smaller particles, which is a clear indication of an improved convective heat transfer between fluid and solid. The amount of pumping work however increases significantly for small particle sizes.

6 Plant simulation with dynamic heat transfer

As far as the real thermocline is considered, a dynamic thermal instability arises during the continuous operation of the plant. When the thermocline exits the bed length, the inlet temperature of the machines changes over time.

This, combined with the effect of variation in pressure losses and flow rate described in the previous sections, causes a variation of the operating point of the machines. The configuration selected for this analysis is the optimized one obtained at the end of the dynamic analysis, so: β_{ch}=20 and β_{disch}=15.75. During the charge phase, when the thermocline exits the bed height, the inlet, and consequently the outlet temperature of the machines will increase, causing the entry of a second thermal front inside the bed, which heats up the primary part of the bed (Figure 15 and Figure 16). The charge must be stopped after 4h for two limiting technical reasons: the maximum cycle temperature would exceed 910°C and the compressor operating point would reach the pumping limit.

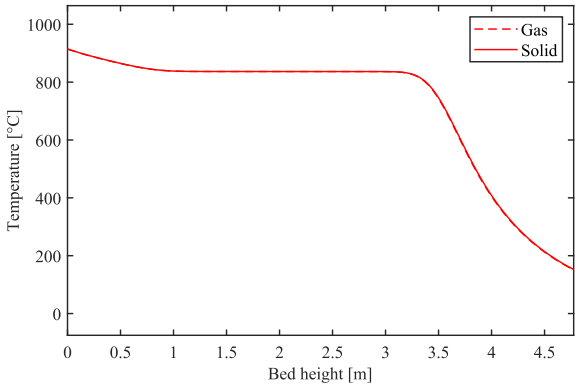

Figure 15: HR temperature profile at the end of 4h considering the real thermal front

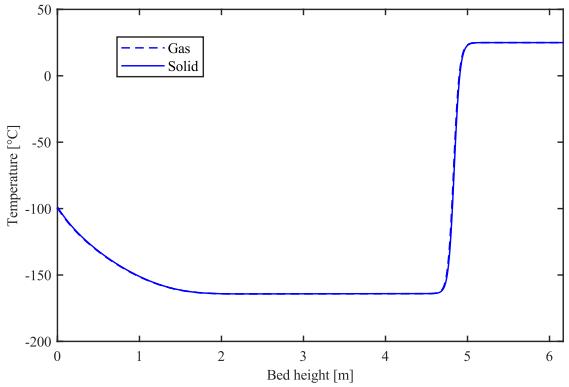

Figure 16: CR temperature profile at the end of 4h considering the real thermal front

This unstable behaviour of the outlet bed temperature will create problems during the delivery phase: first, the machines will experience (both) a decrease in the inlet temperature, until the thermal level in the bed is re-established. Then, when the front leaves the bed length, the inlet temperature of the compressor/turbine will increase/decrease. This effect influences the operating points in terms of turbine curve and compressor reduced speed, changing over time the operating point and, accordingly, the pressure, flow rate and power level (Figure 17). The overall effect is a reduction in RTE, which results in 56.3% and a consequent ϱE of 51.85 kWh/m³. Moreover, the increase of the maximum temperature of the cycle must be considered during the design procedure and the cost analysis.

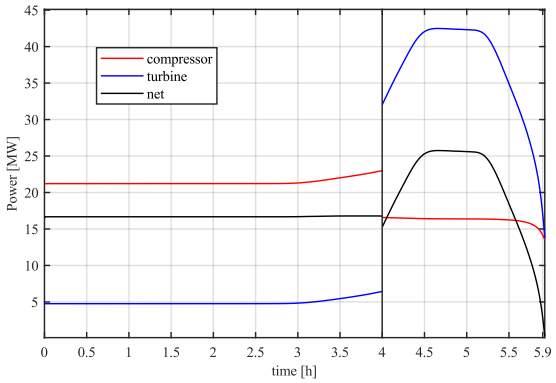

Figure 17: Power level over time

Possible solution

The two heat exchangers employed to dissipate the heat caused by the irreversibility in the delivery phase can be used to control the outlet gas temperature from the bed also during the first charge period. In this way, the system stays under thermal control, stabilizing the compressor and expander power during charge and discharge. The effect of the thermocline's exit during the discharge phase cannot be mitigated and causes a decrease in the power delivery, with a consequent decrement of the RTE. After 2.1h the power absorbed by the compressor is higher with respect to the one delivered by the turbine and the discharge phase is stopped, even if the two reservoirs do not reach the initial uniform temperature state of 25°C. This happens because two thermal fronts (in the HR and CR) are not synchronized. During the delivery phase, when the HR thermocline exits the bed, the TIT will decrease (Figure 18). As the TIT falls, the maximum pressure of the cycle decreases as well as the compression ratio and the delivering power (Figure 19). This effect is shown also in the work of Wang et al. [17]. Meanwhile, the compressor inlet temperature will increase leading to a decrease in the flow rate of Argon. The overall reduction in RTE compared to the case in which no heat exchanger is employed in the charge is lower. A

final RTE of 59.86% is achievable, with consequent energy and power density respectively 67.32 kWh/m³ and 293.16kJ/m³.

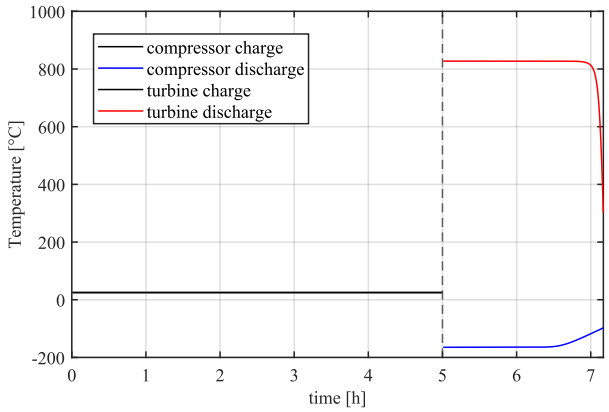

Figure 18:: Inlet temperature considering the real thermal front with charge HX

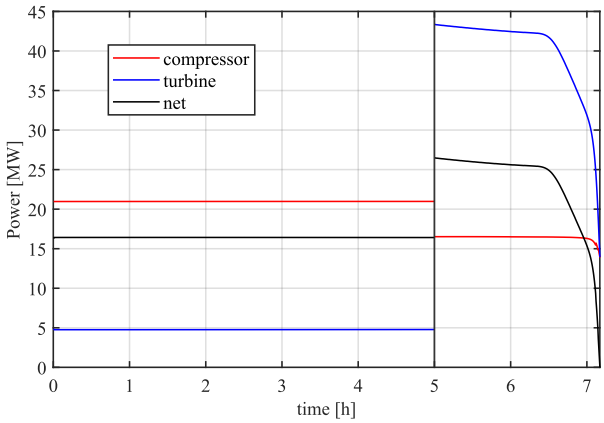

Figure 19: Power levels over time considering the real thermal front with charge HX

7 Conclusions

This thesis can provide a starting point for the design, dimensioning and optimisation of PTES systems based on the Joule Brayton cycle operating with turbomachines. The results show that these systems certainly promise high energy density (67.32 kWh/m3) with a modest RTE (59.86%), considering that the scale-up can achieve virtually any power and capacity. The model developed by the author is a flexible code, able to cope with different cycle configurations, exogenous conditions and working fluids, but results optimized to sustain one charge and discharge cycle. The outcomes of the work are:

- A model for the evaluation and optimization of discharge cycle's performance developed in MatlabR2020a®, through the fluid-dynamic turbine-compressor coupling (with relative operating maps), considering the ideal heat exchange inside the beds.
- A numerical model developed in MatlabR2020a® to predict the actual behaviour of the thermocline within the beds, in terms of temperature profiles resulting from both charging and discharging periods.
- Finally, a combination of the two models mentioned before, which accounts for the effects of real thermoclines progression on the system. Without controlling the temperature during the charge period through additional heat exchangers, the operation of the system is not sustainable over time. The discharge is affected by the heating of the primary zone of the bed at the end of the charge cycle, resulting in a RTE of 56.3% and a ϱE of 51.85 kWh/m³. The solution implemented is to add two additional heat exchangers during charge, stabilising the system for correct and continuous operation over time. However, the different thermal behaviour of the two reservoirs must be taken into account for the discharge period and continuous operation. With this configuration, the RTE, ϱE and ϱP can be brought respectively to a value of 59.86%, 64.32 kWh/m³ and 293.16kJ/m³. In any case, both RTE and energy density is lower compared to the ideal thermocline model result.
- Starting from the results of this thesis, future works could involve the analysis of different storage materials, configurations of the power cycle and working fluids, bearing in mind the issues involved. It will be necessary to analyse the system over a long time, with various charge and discharge cycles, choosing their timing in relation to the shapes of the thermoclines. Future studies may also analyse and rearrange the characteristics of the CR and HR to synchronize the two heat front over time. Last, a cost analysis may give further incentive towards some configurations over others.

8 Bibliography

[1] A. White, G. Parks, and C. N. Markides, "Thermodynamic analysis of pumped thermal electricity storage," *Appl. Therm.*

Eng., vol. 53, no. 2, pp. 291–298, 2013,

[2] M. A. Bouhifd, P. Besson, P. Courtial, C. Gérardin, A. Navrotsky, and P. Richet, "Thermochemistry and melting properties of basalt," *Contrib. to Mineral. Petrol.*, vol. 153, no. 6, pp. 689–698, 2007,

[3] S. Ergun, "Fluid flow through packed columns," *Chem. Eng. Prog.*, vol. 48, pp. 89–94, 1952.

[4] M. P. Boyce, "Axial-flow Compressors," *Gas Turbine Eng. Handb.*, p. 163, 2012, [Online]. Available: https://www.netl.doe.gov/sites/default/files/gas-turbine-handbook/2-0.pdf

[5] T. R. Davenne and B. M. Peters, "An Analysis of Pumped Thermal Energy Storage With De-coupled Thermal Stores," *Front. Energy Res.*, vol. 8, no. August, pp. 1–22, 2020,

[6] *Curve Caratteristiche delle Turbomacchine*. p. 1.

[7] M. Astolfi and E. Macchi, "Efficiency Correlations for Axial Flow Turbines Working With Non-Conventional Fluids," *Asme Orc 2015*, pp. 1–12, 2015.

[8] M. Valorani, L. Magistrale, and A. Maer, "Corso di Motori Aeronautici," 2011.

[9] L. Wang *et al.*, "Unbalanced mass flow rate of packed bed thermal energy storage and its influence on the Joule-Brayton based Pumped Thermal Electricity Storage," *Energy Convers. Manag.*, vol. 185, no. February, pp. 593–602, 2019,

[10] T. E. W. Schumann, "Heat transfer: a liquid flowing through a porous prism," *J. Franklin Inst.*, vol. 208, no. 3, pp. 405–416, 1929.

[11] J. A. Willmott, *Dynamics of regenerative heat transfer*. CRC Press, 2001.

[12] N. Wakao, S. Kaguei, and T. Funazkri, "Effect of fluid dispersion coefficients on particle-to-fluid heat transfer coefficients in packed beds: correlation of Nusselt numbers," *Chem. Eng. Sci.*, vol. 34, no. 3, pp. 325–336, 1979.

[13] A. J. White, "Loss analysis of thermal reservoirs for electrical energy storage schemes," *Appl. Energy*, vol. 88, no. 11, pp. 4150–4159, 2011,

[14] A. Meier, C. Winkler, and D. Wuillemin, "Experiment for modelling high temperature rock bed storage," *Sol. energy Mater.*, vol. 24, no. 1–4, pp. 255–264, 1991.

[15] M. Hänchen, S. Brückner, and A. Steinfeld, "High-temperature thermal storage using a packed bed of rocks - Heat transfer analysis and experimental validation," *Appl. Therm. Eng.*, vol. 31, no. 10, pp. 1798–1806, 2011,

[16] J. P. Coutier and E. A. Farber, "Two applications of a numerical approach of heat transfer process within rock beds," *Sol. Energy*, vol. 29, no. 6, pp. 451–462, 1982.

[17] L. Wang, X. Lin, L. Chai, L. Peng, D. Yu, and H. Chen, "Cyclic transient behavior of the Joule–Brayton based pumped heat electricity storage: Modeling and analysis," *Renew. Sustain. Energy Rev.*, vol. 111, no. October 2018, pp. 523–534, Sep. 2019,

Politecnico di Milano

SCHOOL OF INDUSTRIAL AND INFORMATION ENGINEERING

Master of Science – Energy Engineering

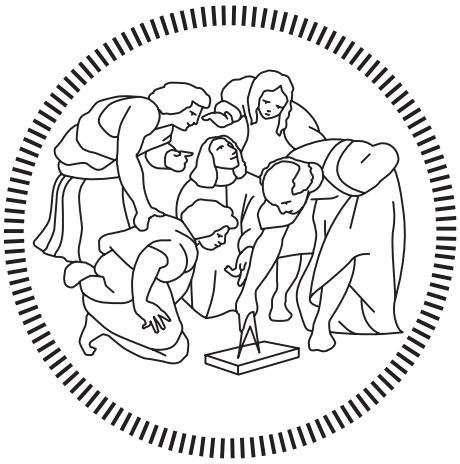

Joule-Brayton Pumped Thermal Electricity Storage based on packed beds

Supervisor

Prof. Paolo CHIESA

Co-Supervisor

Prof. Andrea GIOSTRI

Candidate

Simone SAVA' – 946402

Academic Year 2020 – 2021

Acknowledgements

Mi è doveroso dedicare questo spazio del mio elaborato alle persone che hanno contribuito, con il loro instancabile supporto, alla sua realizzazione e al raggiungimento dei miei obiettivi. In primis, un ringraziamento speciale va al mio relatore Paolo Chiesa, per la sua infinita pazienza, per i suoi indispensabili consigli e per le conoscenze trasmesse durante tutto il percorso di stesura dell'elaborato. Ringrazio la mia famiglia che ha sempre sostenuto e appoggiato in ogni mia decisione. Un grazie di cuore a Paola, che non ha mai smesso di spronarmi ed aiutarmi nei momenti difficili. Un ringraziamento speciale va anche ai miei colleghi Francesco, Federico, Salvatore e Stefano con cui ho condiviso il mio percorso universitario. Senza tutti voi non ce l'avrei fatta ad arrivare fin qui.

Grazie.

Sommario

Il Pumped Thermal Electricity Storage (PTES) ha come vantaggi un'elevata densità di energia ed una modesta efficienza, risultando quindi particolarmente adatto allo stoccaggio di energia elettrica su larga scala. Le performance del PTES hanno suscitato molta attenzione negli ultimi anni ed è stato studiato per lo più sulla base della termodinamica stazionaria, mentre la caratteristica dinamica del reale processo di stoccaggio è spesso trascurata. In questa tesi, giudicando l'efficienza di round-trip e la stabilità del processo, viene studiato il comportamento di un sistema PTES da 16 MW/5h basato su ciclo Joule-Brayton e con stoccaggio termico su letti fissi, utilizzando Argon come fluido di lavoro. Viene proposto un metodo di analisi dinamica che accoppia il matching tra compressore ed espansore con lo scambio termico all'interno dei letti, inizialmente considerato ideale ed in seguito approfondito con un modello numerico *ad hoc* che simuli il comportamento reale. Vengono anche analizzati i fattori che influenzano il sistema come il rapporto di pressione, l'efficienza isoentropica delle macchine, il diametro delle particelle e la struttura dei serbatoi di stoccaggio. I risultati di questa analisi indicano che il sistema Argon PTES può raggiungere fino al 60% di RTE e, attraverso ulteriori studi e miglioramenti, questo valore può essere aumentato ulteriormente. L'aumento del rapporto di pressione e delle efficienze isentropiche migliorano notevolmente le prestazioni di immagazzinamento dell'energia, poiché il ciclo termodinamico migliora ad un livello di temperatura più alto, aumentando però di conseguenza il costo specifico dell'impianto. Valori ottimali del rapporto di compressione in fase di scarica possono essere impostati per massimizzare l'efficienza di round-trip, così come il diametro delle particelle e la geometria dei serbatoi, una volta fissate le dimensioni del sistema (potenza ed energia richieste) e il tempo di carica e scarica. Questa tesi può fornire una base per la progettazione e il funzionamento ottimale di un PTES basato su ciclo Joule-Brayton.

Abstract

Pumped Thermal Electricity Storage (PTES) has the advantages of high energy density and moderate efficiency, making it particularly suitable for large-scale electricity storage. The performance of PTES has attracted much attention in recent years, and it has mostly been studied based on stationary thermodynamics, while the transient characteristic of the actual storage process is often neglected. In this thesis, evaluating the round-trip efficiency and stability of the system, the behaviour of a 16 MW/5h PTES system based on the Joule-Brayton cycle and with thermal storage on packed beds is studied, using Argon as working fluid. A dynamic analysis method is proposed that couples the matching between compressor and expander with the heat exchange inside the beds, initially considered ideal and then investigated with an *ad hoc* numerical model that simulates the real behaviour. The factors influencing the system such as the pressure ratio, the isentropic efficiency of the machines, the diameter of the particles and the structure of the thermal storage tanks are also analysed. The results of this analysis indicate that the Argon PTES system can achieve up to 60% of RTE and, through further studies and improvements, this value can be increased even further. Increasing the pressure ratio and isentropic efficiencies significantly improves energy storage performance, as the thermodynamic cycle improves at higher temperature levels, but the specific cost of the system increases too. The optimal compression ratio during discharge can be set to maximise round-trip efficiency as well as, particle size and reservoir diameter, once the system size (power and energy required) and charging and discharging time are fixed. This thesis can provide a basis for the optimal design and operation of a PTES based on the Joule-Brayton cycle.

Table of Contents

List of Figures

List of Tables

1 Outlines

The 2050 net-zero carbon economy requires a much higher penetration of renewable sources (RES) into the energy system [1]. This poses a significant challenge in shifting the provision of a base-load electricity generation to an intermittent one and thus on the energy network stability. This calls for highly flexible, low-cost, energy and resource-efficient storage technologies to balance the energy supply and demand mismatch. Among the storage technology options, the emerging Carnot Battery (or Pumped Thermal Electricity Storage) technology provides a potentially low-cost and site-independent solution for electricity storage from medium to large scale. Carnot Batteries work by transforming electricity into thermal energy, storing the thermal energy in inexpensive media (e.g. rocks, molten salts), which can be converted back to electricity when required. In this context, a first attempt is made to investigate the behaviour of the Joule–Brayton PTES system shown in Fig. 1.1. The plant operates as a heat pump during the charge phase, employing a compressor to convert electricity into high-grade thermal power, stored in the Hot Reservoir (HR). The recovering of the pressure rise is done by the use of an expander. The cold gas will be sent to a Cold Reservoir (CR) to recover the low temperature produced by the expansion. During the delivery or discharge phase, the plant operates as a heat engine, powered by the Joule-Brayton cycle, with the HR and CR acting as primary hot and cold sinks. Two Heat exchangers (HX) are employed to dissipate the heat generated by irreversibilities during compression/expansion, for the cyclic operation of the system. In particular, a 16 MW/5h charge 2h discharge system is treated with a dynamic analysis method for the coupling of the dynamics, heat transfer and thermodynamics of the components for a complete charge and discharge cycle. The thesis presents a realistic behaviour that is close to the real operations of the plant. Argon is studied as a monoatomic gas with a high energy and power density that can be used as the working gas. The thesis is thus focused on the influencing mechanism of the parameters of the PTES system shown in Fig. 1.2, and on the optimization of the selected configuration. The procedure can be divided into seven different parts as summarized in Fig. 1.3:

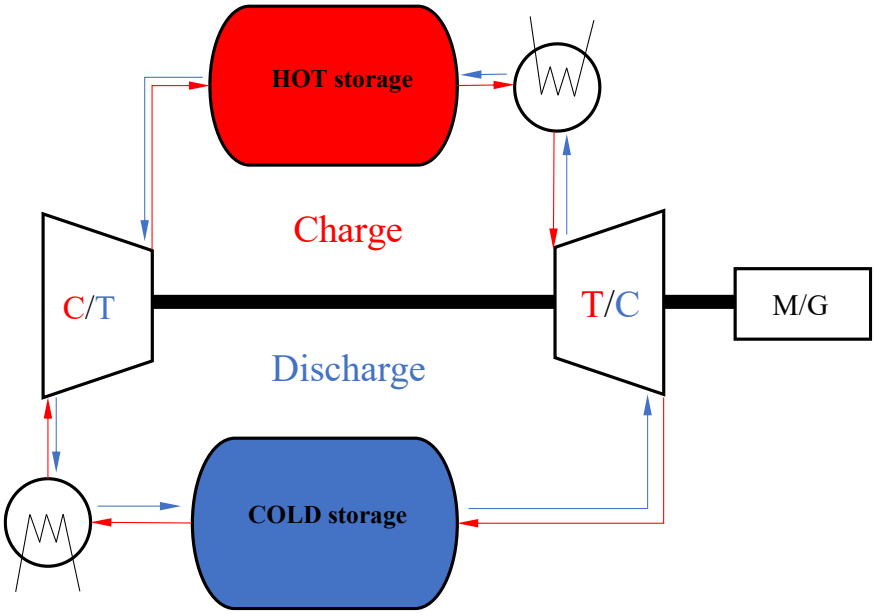

Fig. 1.1: Joule-Brayton based PTES

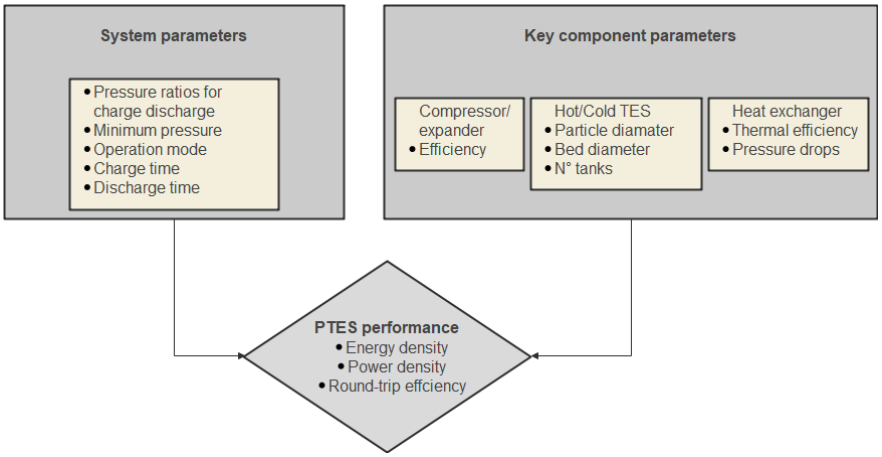

Fig. 1.2: Parameters influencing the PTES performance

Literature review:

First, a literature review is proposed to set a solid theoretical basis to sustain preliminary design choices and plant configuration such as machinery (volumetric or turbo), storage design, working fluid and expected rating parameters.

Basic steady-state analysis:

A preliminary and simplified analysis is performed to better understand the relationship and main trends between the system parameters and the performance of the plant. In this section, the plant is considered under the steady-state condition without accounting for mass variation inside the storage due to the progress of the thermal front. The heat transfer between the working gas and the solid media is considered ideal. The outcomes are the selection of working fluid, the compression ratio during the charge period, the storage tanks volumes, the void fraction and the particle diameter. These aforementioned factors are used in the subsequent sections as input data.

Plant equipment:

All components with their respective models are covered and discussed in this section. This modelling is more realistic and reliable compared to the simplified analysis. As far as turbomachines are concerned, the respective dimensionless operating curves are used to predict the behaviour in off-design conditions. Heat exchangers are treated as counter-current with the $\in$/NTU method, to provide the required parameters for accurate control of the gas outlet temperature. The heat transfer between solid and gas is again considered ideal but the shifting of the thermal front during the operation creates a dynamic regime, in which the mass inside the storages varies over time.

Dynamic analysis:

The operation of the system in dynamic regime will be analysed. The temperature profiles and the thermophysical properties of the gas in the CR and HR are changing during the storage process, thus resulting in a change in the pressure loss and overall in the mass contained inside the pores of the packed beds, influencing in this way the operating pint of the machines as well as the power level over time. The purpose of this analysis is to set the optimal compression ratio in the discharge phase which maximises the round-trip efficiency (RTE).

Packed bed heat transfer model:

A numerical model used to predict the real packed-bed storage performances is presented. First, the different models that can be adopted depending on the conditions and hypothesis selected are listed in a literature review. After that, the selected analytical and numerical methods are presented and described followed by some useful correlations, enabling quantifying the main physical phenomena involved in the packed bed. Then, a case validation of the selected method followed by a sensitivity analysis has been performed.

Plant simulation with convective heat transfer:

A comparison between the ideal and real operation of the plant is presented to underline the consequences of the real heat transfer phenomena, along with possible solutions to mitigate the problems encountered.

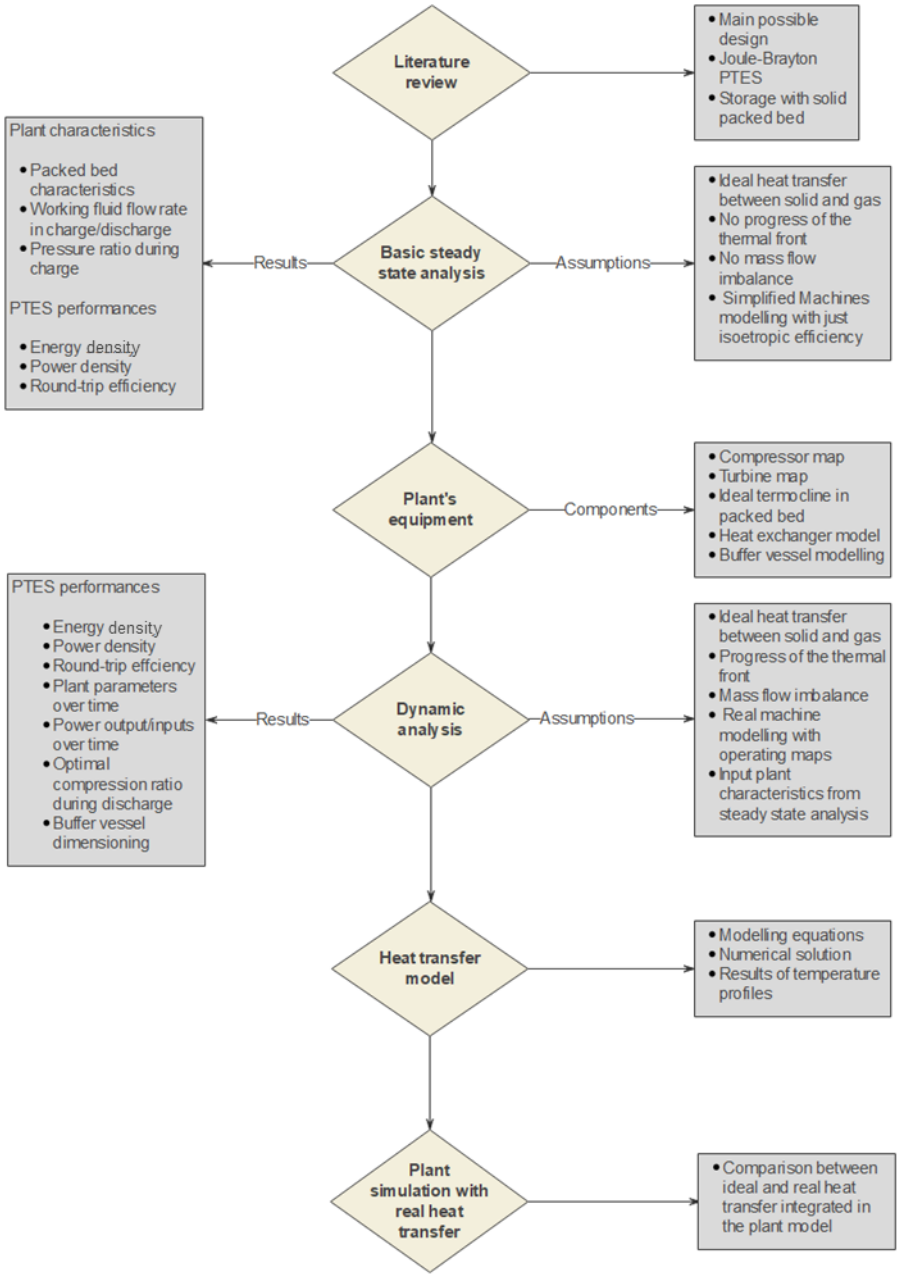

Fig. 1.3: Thesis scheme

2 Literature review of Pumped Thermal Electricity Storage

Energy storage

Before listing the main and most widely used energy storage technologies, it is necessary to better define the concept of energy storage. Three steps are involved in the process of storing energy: charging, storing and discharging [2]. There are many forms of energy, which can be grouped into two categories: primary and secondary [3]. Coal, natural gas, uranium, water, sun, wind, etc. are primary forms of energy, while electricity, heat, hydrogen, etc. are secondary forms of energy, which are products of conversion from primary energy sources. The technologies of interest for the present thesis will be those for storing secondary energy, i.e., electricity. When electricity is converted into another stable form, stocked and, after that, converted again in electricity, the storage is called “Electrical Energy Storage”; while, when the stocked energy is restored in the form of thermal energy (heat or cold), the storage process is called “Thermal Energy Storage”. Energy Storage is then sub-classified as follows: Mechanical ES, Chemical ES, Electrochemical ES and Superconducting Magnetic ES (SMES). Thermal Energy Storage can be sorted as: Sensible Heat Storage, Latent Heat Storage, and Thermochemical Heat Storage. In the present study, only the storage of electricity in the form of sensible heat is considered. In Mechanical Energy Storage (MES), electricity is converted into another easy storable form of energy employing mechanical systems while Chemical Energy Storage (CES) includes all the technologies which produce storable chemical compounds using electrical energy. MES units include Pumped Hydro Storage (PHS), Compressed Air Energy Storage (CAES), Gravity Energy Storage (GES), Liquid Piston Energy Storage (LPES), Liquid Air Energy Storage (LAES), Pumped Thermal Electricity Storage (PTES) and Flywheels Energy Storage (FES) while hydrogen, methane, hydrocarbons or biofuels like ethanol, methanol biodiesel, etc. are part of the category called Chemical Energy Storage. Supercapacitors and batteries constitute the technologies that compose the Electrochemical Energy Storage systems. Only a few of the above-mentioned technologies can store a quantity of energy higher than 100 MWh, such as PHS, CAES, Flow Batteries (FBs), GES, LAES, PTES, and Hydrogen. To date, Pumped Hydro Storage is the most mature and widely adopted technology while CAES and flow batteries are commercially

mature technologies but with a limited spread. On the contrary, GES, LAES, Hydrogen Storage, and PTES can be considered in developing for large-scale storage capacity [4]. New long-duration Energy Storage Technologies are required to support intermittent availability of the most used renewable energy resources; these systems need to be competitive and to overcome the issues related to the modern PHS, Li-batteries and CAES systems:

- Lower cost than pumped hydro or batteries
- Higher round-trip efficiency and fewer carbon emissions than gas-fired CAES
- Non-specific geology (mountains or salt caverns)
- High storage density

Carnot Batteries are an emerging technology for the inexpensive and site-independent storage of electric energy at medium to large scale. Also referred as "Pumped Thermal Electricity Storage" (PTES) or "Pumped Heat Energy Storage" (PHES). Reaching from medium to high capacities (up to 1000 MWh) as shown in Fig. 2.1, this technology has the potential to solve the global storage problem of renewable electricity in a more economic and environmentally friendly way than conventional batteries. Thermal storage materials are a plentiful, inexpensive and safe allowing high storage densities and low costs [5].

Table 2.1: Storage Technologies comparison [4], [6]–[8]

Technology	**Energy density [kWh/m^3]**	**Capital cost [€/kW]**	**Cost per unit of energy [€/kWh]**	**RTE [%]**	**Lifetime [y]**
PTES	46-100	454-965	20-80	50-70	25-30
PHS	0.5-1.5	600-2000	5-100	65-87	30-60
CAES	3-12	400-800	2-200	40-95	20-60
LAES	50	900-2000	260-530	40-85	20-40
Li BATTERIES	46-100	740-1130	1000-1500	95	20
FLOW BATTERIES	250-670	600-1500	120-1000	20-50	5-30

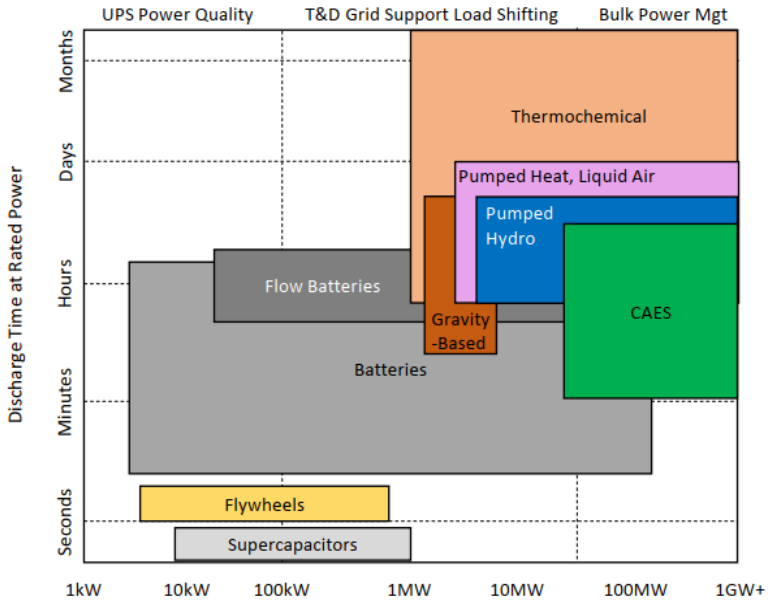

Fig. 2.1: Comparison among different storage technologies [9]

2.1 Pumped Thermal Electricity Storage: Basic concepts

The heat can be stored in the form of sensible or latent heat. In the first case, the thermal energy is stored in the change of the storage medium temperature, which is a consequence of the variation in the internal energy, while, in latent heat storage, the thermal energy is stored in the phase change energy. Sensible heat storage can either use solid or liquid as storage media. Exploiting solid media like concrete, rocks or sand is the most inexpensive, safe and easy way to store thermal energy. Despite the way of storing heat, the off-peak electricity is converted into heat using a high-temperature heat pump, storing the thermal energy in two tanks. This process is called the "storing phase". Then, the conversion of the stored heat into electricity is done through a heat engine. This phase is usually called "delivering" or "discharging" phase. Since 1979, several patents have been registered with different types of PTES configurations while only a reduced number of theoretical works have been published in the scientific literature. A PTES system can be categorised according to the combination of power-cycle, thermal storage units and working fluids. Closed Brayton cycle or reversible Brayton cycle is the first plant arrangement. It uses a single-phase gas like Air, Argon, Helium or Nitrogen and it is equipped with a low and high-pressure reservoir. To minimize the entropy generation in the heat transfer processes, sensible heat storage units are

preferred for this configuration [10]. Transcritical Organic Rankine cycle using CO_2 as working fluid and equipped with ice and pressurised water storages are the second type, while the third is the one based on traditional Rankine cycle. The basic thermodynamic scheme consists of three phases as shown in Fig. 2.2:

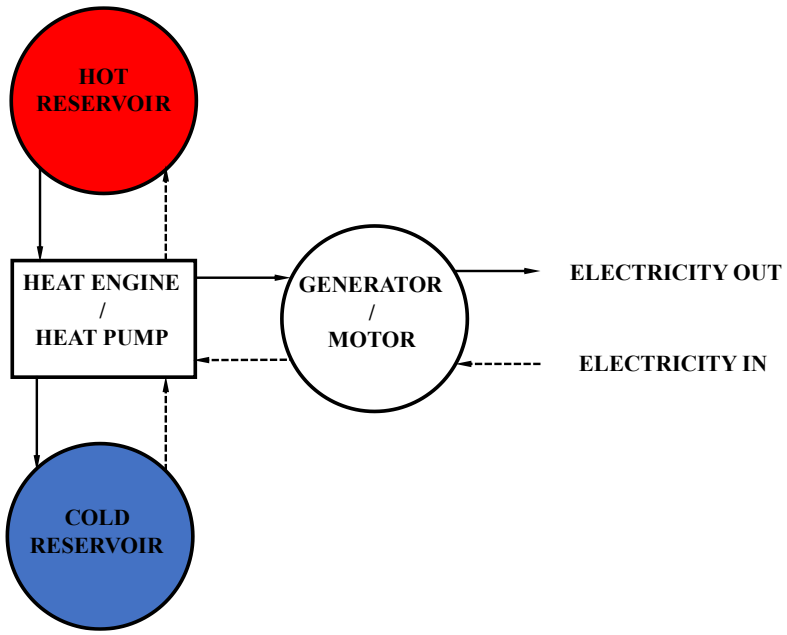

Fig. 2.2: Basic scheme of a PTES system

- CHARGE: an electrically driven heat pump is employed to transfer thermal energy from a cold reservoir to a hot reservoir.
- STORAGE: the thermal energy is stored until the delivery phase starts. Reservoirs are insulated to minimise losses during this period; losses are proportional to the surface, but energy content is proportional to the volume, so it's important to maximize the volume to area ratio of the storage.
- DISCHARGE: a heat engine is operated between the same reservoirs to recover the energy stored.

2.1.1 Rating Parameters

The following parameters are the most important and useful to assess the performance of an energy storage system.

Round-Trip Efficiency (RTE): defined as the ratio between the energy produced during discharge and the energy absorbed during charge. It is the most important performance index, and it represents the overall efficiency of the storage system. What may be counter-intuitive is that in the case of reversible transformations, the efficiency of the complete charge and discharge cycle is 100%. This happens because without considering the irreversibility of heat exchange and work exchange, whatever PTES system is considered, the energy absorbed is equal to the one generated. If a Joule Brayton cycle is considered for the heat engine and the heat pump, it is easy to see that the power absorbed/produced by the compressor and expander compensate each other in the charge and discharge phase, thus making the efficiency 100%. The round-trip-efficiency in the ideal reversible case can be written as the efficiency of the engine times the coefficient-of-performance (COP) of the heat pump:

$$\chi_{ideal} = RTE = COP \times \eta_{HE} = \left(\frac{T_{Hot}}{T_{Hot} - T_{Cold}}\right) \times \left(\frac{T_{Hot} - T_{Cold}}{T_{Hot}}\right) \qquad (2.1)$$

which are inversely proportional to each other in the ideal, reversible case [1]. To obtain the real value of RTE it will be necessary to consider the irreversibilities of the process that will reduce the ideal RTE, reaching values between 40-70% (PTES), depending on the efficiency of the single components and the type of engine/heat pump. The RTE is important also for the definition of the minimum cost of the electricity to be sold in the discharge phase defined as:

$$C_{el,disch} = \frac{C_{el,ch}}{\chi} \qquad (2.2)$$

Work Ratio (WR): defined as the ratio between expansion work and compression work, which can be computed for both charge and discharge periods. In most thermodynamic cycles used for storage, a compressor/pump and an expander are present simultaneously. Having high work ratios enables the installation of smaller machines and the achievement of a higher RTE for the same power requirement [5], [11].

$$WR = \frac{w_C}{w_E} \tag{2.3}$$

Energy and Power density (ρ_E, ρ_P): The maximization of such parameters decreases the specific cost per unit of energy stored and per unit of power capacity. Energy density is defined as the ratio between the maximum (nominal) electrical energy that can be delivered by the expander during discharge and the total volume of the storage system (kWh/m^3). The power density instead, is defined as the ratio between the maximum (nominal) power delivered by the system and the maximum volumetric flow rate of the working fluid, which is computed at the outlet of the turbine during discharge (kW/m^{3}s^{-1} or kJ/m^3).

$$\rho_E = \frac{E_{el,disch}}{V_{tot}} \ , \ \rho_P = \frac{\dot{W}_{max,disch}}{\dot{V}_{max,disch}} \tag{2.4}$$

2.1.2 Joule Brayton Battery: Characteristics and main proposed layout

In the following section, the design proposed by various authors will be analysed. In the Joule-Brayton implementations of PTES, the working fluid always remains in the gas phase. A compressor and an expander are used to drive a high temperature-ratio heat pump during charge, and a heat engine during discharge. The thermal energy is stored in the hot and cold stores with the sensible of the storage media, and two external heat exchangers (coolers) are used to reject heat, which is derived from irreversible processes during discharge, as shown in Fig. 2.3. The basic characteristics of the cycle remain the same in the different proposals, while design choices such as working fluid, storage material, maximum temperatures, number of heat exchangers and heaters/coolers characterise and differentiate the different layouts. Concrete proposals on a large-scale storage plant based on the Joule Brayton cycle are quite recent. In 2010, Desrues [12] was one of the first to propose a comprehensive theoretical study on a large-scale storage system. It consists of a high-pressure (HP) tank and a low-pressure tank (LP), four turbomachines (one compressor/turbine pair used during the loading period, and another pair for the delivery period), and two heat exchangers as shown in Fig. 2.3. The tanks are regenerators, made of refractory material which will alternatively store or deliver heat. The turbomachines allow the circulation of a gas (Argon) in the tanks, following a closed thermodynamic Brayton cycle [12].

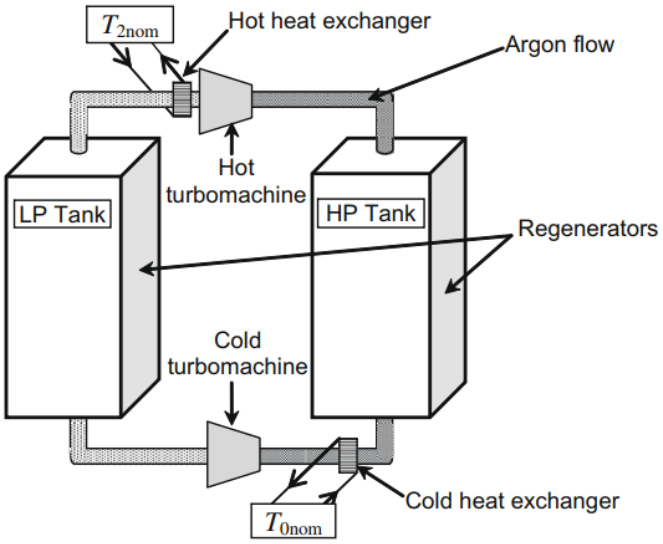

Fig. 2.3: PTES plant scheme proposed by Desrues [12]

The system examined by the author, as well as the others that will be illustrated, are the basis for an active and critical comparison of the results of this thesis. The author proposes a system with 602.6 MWh of nominal storage capacity. The complete charge and discharge duration are respectively 6h03min and 5h52min, employing a storage volume of about 21622 m^3. During the charge, Argon is compressed and reaches the temperature of 1000°C and the pressure of 4.6 bar. Then, the working fluid enters the hot tank and heats the refractory material from 25°C to 1000°C. At the same time, the temperature at the outlet of the turbine is around -70°C. During the discharge period, the turbine outlet temperature is 500°C, cooled down to -70°C in the cold storage, while, the outlet temperature of the compressor is 60°C. The two main heat exchangers are fundamental to control the inlet temperature to the storage volumes during discharge time. A significant 66,7% of RTE is obtained, considering a realistic polytropic efficiency for the turbomachines of 0.9 (both compressor and turbine) [12]. A complete model in terms of heat transfer is presented but the conclusions state that the model needs to be validated using a test rig with sufficiently large storage vessels; moreover, the author did not consider the unbalance in mass flow rate during the charging and discharging time, caused by the progression of heat front, which must be studied for the fluid-dynamic matching between turbine and compressor. McTigue et al. [6] proposed a study about a hypothetical 2 MW PTES system with 16 MWh of nominal capacity (Fig. 2.4). The main system components are two volumetric compression–expansion devices (CE and EC) and two thermal reservoirs (one hot, HR, and one cold, CR). Compression and expansion are achieved by

reciprocating devices since there is evidence that these are capable of higher polytropic efficiencies than turbomachinery. A second, crucial advantage of reciprocating devices is that, by adjusting valve timings, they can in principle be reversed such that compressors become expanders and vice versa. Using Argon as working fluid and setting a pressure ratio of 10:1, the nominal hot and cold storage temperatures (based on isentropic compression and expansion) are respectively 505°C and -150°C. In addition to the main components described above, the PTES system also requires heat exchangers and a buffer vessel. A buffer vessel is required because the total mass of gas within the two reservoirs changes during charge and discharge time, because of the the advancing of the heat front inside the tanks [6].

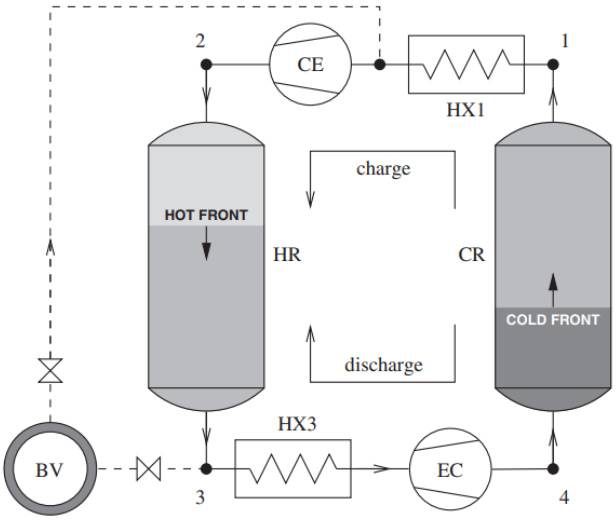

Fig. 2.4: McTigue plant layout [6]

The storage material is Fe_3O_4, which is a suitable storage material due to its high heat capacity per unit volume and its low fractional variation of heat capacity over the temperature ranges of interest. The reservoir volumes are calculated considering that the storage material is in the form of a packed bed of spherical pebbles with an average void fraction of 0.35. McTigue et al. [6] performed a multi-objective optimization to generate the trade-off surfaces known as Pareto's fronts. Predicted efficiencies and storage densities obviously depend on the different combinations of parameters obtained by the stochastic algorithm and on the assumed loss factors. With reasonable estimations for mechanical and electrical losses (0.04% and 2% respectively), this would give an overall round-trip efficiency of just under 70%. White et al. [11] proposed a complete study dived between various articles combining the thermodynamic cycle analysis with a real heat transfer model between storage material and working fluid, shown in Fig. 2.5.

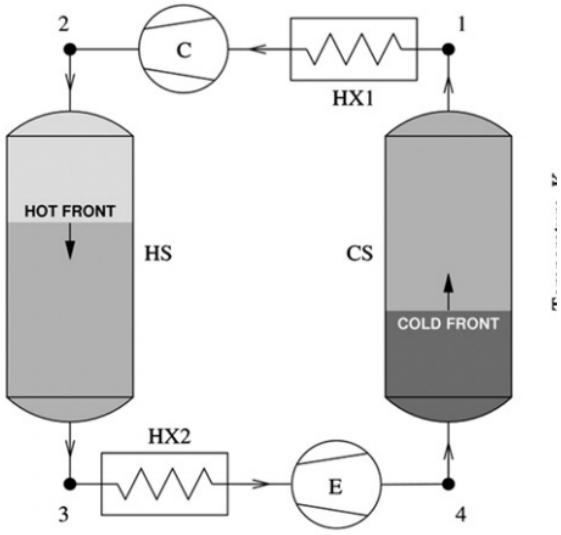

Fig. 2.5: White PTES plant layout [11]

The plant utilizes Argon as working fluid and gravels as storage material, with the following characteristics: $T_1 = T_3 = 300$ K, $p_1 = 1$ bar, $(T_2/T_1) = 2.58$, during charge. The investigations found that the energy density and power density are respectively 50 kWh/m^3 and 240 kJ/m^3. Round-trip efficiency and storage density increase with the compressor temperature ratio but adopting high-temperature ratios imply high-pressure ratios. Finally, White et al. [2] claimed that reducing the ratio between the hot and the cold temperatures during the discharge can mitigate the effects of the compression and the expansion irreversibility. In addition, this temperature ratio reduction implies an increment of the power and energy density. In 2012, Howes [13] firstly investigated the thermodynamic aspects of the idealized heat pump; a prototype has been designed and built to investigate the pressure losses and the heat transfer process during the compression and the expansion phase. A peculiarity of the prototype is the integration of the heat exchangers into the reciprocating machine (Fig. 2.6).

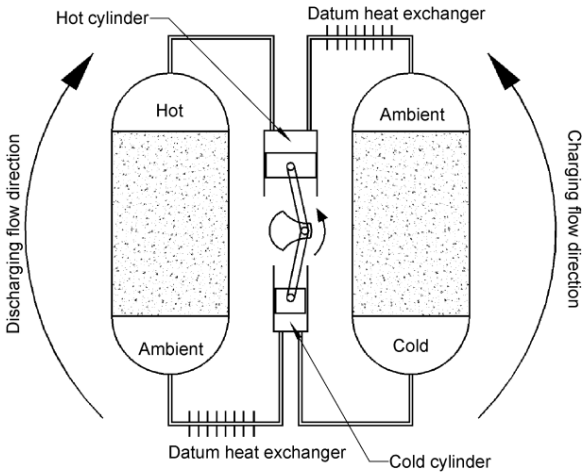

Fig. 2.6: Howes PTES layout [13]

This device consists of a single double-acting cylinder with valves at both ends of the cylinder and a piston for a uniflow configuration. The cold cylinder is smaller than the hot one for equal mass flow. Based on the experimental investigations performed on these prototypes, Howes [13] developed a hypothetical 2-MW (absorbed power during charge) storage machine that may be defined with the following characteristics:

Working fluid	Argon	-
Mass processed per cycle	638	kg/s
Hot store pressure	12,13	bar
Cold store pressure:	1,013	bar
Hot store temperature:	500	°C
Cold store temperature:	-166	°C
Design running speed	1200	rpm
mass flow rate	12,56	kg/s
heat per cycle of hot store	159412	J
heat per cycle of cold store	59412	J
nominal work per cycle	100000	J

Obtaining a final RTE=72%, close to a pumped hydro RTE=74%. In 2007, he sold his stake in AeroDAC to concentrate on the development of the energy storage concepts within Isentropic Ltd, which recently patented a prototype of 150 kWe using reciprocating devices. In recent studies (2017), Benato [14] presented a PTES configuration in which an electric heater is used to convert

off-peak electricity into thermal energy (Fig. 2.7). Air is used as the working fluid and just one heat exchanger is adopted to maintain the expander inlet temperature at its design value. During the delivery phase, no heat exchangers are used.

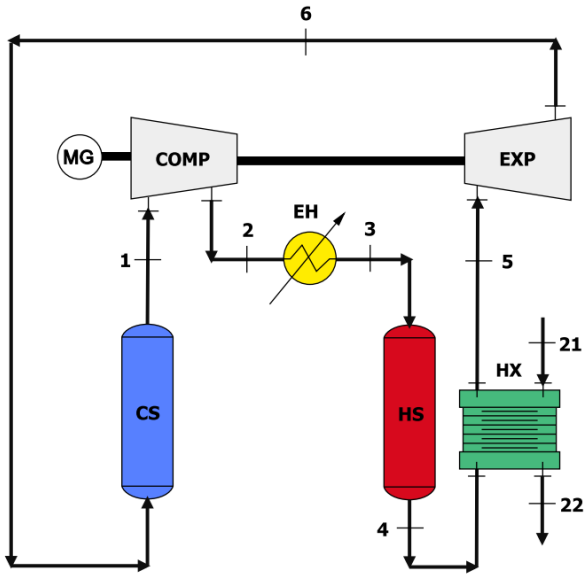

Fig. 2.7: Benato PTES layout during charge [14]

Five types of storage material, two bed material shapes and different maximum plant temperatures have been tested to evaluate their influence on the plant performance and costs. Despite the low round-trip efficiency of 8.5%, related to the high losses in the HX during the charging phase, the low maximum cycle temperature, and the implemented control strategy, the proposed plant arrangement is characterised by an energy density in the range of 70–430 kWh/m^3 and a specific cost in the range 50–180 €/kWh. In 2019, Davenne et al. [15] considered the feasibility of a large-scale storage system (1 GWh nominal storage capacity), with maximum power absorption in charge mode 165 MWe and total a storage volume of 9000 m^3 (2/3 for the cold vessel and 1/3 for the hot vessel), using a PTES system with de-coupled thermal stores, as shown in Fig. 2.8;

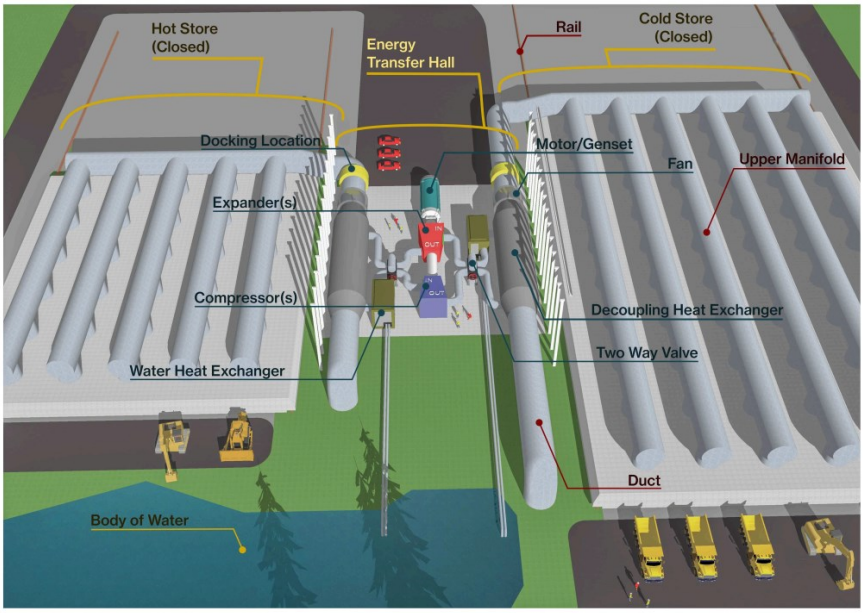

Fig. 2.8: De-coupled PTES system 3D layout [3]

providing a comparison with the more investigated coupled system. Based on ambitious but still realistic component performances, an energy storage round trip efficiency of 65.3 and 59.5% is obtained for the coupled and de-coupled systems, respectively. Even with dwell times in the charged state of 5 days, a round trip efficiency of over 50% is still predicted in both systems, suggesting that PTES could offer a viable large-scale, long-duration energy storage. A de-coupled system is one where the thermal stores have a dedicated heat transfer fluid circulating within them, which does not pass through the compression /expansion working circuit as shown in Fig. 2.9. The separate working circuit transfers heat to the thermal store circuits via de-coupling heat exchangers. The potential advantage of this is that the thermal reservoirs, in particular the hot one, do not have to stay at the same high pressure of the working circuit, and can operate at near atmospheric pressure. This opens the door to the design of large thermal stores without the constraints and size limits of high pressure, heavy-walled, cylindrical vessels which are recognized as the most efficient geometry for a pressure vessel. The de-coupled system does require two fans to circulate heat transfer fluid through the thermal stores and the de-coupling heat exchangers. These bring an additional loss, but the pressure drop through the thermal store and de-coupling heat exchanger can be made low to minimize this additonal cost [15].

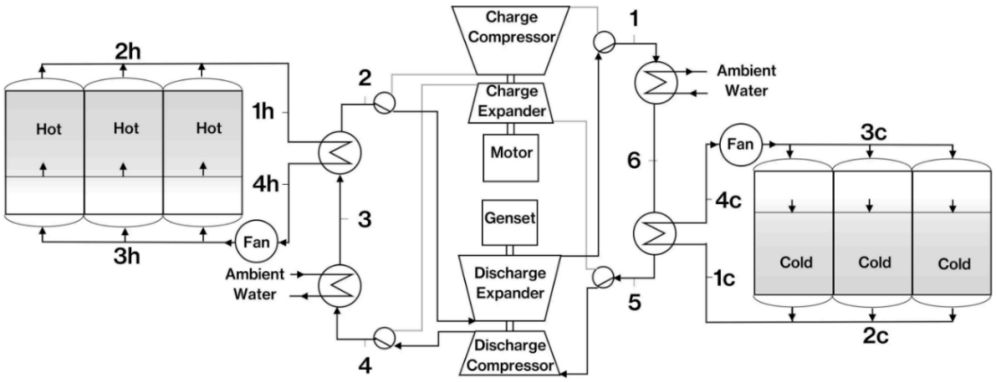

Fig. 2.9: De-coupled PTES layout [3]

2.2 Thermal storage: Solid media

In the case of solids, the material is invariably in porous form and heat is stored or extracted by the flow of a gas or a liquid through the pores or voids. The operating temperature range of TES is limited by the thermal stability of filler material. Earth materials like rocks, gravels, sand are the most used, and such systems operate in the medium temperature range between 50°C- 300°C [16]. Energy can be stored up to 850°C in specific sands, cast Iron, Steel, Aluminium oxide, Magnesium oxide, Quartz, Basalt and Granite. This range can be increased up to 1000°C, selecting solid materials like refractory bricks. Metals have good conductive characteristics and do not require a large heat transfer area. Sand, on the other hand, needs a large heat transfer area because of its insulative property. The basic equation for sensible heat storage is:

$$Q = \int_{T_1}^{T_2} M\, c\, dT \qquad (2.5)$$

where T_1 and T_2 are the initial and final temperature of the storage material, M is the material total mass, and c is the specific heat capacity of the material. The high specific heat capacity can have a direct impact on the amount of stored thermal energy. The long-term stability assures the low degradation of the heat storage material after thousands of thermal cycling. From the foregoing definition, desirable sensible heat storage requires the energy storage material to have four characteristics [17] :

- High specific heat capacity
- Long term stability under the thermal cycling

- Good compatibility with its containment
- Low cost

Solid storage media are considered mainly for economic reasons. Compared to today's molten salts, the costs of the equivalent mass of solid materials might be one order of magnitude lower, and some materials like natural stones might be even two orders of magnitude cheaper. The savings from using a cheaper storage material are often reduced by the more complex heat transfer concept.

2.2.1 Main solid bed design

The proposed layout for solid thermal storage are the following [18]:

- Regenerator design: the thermal storage material contained in the vessel is heated/cooled by the HTF
- Active design: the thermal storage material contained in the vessel is heated/actively cooled by the HTF, thus transporting it in a heat transfer zone

The Regenerator thermal storage design can be divided into three categories (as shown in Fig. 2.10):

- Packed bed system: a fixed bed of filler material that acts as the primary heat storage, which is put in direct contact with the HTF, that moves through the voids inside the filling
- CellFlux: The CellFlux concept has been developed to allow the application of packed bed storage volumes also for liquids and pressurized gases like synthetic heat transfer fluids or molten salts
- Embedded heat exchanger: can be used when direct contact between HTF and solid media is not feasible. Castable materials like concrete or ceramics allow the integration of a parallel tube heat exchanger into the storage volume, which simplifies the heat transfer model and allows a unique block of material to be used for storage

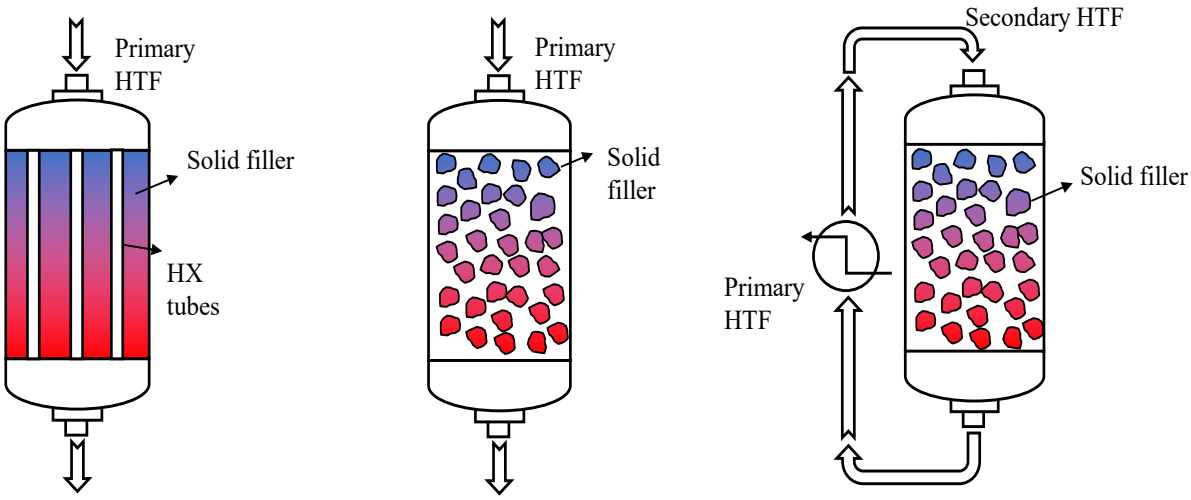

Fig. 2.10: Solid media storage layout from left to right respectively Embedded heat Exchanger; Packed bed; CellFlux

Different bed designs can be used for different solid storage layouts:

- Packed beds are very versatile and can be used also in the CellFlux concept
- Fluidized beds can be used when direct contact is not feasible or to improve the heat transfer coefficient between solid and gas, especially when a bubbling fluidization regime is present. Solid particles are suspended in a flowing fluid making the transport of particles through the bed possible. This design can be applied in the Embedded Heat exchanger concept or in the Active design
- Moving bed systems are like the fluidized bed in concept, except that the particles slowly move downwards with the aid of gravitational force in slanted ducts rather than through a high-speed fluid flow; the advantage is that no-direct heat exchange is possible through a heat transfer zone. They are characterised by a low parasitic consumption compared to fluidized beds which require pumping of fluid.

Most of the concepts use a fixed storage volume [11], [14], [15], [19] as in the 150 kWe/4h PTES pilot-scale plant made by the new National Facility for Pumped Heat Energy Storage together the former Isentropic facility and Newcastle University's Sir Joseph Swan Centre for Energy Research(Fig. 2.11).

Fig. 2.11: Small scale pilot plant made by the new National Facility for Pumped Heat Energy Storage

Some innovative studies refer to the de-coupled system [15] to overcome the tank-pressurization, fluidized bed as patented by SandTes [20] and some prototypes for moving bed studied and proposed by Solex [21].

2.2.2 Packed bed

Packed or fixed beds are defined as beds in which the solid particles are completely stationary. These beds are characterised by low gas velocities, less than 1 m/s, with high particle diameter, between 1 and 20 mm to avoid bed drag and packing caused by the presence of fine particles. The fine parts clog the spaces between the larger ones, preventing the gas from passing through, increasing pressure drop and preventing extended contact. Due to the limited velocities and plug-flow movement, heat transfer is limited. The minimum void fraction (ε) achievable with an ordered 3D arrangement of spheres of equal size is 0.260, i.e., the volume occupied by the interstices between one particle and another divided by the total volume of the bed. This parameter can even vary for particles of equal size; typical values for large fixed beds are between 0.36 and 0.41. A packed bed for thermal energy storage systems has an insulated container holding the filler material. The HTF is used to charge and discharge a packed bed by heat transfer through direct surface contact without the need for a heat exchanger. This system has the characteristic of a temperature stratification effect along the bed. Typical working fluids are Air, Water, Thermal oils and gases like supercritical CO_2, Argon or Helium, while typical bed filler materials are rocks, pebbles, gravel, sand, gypsum, soil, microencapsulated PCM containers, metal blocks, small

concrete cubes, small concrete spheres, masonry brick, porcelain balls, zirconium oxide pellets, irregular solids particles of iron ore, coke, limestone, coal, blast furnace charge, copper slag, iron slag, aluminium slag etc.. [16]. Packed beds and moving beds are potentially more compact and cost-effective than conventional storage systems, such as two-tank liquid stores, and have low parasitic consumption compared to fluidized beds, despite the lower heat transfer coefficient. Particularly packed beds are more flexible since they do not need a specific heat transfer zone or a high-speed fluid, and they are well-studied in terms of heat transfer modelling. This bed layout is chosen.

2.2.3 Prototypes and industrial-scale PTES systems nowadays

Nowadays, PTES systems are just prototypes or pilot-scale projects. It is worth mentioning for the specific subject treated in this thesis, as a novel technology, the GridScale storage system [22]. Commercialized by Stiesdal in 2019 is an industrialized and scalable technology for cost-effective thermal storage of electric energy. GridScale uses a crushed rock as a low-cost storage medium as shown in Fig. 2.12 offers high round-trip efficiency with no geological or topological constraints. The GridScale system's charging and discharging cycles are implemented as a heat pump, and two separate reservoirs store heat and cold, respectively. Since the maximum temperatures of the cold storage reservoir are much lower than in the hot storage reservoir, the cold reservoir can use any type of crushed rock. There is no degradation of the crushed rock storage materials, and the GridScale nameplate storage capacity is available for the full lifetime of the system.

Fig. 2.12: Full-scale reservoir installed at Company HQ, shown during stone-filling experiments (2020)

The charge-discharge system comprises one compressor-turbine system for charging and another similar but differently dimensioned system for discharging (Fig. 2.13). The charging system is operated in a heat pump cycle. The COP (Coefficient of Performance) is on the order of 250%, depending on the temperature ranges. The discharging system is operated in a so-called Brayton

cycle, as the cycle of a gas turbine. The efficiency is on the order of 20-25%, again depending on the temperature ranges. The total round-trip efficiency is the product of the charging COP and the discharging efficiency. For serial production systems, the round-trip efficiency is expected to be 55-60%. Since 2019, the GridScale concept and technology has been validated through a wide range of tests using a combination of standard industrialized components and proprietary technology. In 2022, the first full-scale demonstration project will be installed in Rødby on the Danish island of Lolland. It comprises a 4 MW/2 MW charge/discharge unit with a 10 MWh capacity to be installed next to Rødby's district heat and power plant. The total specific cost of the thermal storage materials, including storage tanks, insulation, etc. is expected to be less than 10 €/kWh electric discharge capacity for serial production systems. In comparison, conventional battery storage systems typically have storage capacity costs in the range of 200 €/kWh.

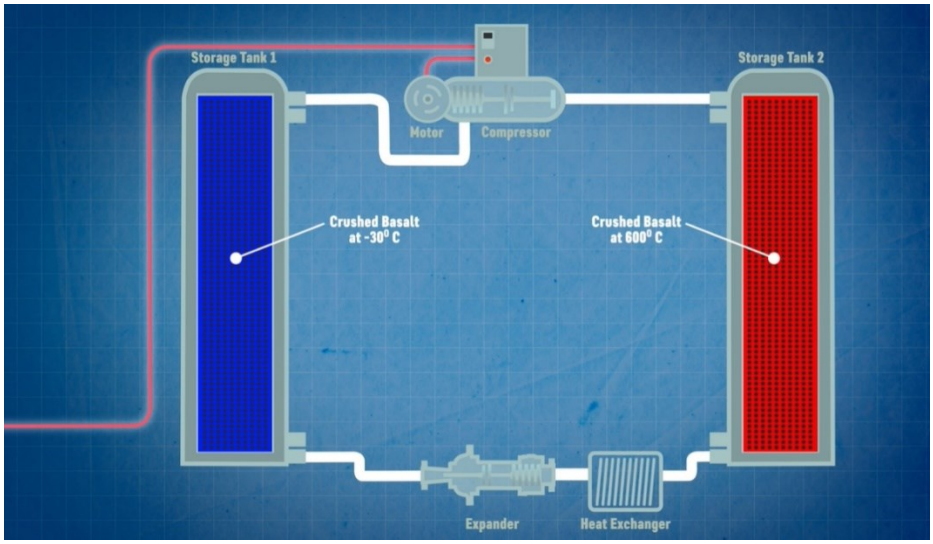

Fig. 2.13: GridScale heat pump cycle with Air

3 Plant design and methodology

Based on the PTES layout proposed in the previous chapter, the Joule–Brayton PTES discussed in this thesis mainly consists of a cold (low–pressure) TES packed bed reservoir, an hot (high–pressure) TES reservoir, two compressor–turbine–pairs, one for charging and the other for discharging, to maximise isentropic efficiency in the two different phases. Both packed beds will be filled, in this design, with spheres made of Basalt, as it has a good heat capacity and thermal stability within the temperature range of -171\830°C. Other materials can be used to fill the two tanks, depending on site availability. Single reversible turbomachines are not physically possible due to the different thermo-fluid-dynamic designs for compressor and turbine and different thermodynamic properties of the gas at the inlet of the machines during the two phases. Two heat exchangers are required to remove surplus heat from the system and stabilize the temperature variation in the reservoirs during the discharging process. A buffer vessel is also required to store/release gas, stabilizing the system pressure during charging/discharging, balancing the mass changes in the two reservoirs. In a fixed volume system, an average temperature increase will lead to an increase of pressure, leading to undesired pressurization, as treated also by Liang et al. [23]. A different pressure ratio between charge and discharge can be obtained by adjusting the buffer vessel, valves and pressure in the HR using the compressor co-ordinately during the idle period. The working principle plant is that during the charging process, the gas is driven by the compressor and goes first through the HR, then expands in the turbine (for charging) and finally absorbs heat from the CR. During the charging process, the heat is extracted from the CR to the HR while consuming electricity, with hot and cold thermal energy respectively stored in the HR and CR. During discharging, the working gas is cooled down by the CR, compressed by the compressor (for discharging), cooled down by the HX1, heated up in the HR, expanded in the turbine (for discharging) from high temperature and pressure, cooled down through HX2 and CR, as illustrated in Fig. 3.1 and Fig. 3.2.

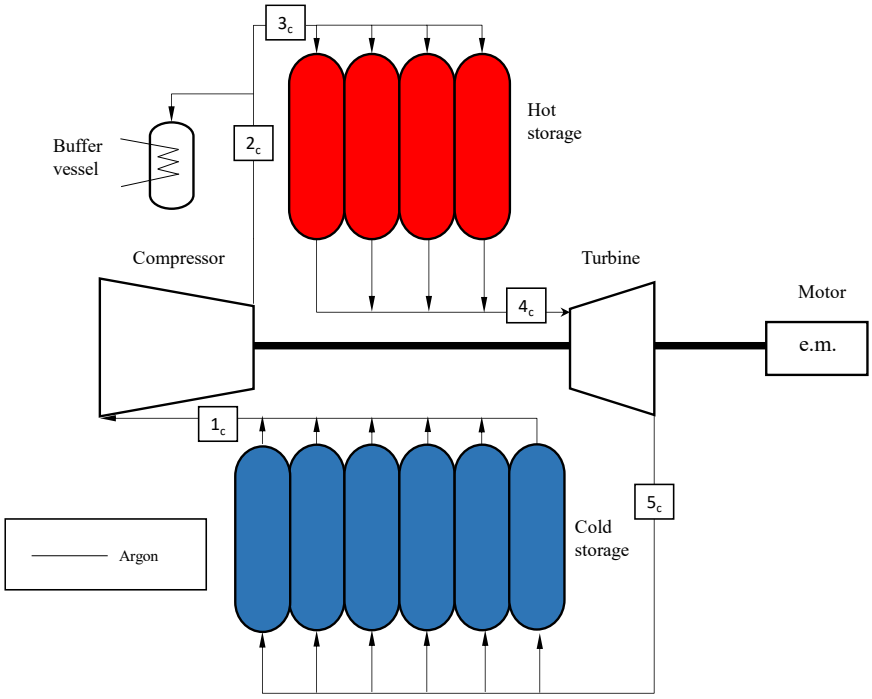

Fig. 3.1: Plant layout during charge, subscript 'C'

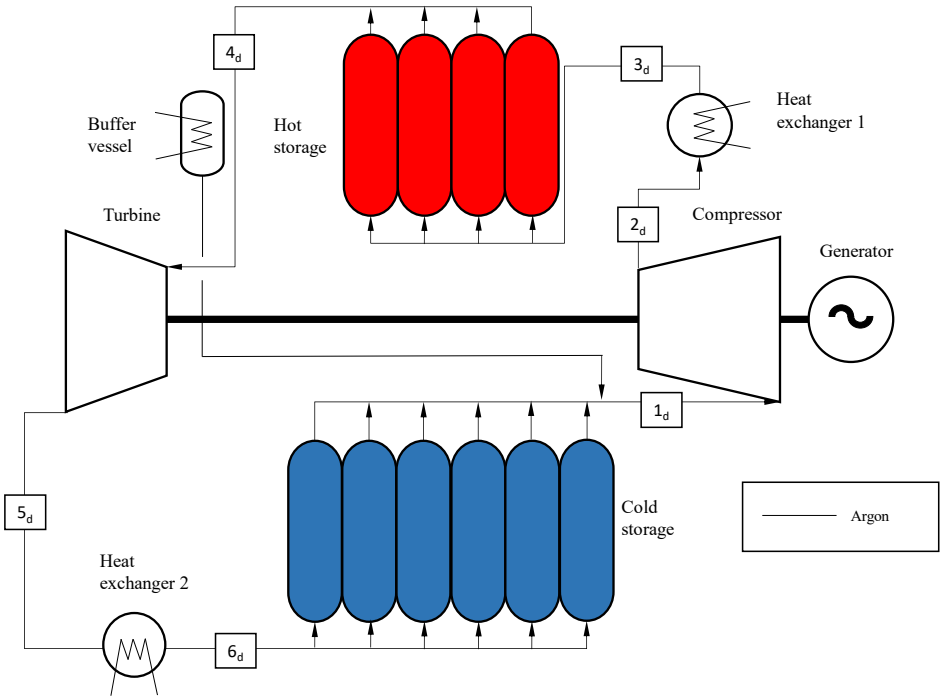

Fig. 3.2: Plant layout during discharge, subscript 'D'

The main advantages of such a PTES system are that it can be scaled up to very high-power output and stored energy thanks to the large solid storage volumes and the use of turbomachines, with a cost per unit of stored energy comparable to PHS systems, reduced investment costs and fair RTE. Table 3.1 summarizes the starting target design data.

Table 3.1: Design input data

Power absorption during charge	10-20	MW
Nominal charge time	5	h
Nominal discharge time	2	h
Type of machines	Turbomachines	
Thermal storage	Solid Packed bed	

Concerning the new energy storage systems, it is better to slowly charge the system when energy is available, and fast discharge when is needed. The massive penetration of photovoltaic (PV) causes a duck curve problem (Fig. 3.3.). In the duck curve, the difference of load demands at peak and off-peak is enormous, which causes thermal generators to not operate optimally and a higher risk of overgeneration and network instability during the day (typically from 6 a.m. to 9 p.m.). PTES can be then used as a load demand balancer. PTES will store electricity when the system has a surplus due to PV penetration during the day and will inject power into the system at night (typically from 9 p.m. to 12 p.m.).

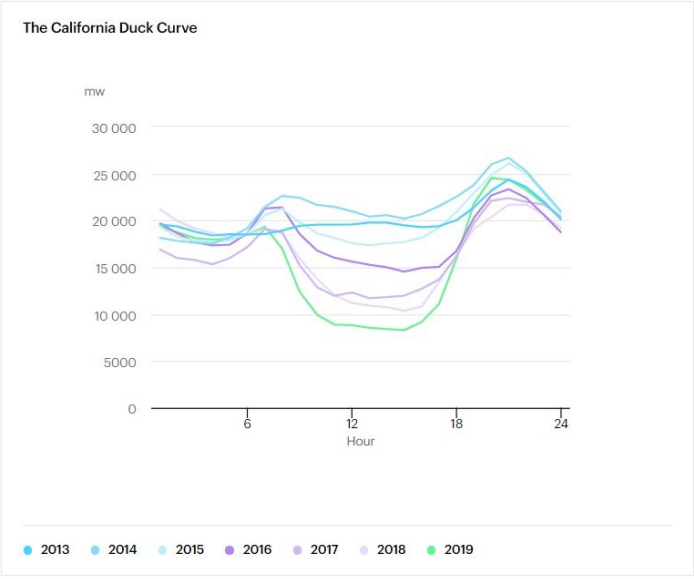

Fig. 3.3: The California duck curve [24]*, y-axis represents the difference between the required load and the PV capacity*

3.1 Preliminary design choices and sizing

The performance of PTES plants is strongly dependent on the preliminary design choices: turbomachines or volumetric machines, the position of the auxiliary exchanger to dissipate irreversibility, storage materials, number of vessels and their arrangement etc. Energy storage round-trip efficiency largely depends on the isentropic efficiencies of the compression and expansion equipment, the thermal effectiveness of the thermal stores, the presence of circuit pressure drops, heat leaks to and from the system and electrical machine efficiencies. Concerning the next two sections, the plant will be simplified with the following hypothesis:

- Steady-state operation, which implies no mass imbalance in the bed (treated in sub-section 3.2.3)
- Compression and expansion represented with real adiabatic transformation, neglecting the real performances maps (for simplicity represented with the same machine in Fig. 3.4)
- Constant gas temperature at the outlet of HXs
- Ideal heat transfer between solid and working gas, hence $h \rightarrow \infty$

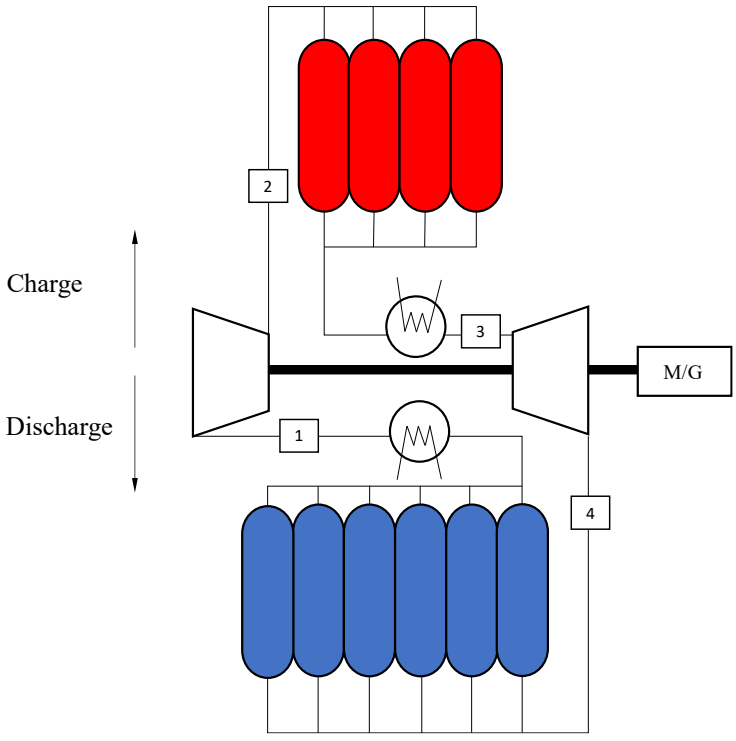

Fig. 3.4: Layout of a PTES system with turbomachines and packed beds: stationary framework

3.1.1 Basic thermodynamic analysis: Compression and expansion

As shown in the work of White [11], and as pointed out also by Farrés [5], during the preliminary design choices and sizing, it is important to underline and consider the approximate susceptibility to design parameters. Given the data in Table 3.1 and considering plant layout in Fig. 3.4, energy density, power density and round-trip efficiency can be written, for an ideal PTES system as follows. Defining ρ_E as the average energy stored in the reservoirs per unit volume of storage medium, and ρ_P as the power output per unit volumetric flow rate of the working fluid, considering λ as the isentropic temperature ratio of the compressor as T_2/T_1 and θ as hot and cold reservoir temperature ratio when discharged T_3/T_1, the straightforward analysis gives:

$$\rho_E = \frac{1}{2}\rho_S c_s\{(T_2 - T_3) + (T_1 - T_4)\} = \frac{1}{2}\rho_S c_s T_1(\lambda - 1)\left(1 - \frac{\theta}{\lambda}\right) \quad (3.1)$$

$$\rho_p = \rho_{g,1} c_{pg}\{(T_2 - T_1) - (T_3 - T_4)\} = (\tau - 1)\left(1 - \frac{\theta}{\lambda}\right) \times \frac{\gamma p_1}{\gamma - 1} \quad (3.2)$$

The following outcomes may be deduced from these expressions:

- Both the energy and power density are monotonically increasing functions of the temperature ratio λ, which depends on the pressure ratio and the isentropic index (γ) of the gas
- For a given pressure ratio (or λ), energy density and power density are both increased by reducing T_3 or increasing T_1. This is also shown by the dashed line in the T-s diagram, which encloses a larger area (Fig. 3.5)

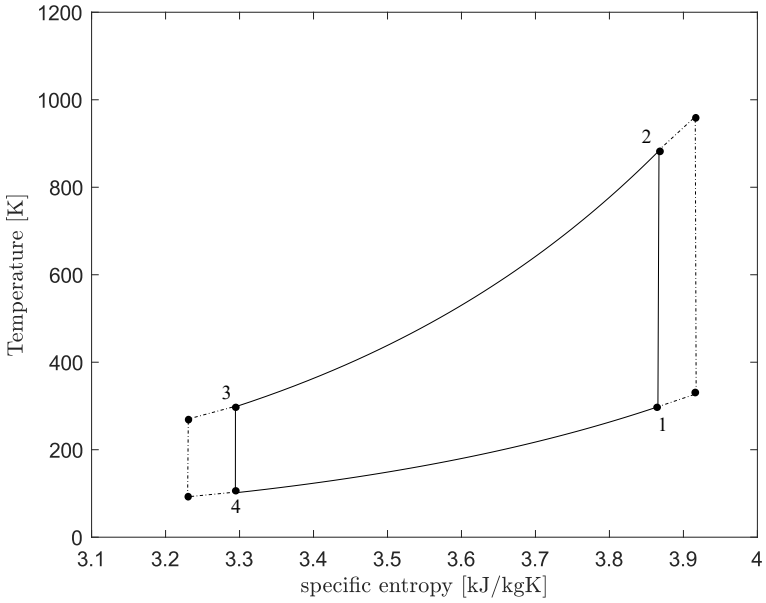

Fig. 3.5: T-s diagram for ideal PTES system (fluid: Argon; β=15, T_1=T_3=25°C)

Considering a real system by introducing the realistic thermodynamic efficiency of the machines, an upper limit of the round-trip efficiency can be obtained by assuming that there are no storage losses (i.e., the tanks are perfectly insulated, with no pressure losses) and that all the thermal energy stored during charge can be depleted during discharge (converting part of it into useful work, and rejecting another part to the environment). Irreversibilities tend to reduce expansion work outputs and increase compressor work inputs during both charge and discharge. An approximate estimation of how operating conditions influence the round-trip efficiency for the real (irreversible) system can thus be obtained by scaling compression work by $1/\eta_{is}$ and expansion work by η_{is}, where η_{is} may be interpreted here as an average isentropic efficiency. The round-trip efficiency, considering the same pressure ratio for charge and discharge as shown in Fig. 3.6 is then given by:

$$\chi = \frac{\eta_{is}(T_2 - T_1) - \frac{(T_3 - T_4)}{\eta_{is}}}{\frac{(T_2 - T_1)}{\eta_{is}} - \eta_{is}(T_3 - T_4)} = \frac{WR\,{\eta_{is}}^2 - 1}{WR - {\eta_{is}}^2} \qquad (3.3)$$

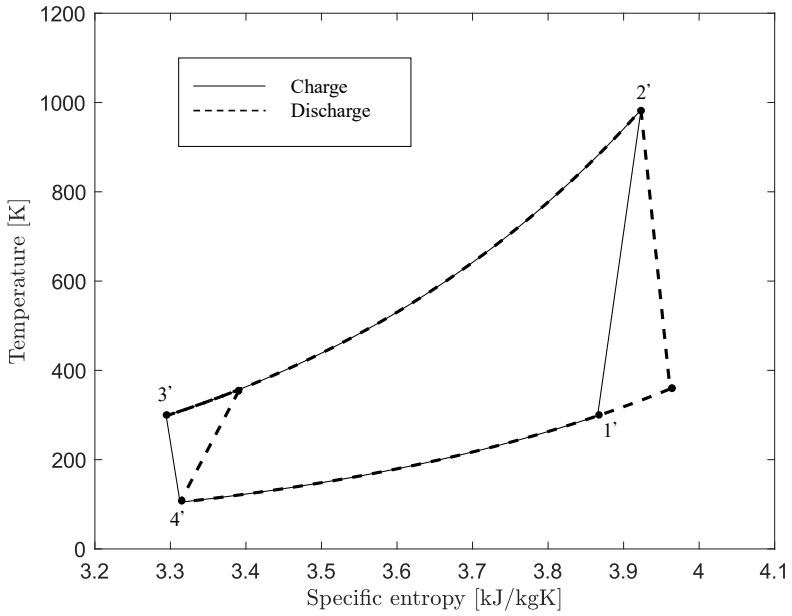

Fig. 3.6: T-s diagram for PTES system with ideal heat transfer and real compression and expansio processes (fluid: Argon; β=20, $\eta_{is,c}$=0.89, $\eta_{is,t}$=0.93)

where WR= T_1/T_4 =T_2/T_3= λ/θ = $W_{C,ch}$/ $W_{E,ch}$= $W_{E,disch}$/ $W_{C,disch}$ and T_1/T_4 represents the temperatures for the reversible cycle rather than the real one. For a given value of isentropic efficiency, the round-trip efficiency is a continuously increasing function of the ratio WR. From this basic equation can be observed that: RTE_{max} =η_{is}^2 if WR $\rightarrow \infty$ therefore if η_{is} = 0.9 the maximum reachable RTE is 0.81. The WR may be increased by raising the pressure ratio, decreasing the hot reservoir discharged temperature, T_3, or increasing the cold reservoir discharged temperature, T_1, all of which are consistent with improving the energy and power densities. High-pressure ratios, however, lead to high storage costs since HS needs to be pressurised. It is for this reason that a monoatomic gas like Argon is proposed as the working fluid rather than Air since the same value of λ can be achieved at a lower pressure ratio due to Argon's higher isentropic index. Given that higher efficiency is reached at higher T_2 (outlet compressor temperature during charge), this implies higher compression ratio and, simultaneously, lower temperature at the discharge of the turbine (same minimum pressure, same expansion efficiency but higher inlet pressure), typically lower than 0°C. The use of Air as working fluid would lead to icing if dehydration is not present, thus increasing the cost of the plant.

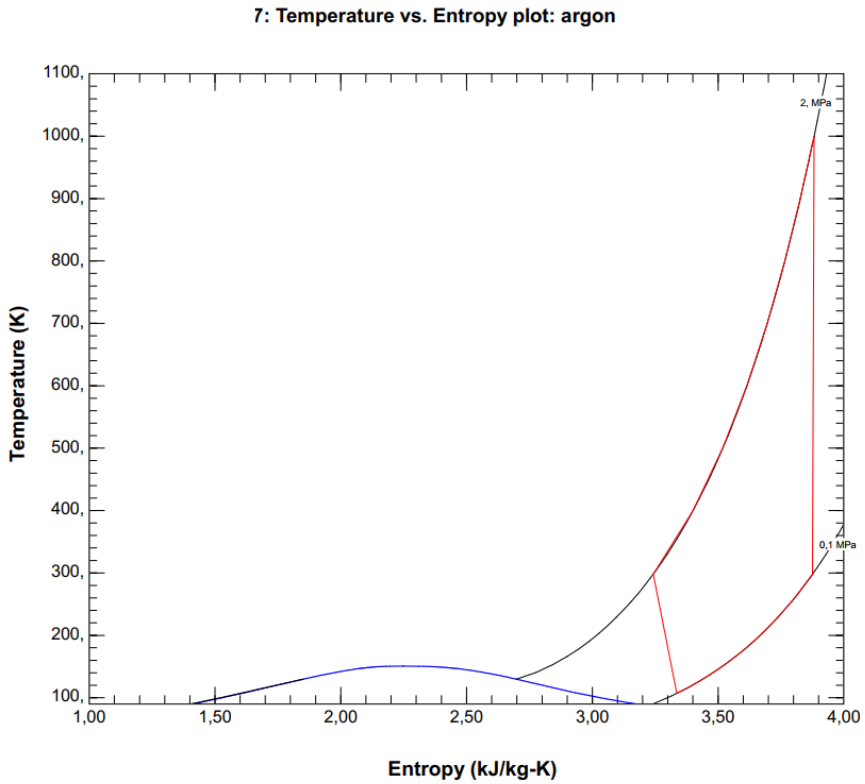

Fig. 3.7: Hypothetical cycle for PTES with Argon as working fluid; max. T=1000K, max. P=2 MPa, min T=107 K, min. P=0.1 Mpa

Considering for example typical values for temperatures and pressures of a Brayton power cycle for PTES as shown in Fig. 3.7, the gas can be treated as ideal also at very low temperature, since the compressibility factor (Z) range between 1.0046 and 0.9813 respectively for thermodynamic points: (T=727°C; P=20 bar), and (T=-173°C; P=1 bar).

3.1.2 Basic Steady-state analysis

In this sub-section a more comprehensive analysis, even if still simplified, is performed to provide the baseline design parameters used in the subsequent sections such as: compression ratio during charge, mass flow rate of working fluid, net power, stored energy etc., starting from the input data in Table 2.1 and referring again to the plant layout shown in Fig. 3.4. The numerical routines and the codes developed in this work are made with MatlabR2020a®, while the thermophysical and thermodynamic properties of the working fluid that cannot be computed with the ideal gas law (viscosity, thermal conductivity etc.), are computed using Refprop®, called during the numerical routines by an implemented auxiliary function.

Table 3.2: Assumptions scheme for steady-state analysis

Assumptions
Steady-state operation, which implies no mass imbalance in the bed and no buffer vessel
Compression and expansion represented with real adiabatic transformation, neglecting the real performances maps
The outlet temperature of working gas at the outlet of HX constant
Ideal heat transfer between solid and working gas
Pressure losses accounted for HX and TES

Concerning the properties of the solid, only the specific heat capacity is found to depend heavily on temperature. Only for this section, an average value between the maximum and minimum temperature in each of the storage tanks (cold and hot) is considered, respectively 950 /550 J/kgK for the HR and CR, as shown in Table 3.3. Assumptions for the numerical modelling are summarized in Table 3.2. The numerical routine is iterative since the pressure losses within the tanks are dependent on the thermophysical properties of the gas, which are in turn related to the pressure and temperature level, which are influenced by the same pressure drops. The iterative scheme is shown in Fig. 3.8 and . 3.9. Table 3.3 describes the input data, which are arbitrary choices and can differ from the ones selected. The non-fixed variable will be the subject of the following sensitivity analysis.

Table 3.3: Input data for the iterative procedure (Steady-state framework)

INPUT DATA		
Ambient condition		
$T_{amb}=T_{in,bed}$	25	°C
P_{amb}	1.01	bar
Packed bed		
Filler	Basalt	
ρ_s	3011	kg/m^3
c_s	950 (HR)/550(CR)	J/kgK
d_p	Variable: 3÷10	mm
D	4	m
N° vessels (cold/hot)	6/4	-
ψ[1]	1	
ε	Variable: 0.3÷0.5	-
Compressor and turbine		
$\eta_{is,c}$	Variable: 0.6÷0.95	-
$\eta_{is,t}$	Variable: 0.6÷0.94	-
$\eta_{mecc,c,t}$	0.996	-
$\eta_{el,gen}$	0.987	-
Compressor inlet Pressure	1.05	bar
Fluid		
Working fluid	Argon	
Mass flow rate	50	kg/s
Properties	Refprop®	
Heat exchangers		
$\Delta P\%$	2	%
$T_{out,\ gas}$	25	°C
Cooling medium	Water	-
Plant operation		
Nominal charge time	5	h
Nominal discharge time	2	h

[1] Sphericity of the filler

INPUT DATA

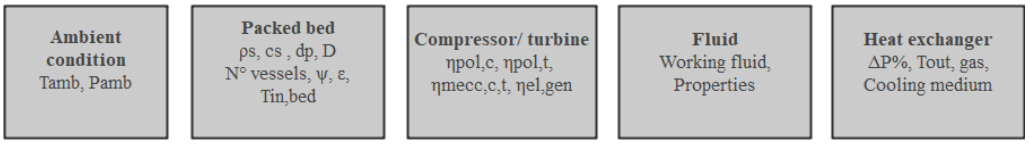

CHARGE

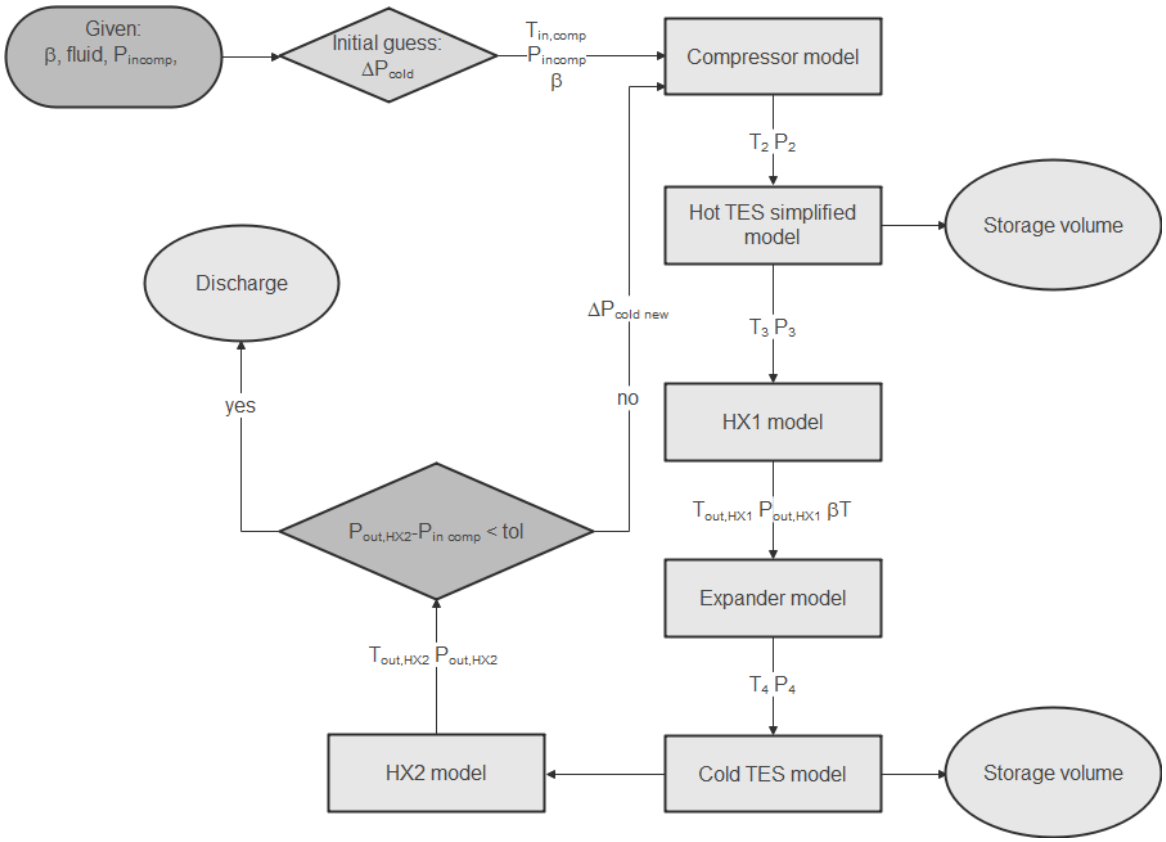

Fig. 3.8: Numerical routine for steady-state calculation, CHARGE

DISCHARGE

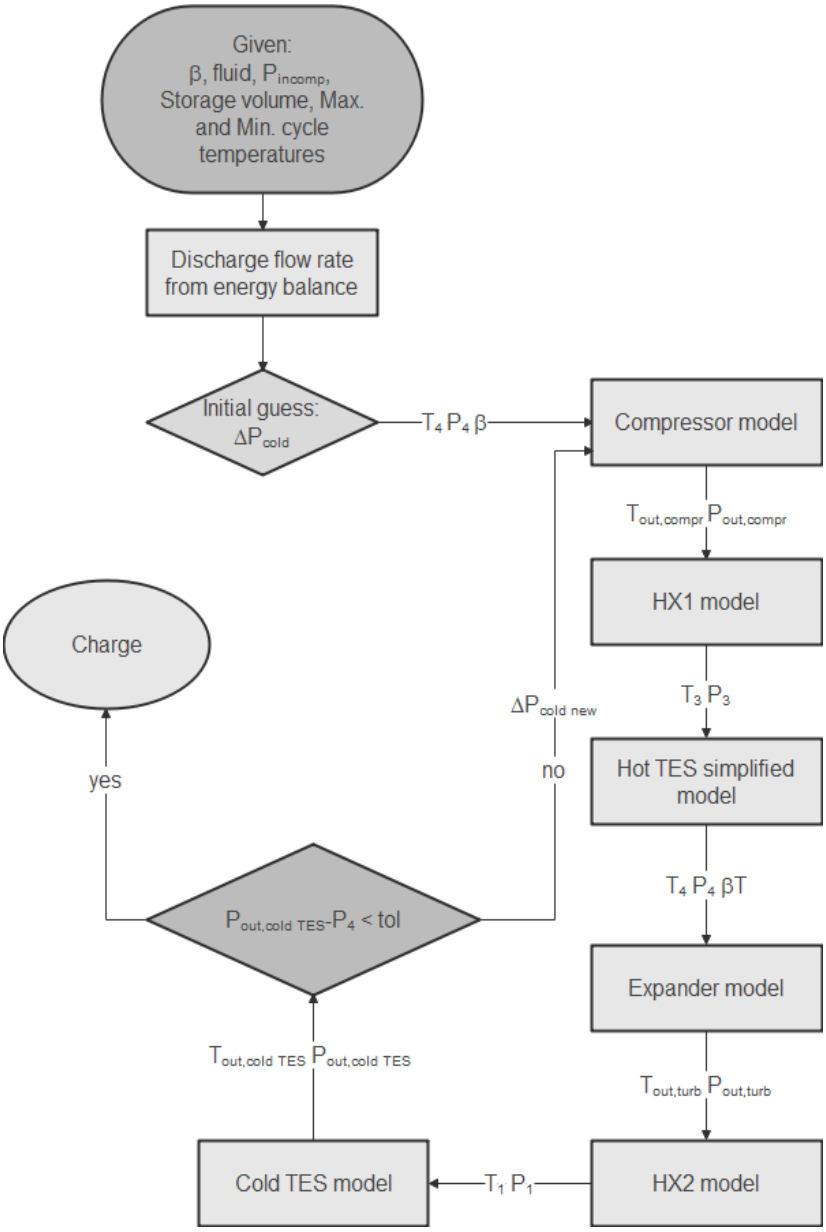

. 3.9: Numerical routine for steady-state calculation, DISCHARGE

Concerning the iterative process proposed in Fig. 3.8 and . 3.9, it is necessary to better specify some parameters and aspects that characterise the procedure and then clearly discuss the results obtained:

- The Argon mass flow rate is considered constant in each point of the system, and different from charge to discharge cycle to gain the specified discharge time, once the storage volume is fixed

$$\dot{m}_{disch} = \frac{(1-\varepsilon)c_s\rho_s\left(T_{out,bed} - T_{in,bed}\right)V_{tank}}{\left(H_{out,bed} - H_{in,bed}\right)t_{disch}} \quad (3.4)$$

- The minimum pressure of the system is set to 1.05 bar, to avoid the complication of running the plant with a minimum pressure lower than the ambient one, such as air infiltration
- Compressor and turbine thermodynamic transformation are described with the real adiabatic irreversible process, described by the value of isentropic efficiency. These can vary typically vary between 0.75÷0.94 for turbines and between 0.6÷0.92 for compressors depending on the size, type and application. Power is computed as $\dot{m}(h_{out} - h_{in})$
- The minimum storage volume for cold and hot TES is defined from the energy balance between gas and solid:

$$V_{min} = \frac{\dot{m}\left(H_{out,bed} - H_{in,bed}\right)t_{ch}}{(1-\varepsilon)\overline{c_s\rho_s}\left(T_{out,bed} - T_{in,bed}\right)} \quad (3.5)$$

The volume computed is the minimum since it is referred to an ideal heat transfer between solid and gas. If the heat front is perfectly vertical and ideally, it does not occupy space inside the tank and the storage volume is the lowest possible.

- The compression ratio (β), same for charge and discharge is variable from 5 to 26 to select the optimal configuration in terms of RTE, energy density, power density, considering feasible limitations on maximum and minimum temperatures of the cycle

- The total storage volume is divided into *N* parallel tanks, to increase reliability and limit pressure drops, since the flow rate passing through each bed (with same diameter *D*) will be the total one divided by *N*. A single storage volume is practically not feasible since the pressure drop will drastically decrease the RTE
- The ideal heat transfer in the packed beds assumes no temperature difference between the solid sphere and the working fluid, so the gas temperature in the outlet section of the bed equals the initial temperature of the solid bed
- Heat exchangers are considered counter-current, able to control the outlet gas temperature (assumed equal to 25°C), with a continuous flow of water.
- The diameter of the bed is chosen as the maximum diameter that can be transported by truck (4 m), to minimise the number of tanks and limit the pressure losses
- The pressure drop in a fixed bed of uniform spherical particles is evaluated employing the semi-empirical relationship known as Ergun's law [25]

$$\frac{\Delta P}{L_{bed}} = 150\frac{(1-\varepsilon)^2}{\varepsilon^3}\frac{\mu\, u_s}{{d_p}^2} + 1.75\frac{1-\varepsilon}{\varepsilon^3}\frac{\rho_g\ {u_s}^2}{d_p}\,[Pa] \qquad (3.6)$$

According to the Ergun equation, the pressure loss along the bed increases with the free stream velocity. When the fluid brings the entire weight of the bed to the waterline, the bed reaches the condition of incipient fluidization. Note that all thermo-physical parameters are dependent on pressure and temperature.

Results

The following results are obtained from this preliminary analysis: The effect of variation of isentropic efficiency, void fraction and particle diameter is analysed. Starting from general trends, as the compression ratio increases, the performance indices increase, due to a considerable increase in maximum and minimum cycle temperature. As far as the total storage volume is concerned, it increases slightly since the cold storage volume increases but the hot storage volume decreases (due to the dependence of the specific heat of the solid on the temperature), thus leading to an overall increasing trend in the energy density.

Turbomachine's efficiency

As isentropic efficiency increases at the same compression ratio, power density and RTE grow up; minimizing irreversibility in both machines is crucial for an efficient PTES. As the expander isentropic efficiency is reduced, a stronger drop in performance compared to a reduction in compressor efficiency is noticed, as depicted in Fig. 3.11 (a) and Fig. 3.12 (a). This is because irreversibility in the compressor leads to a higher outlet temperature than a theoretically perfect isentropic machine and some of the extra work required is converted to useful high-grade heat that can be stored during the charge phase. This is not the case for the expander where considering a real machine just results in a higher cold store temperature and less expander work on discharge, degrading turn-round efficiency on both counts. On the other hand, energy density increases with turbine efficiency as shown in Fig. 3.12 (b) and decrease as the compressor efficiency rises, due to a lower temperature at the discharge of the compressor and an increase in storage volume (both hot and cold), as a result of a lower specific heat capacity (Fig. 3.11 (b)). The values of maximum and minimum temperature are strongly dependent on compression ratio and isentropic efficiency: for a compression ratio higher than 20, with Argon as working fluid and with realistic values of efficiency, the maximum cycle temperature would exceed 820°C, while the minimum one would fall below -170°C, approaching the practical maximum temperature ratio within typically achieved industrial axial flow compressor pressure ratios (i.e., up to 30) [26].

Void fraction

The void fraction, which is a variable parameter independent of particle size, mainly influences the storage volume and pressure drop. The total storage volume increases, considering the same compression ratio. Power and energy density increase by increasing the void fraction (Fig. 3.14 (b)-(c)) at low pressure ratio, due to the higher "free space" inside the fixed bed, which decreases the pressure drop. For high pressure ratios instead, the increase in the storage volume overcomes the benefit in pressure drops, decreasing both indices. However, the RTE continuously increase since the reduction in pressure drops affect both phases (decreasing the work during charge).

Flow rate

From this preliminary evaluation, fixing the Argon flow rate at 50 kg/s, a compression ratio of 20 to limit temperatures, a void fraction of 0.4 and a particle diameter of 5 mm, it is possible to obtain a storage system with a nominal net power absorbed in the charging phase of 16 MW(heat exchanger relative pressure drops is considered 2%). To obtain a discharge time of 2h considering fixed storage volumes (calculated to charge the 16 MW system in 5 h), a flow rate of 125 kg/s is required. The ideal heat transfer in the TES system leads to a linear dependence between the speed of the thermal front and the flow rate. The increase in flow rate has two consequences: the first, is an increase in discharge power considering the same nominal compression ratio in the two phases

of storage (charging and discharging), the second is a considerable increase in pressure drop in the second phase due to the increase in the speed at which the gas crosses the storage volume. This leads to a decrease in the expected RTE compared to the case where equal charge and discharge times are considered (5 h), bringing the RTE from an expected value of 70.35% (with 5 h charge and discharge and 50 kg/s) to 64.73%.

Particle diameter

Considering instead the particle diameter, the larger the particle diameter, the lower the pressure drop and the higher the RTE as depicted in Fig. 3.16. Boosting particle diameter, although seems to be the best choice, creates problems in the real heat transfer process, increasing the Biot number and reducing the heat transfer coefficient between gas and solid (see 4).

Performance parameters

The performance parameters with the selected configuration are the following: RTE of 64.73%, ρ_E of 72.56 kWh/m^3 and ρ_P of 328.8 kJ/m^3. RTE and energy density are in line with expected values from Table 2.1.

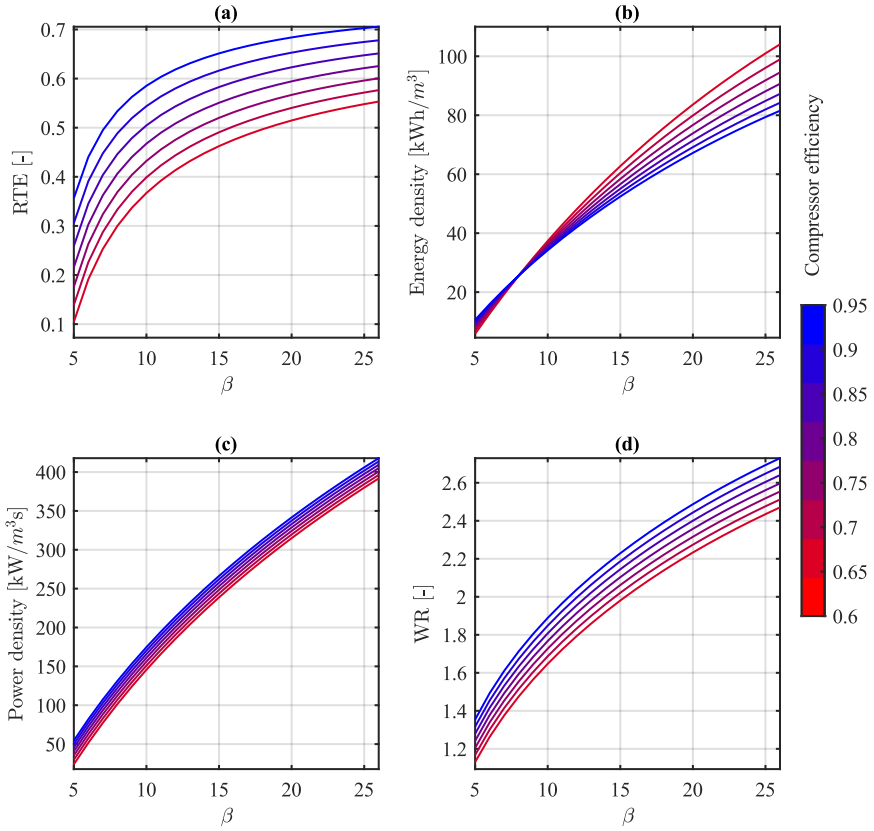

Fig. 3.10: Effect of compressor efficiency on a) RTE b) Energy density c) Power density d) WR during discharge

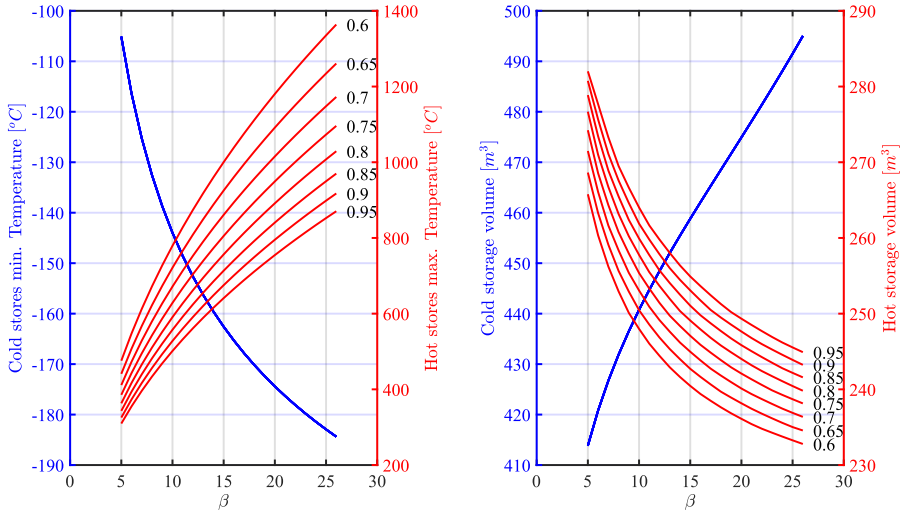

Fig. 3.11: Effect of compressor efficiency on a) Cycle temperatures b) Storage volumes

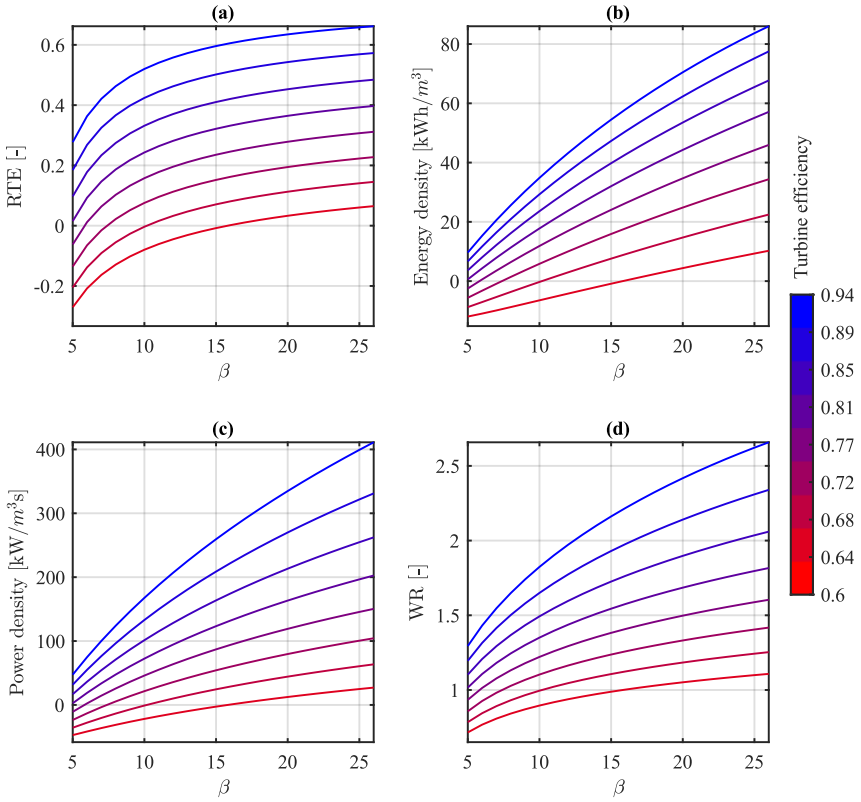

Fig. 3.12: Effect of turbine efficiency on a) RTE b) Energy density c) Power density d) WR during discharge

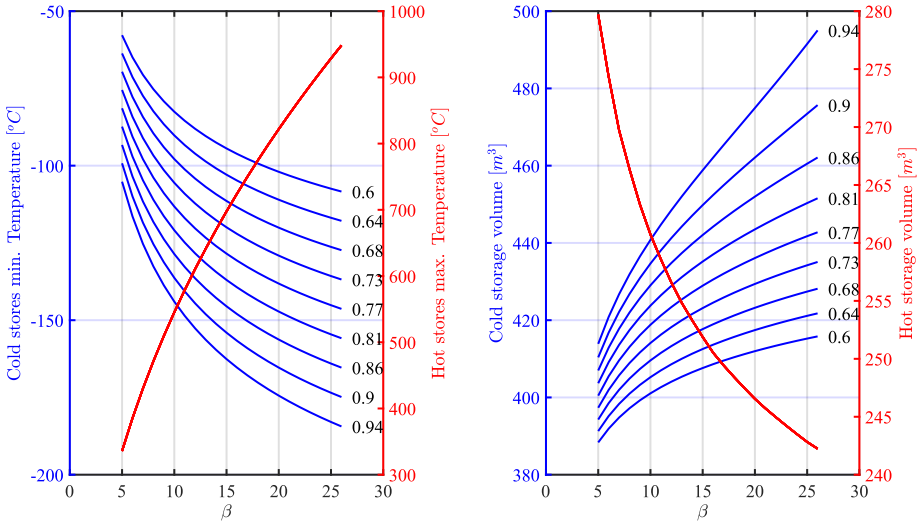

Fig. 3.13: Effect of turbine efficiency on a) Cycle temperatures b) Storage volumes

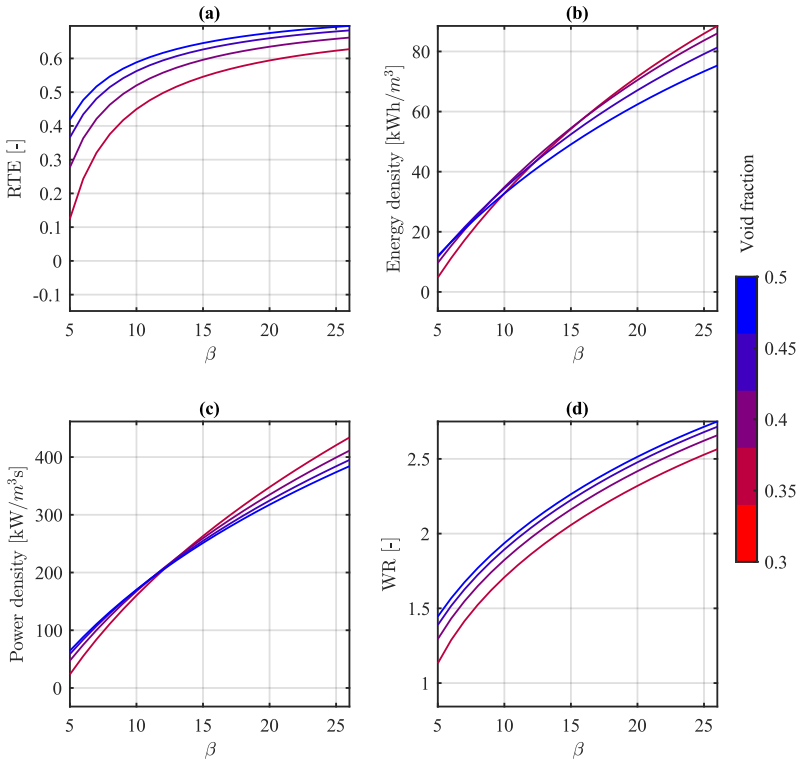

Fig. 3.14: Effect of the void fraction on a) RTE b) Energy density c) Power density d) WR during discharge

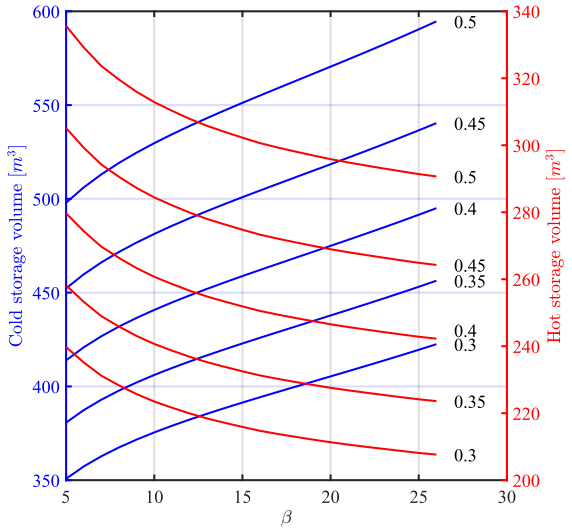

Fig. 3.15: Effect of the void fraction on storage volumes

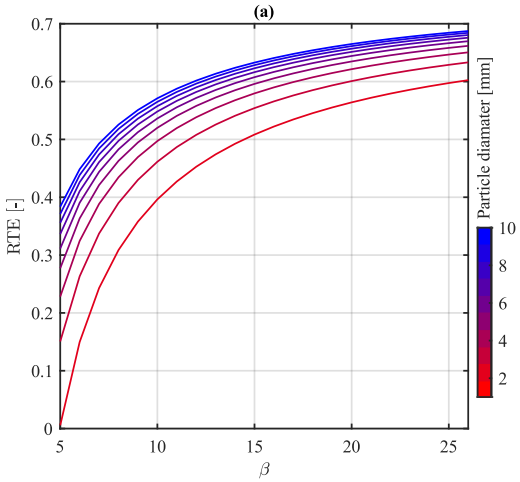

Fig. 3.16: Effect of particle diameter on RTE

The total storage volume is 250 m^3 for the hot side and 475 m^3 for the cold one, divided into 4-6 cylindrical tanks respectively. The higher cold tank number is mainly to reduce the flow speed and to limit pressure drop because of the lower gas density in the CR. The storage density for the latter is notably lower so that typically the CR needs to be about twice the size; this accords with the average solid heat capacity's being roughly a factor of 2 lower compared to the one in the HR. With this configuration, the maximum pressure drop found in the cold tank (higher stream velocity due to lower gas density) is around 0.369 bar (vs 0.0289 bar during charge), while the hot tank faces a pressure drop during discharge of 0.15 bar (vs 0.0278 during charge). With a total storage volume of 725 m^3 and with the temperature difference given by a compression ratio of 20, the ideal total energy stored in the tanks is about 130.37 MWh and the net one delivered by the expander during the discharge phase is 51.5 MWh.

3.2 Plant equipment

Each component of the storage system is treated and discussed in this section. In comparison with the previous section, the modelling, based on the basic design parameters provided previously, is more realistic and reliable. As far as turbomachines are concerned, the respective dimensionless operating curves, which establish the fundamental correlations between the main dimensionless parameters, are used to predict the behaviour in the off-design conditions (i.e., with a change in flow rate over time). Heat exchangers are solved as counter-current with the ε/NTU method, to provide the required parameters for accurate control of the gas temperature (which must be around ambient one). For the storage tanks, the pressure losses are calculated in the same way described

in the previous section while. Regarding the heat transfer, the displacement of the thermal front during the operation creates a dynamic regime, in which the mass of the system varies over time.

3.2.1 Compressor model

The compressors for energy applications, especially units over 5 MW, are axial-flow compressors. An axial-flow compressor is one in which the flow enters and exits in an axial direction (parallel with the axis of rotation). The machine compresses its working fluid by first accelerating and then diffusing to obtain a pressure increase. For a gas compressor, the functional dependence of outlet total pressure $P_{T,exit}$ and the isentropic compressor efficiency η_c can be expressed as a function of the following parameters:

$$\left(P_{T,exit}\ ,\ \eta_c\right) = f\left(\dot{m},\ P_{T,in},\ T_{T,in},\ n, \upsilon, \gamma, R, D, geometry\right) \qquad (3.7)$$

For a given family of compressors, for which γ, inlet diameter, gas constant and geometry do not vary, and at high enough Reynolds number (>3e5), β and η_c can be correlated in terms of reduced quantities:

$$\left(\beta_C,\ \eta_c\right) = f\left(\frac{\dot{m}\sqrt{T_{T,in}}}{P_{T,in}},\ \frac{n}{\sqrt{T_{T,in}}}\right) \qquad (3.8)$$

These quantities are dimensional but usually preferred when building this kind of maps. The similitude analysis helps in reducing the number of variables and considers the compressibility effects (rotational speed is coupled with temperature). The performance map of axial-flow compressors displays the variation of total pressure ratio across a compressor, as a function of reduced mass flow (usually expressed as a per cent of design value) and reduced speed (nr_c). The axial flow compressor adiabatic efficiency (η_c) is represented by different islands on the performance map, as shown in Fig. 3.17.

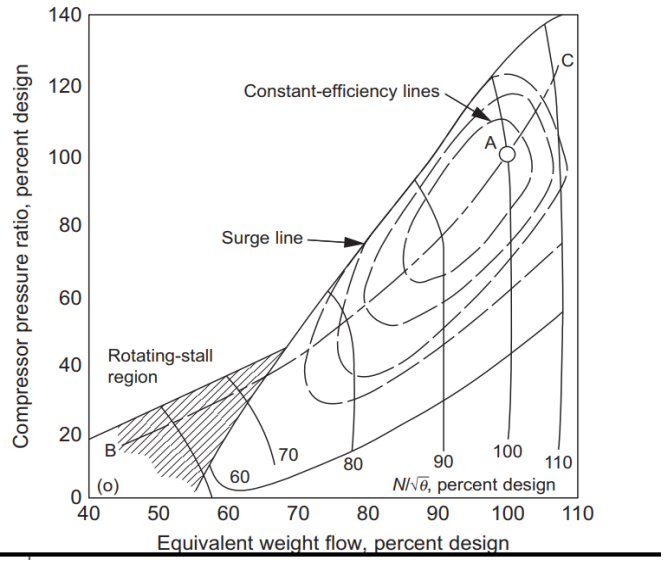

Fig. 3.17: The performance map of axial-flow Air compressors [26]

On a given reduced speed line, as the reduced mass flow falls, the pressure ratio increases until it reaches a limiting value on the surge line (i.e., nearly axial-symmetric) where the compressor tends to break down (flow becomes asymmetric with rotating stall) and can become violently unsteady[26]. These days numerous noble gases are progressively being utilized in compressors in different engineering fields. The Helium compressor can be coupled with high-temperature gas-cooled reactors (HTGR) for power generation and propulsion systems. Similarly, supercritical carbon dioxide (S-CO_2) can also be utilized in the compressor for generating electrical power. It is reasonable, when building such a map, to assume a compressor designed to operate with a special working fluid like Argon, whose operating curve will show a similar trend as the one of an air compressor, with some difference due to the difference in the specific heat ratio. Noble gases operating parameters and physical properties are in variance with Air, which is the reference working fluid for axial flow compressor design in major industrial applications. Turbomachinery operating with different gas have different performance characteristics, which have a significant effect on the overall performance of the power conversion system. Basic thermo-physical properties of Argon and Air are schematized in Table 3.4.

Table 3.4: Argon/Air thermo-physical properties

Fluid	**Gas constant [J/kgK]**	**γ [-]**	**MM [kg/kmol]**
Argon	208.1	1.667	39.948
Air	287.1	1.4	28.965

According to Tian et al. [27]-[28], the design criteria of the Air compressor can be applied to carbon dioxide or inert gases. However, based on the similarity criterion, one can observe that the heat capacity ratio is separate from the similarity condition. It is an essential factor that reflects the physical property differences of different working fluids. According to Tian et al. [28], the overall effect of an axial flow compressor stage, considering the same rotor design but with different working fluids are the following:

- Specific heat ratio has an important influence on the performance of the compressor rotor. The compressor with a higher specific heat ratio working fluid has lower adiabatic compression efficiency and higher total pressure ratio than that with smaller specific heat ratio working fluid given the same corrected flow rate
- The corrected choking mass flow rate of a compressor with different working fluids is independent of adiabatic compression efficiency and total pressure ratio and is only affected by the specific heat ratio of the working fluids. The corrected choking mass flow rate decreases with the increase of specific heat ratio

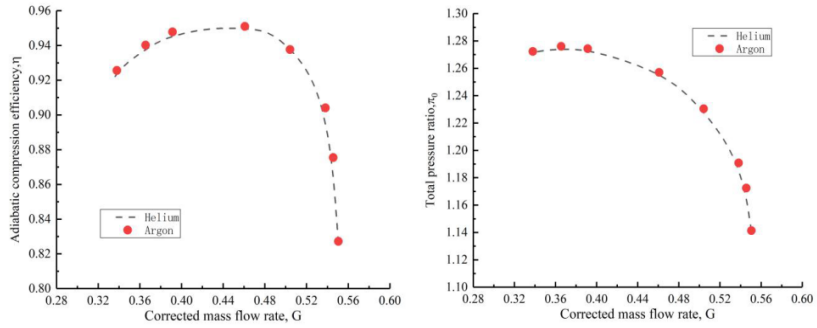

Fig. 3.18: Characteristics of the compressor rotor using Helium and Argon as working fluids [28]

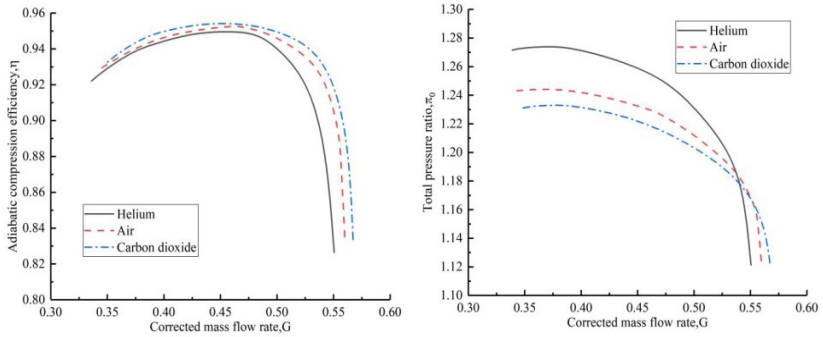

Fig. 3.19: Characteristics of the compressor rotor using Helium, Air, and carbon dioxide as working fluids: Efficiency characteristics, Pressure ratio characteristics [28].

As shown in Fig. 3.19, the adiabatic efficiency of compressor rotor is almost constant with the increase of specific heat ratio of the working fluid, while total pressure ratio increases, thus decreasing the overall number of stages, fixing the total pressure ratio of the machine. Considering the above conclusions, an Argon axial compressor map was built, as shown in Fig. 3.20 starting from the maps in Fig. 3.17.

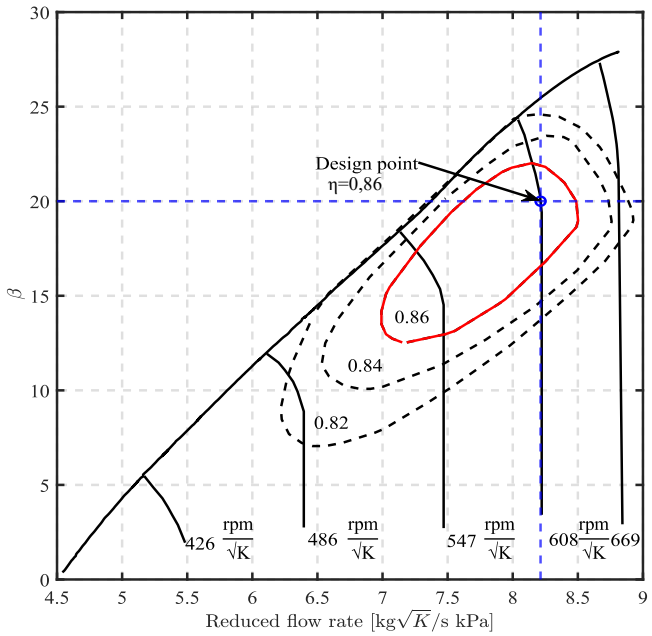

Fig. 3.20: Charge Argon compressor operating map in the reduced flow/ compression ratio plane: red line represents the selected efficiency island, while the blue dot is the design operational point

Adiabatic efficiency estimations, as well as nominal speed and mean diameter ones, are relevant and need to be discussed for sake of clarity. Given the inlet condition in terms of flow rate, pressure, and temperatures, assuming a total number of stages (considering a limit for compression ratio for the single stage[2]), it is possible to select a specific stage (typically the mid one) to be optimized in terms of specific speed and specific diameter[3]. Considering recent year trends for isentropic efficiency of the single compression stage, the optimized stage can reach efficiency up to 95% [28]. During the compression, not all the stages will be optimized in terms of specific speed and diameter. The specific speed reduces and specific diameter increases stage by stage due

[2] Maximum achievable pressure ratio for single stage assumed 1.35 for Argon vs 1.28 for Air

[3] Specific speed (ws)= $\frac{\omega\sqrt{\dot{V}}}{w_{is}^{3/4}}$, specific diameter (Ds)= $\frac{Dw_{is}^{1/4}}{\sqrt{\dot{V}}}$

to a decrease in volumetric flow rate, keeping in mind that for stationary applications typically heavy-duty single shaft machines are used to maximize the specific work (constant rotational speed). Considering a middle stage optimized, the overall efficiency of the machine is influenced by the compressibility effect and the stages before and after the middle one will be penalised. The design isentropic efficiency for the single optimized stage (mid one) is assumed 91%. The preliminary sizing is evaluated according to a design procedure developed in Excel® proposed by the author during a bachelor project, for the preliminary design of axial flow compressors, which considers different stage efficiency due to the change in volumetric flow rate, substituting design parameters for Argon and considering just the single-shaft configuration. For a more detailed description of the method, the reader can refer to here. The overall adiabatic efficiency can be assumed (from a simplified estimation) of 86% in design condition, which is reasonable for a single shaft compressor operating with a compression ratio of 20. Assuming an optimal specific speed and diameter in the middle-optimized stage respectively 2.3 and 2.1 (according to the Cordie line), the rotational speed and mean diameter result to be 10500 rpm and 0.695 m. Starting from the values under design conditions listed in Table 3.5, two different curves have been built, each one referring to the single machine operating in charge or discharge mode. The discharge compressor operates with different values of flow rate, compressor ratio and temperature, compared to the charge one. The optimal discharge compression ratio will be the main variable for the optimization of the delivery cycle (and so RTE when fixing the charge parameters) and the relative compressor characteristics will be described after that (Table 3.12).

Table 3.5: Baseline design parameters for charge compressor

Compressor parameter	Charge	
Inlet flow rate	50	kg/s
Inlet pressure	105	kPa
Inlet temperature	25	°C
Nominal pressure ratio	20	-
Nominal speed	10500	rpm
Mean diameter	0.695	m
Number of stages	13	-
Efficiency islands	86/84/82[4]	%
Nominal power	20.8	MW

The operation in off-design condition cannot be predicted with the Excel paper proposed and need to be studied separately. For sake of simplicity, according to [29], the efficiency in off-design condition, represented by the two different efficiency islands, is the nominal one reduced respectively by 3% and 5.5%.

[4] Assumed for off-design condition

Calculation model

The 0-D implemented model takes as inputs the compression ratio and reduced speed, giving as outputs the reduced flow rate and efficiency, from which all thermodynamic quantities at discharge can be evaluated. Specifically reduced speed lines are available for certain fractions of the nominal one; for different values a linear fitting is implemented, considering the surge limit.

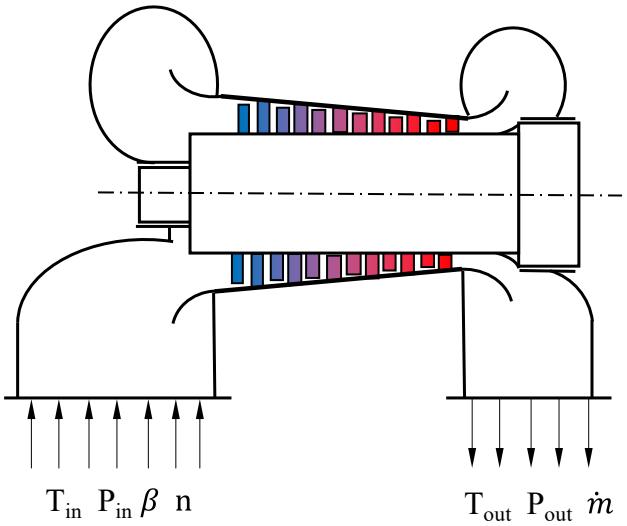

Fig. 3.21: Compressor model schematic

3.2.2 Turbine model

Similar to the axial compressors, also for axial flow expanders (turbine) of assigned geometry, given the properties of the motor fluid (and thus k, R, Cp,) a tern of values $\left(\frac{\dot{m}\sqrt{T_{T,in}}}{P_{T,in}}, \frac{n}{\sqrt{T_{T,in}}}, \beta_t\right)$ identifies operating conditions that comply with the similarity criteria. Therefore, for a compressible flow, the representation of the characteristics (work vs. flow rate) as the speed varies should be replaced by the more general representation of the characteristics:

$$(\beta_t, \eta_t) = f\left(\frac{\dot{m}\sqrt{T_{T,in}}}{P_{T,in}}, \frac{n}{\sqrt{T_{T,in}}}\right) \qquad (3.9)$$

The representation in reduced parameters allows giving greater generality to the plane of characteristic curves since the operating conditions of the turbine can be identified as the upstream

conditions vary. It should be remembered that gas or steam turbines are often brought to operate under conditions different from the nominal ones as a result of an adjustment in the operations, with consequent changes in inlet pressure and temperature. The reduced flow rate trend with expansion ratio is qualitatively like that found in flow through nozzles. Therefore, this flow pattern is subject to the flow blocking conditions if the unit Mach number (absolute or relative) is reached in one of the stator or rotor elements. All the considerations presented can be extended to multi-stage axial turbines, for which the coupling between the various consecutive stator and rotor elements determines the shape of the characteristic curves shown in the following figures [30]:

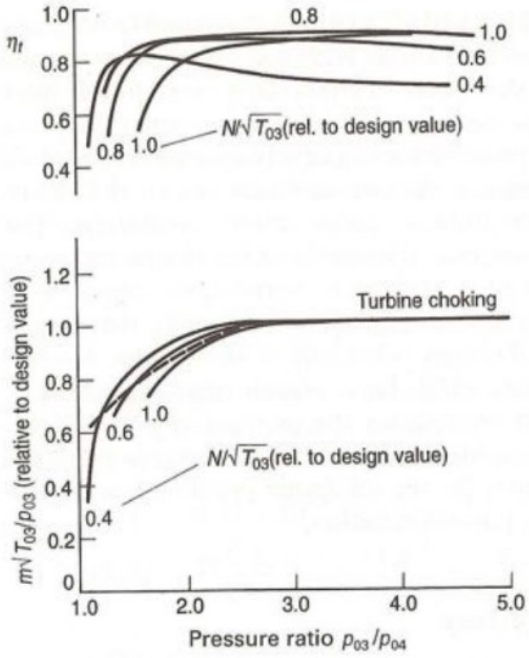

Fig. 3.22: Example of turbine operating map at fixed number of stages [30]

It is reasonable to assume, while building operating maps, as if we had a turbine built and optimised specifically for Argon as a working fluid. Since the isentropic turbine efficiency value is pivotal for a reasonable sizing of the cycle (both charge and discharge), it is worth analysing more in detail this component as done with the compressor. The validation of the turbine geometry and its equivalent resulting isentropic efficiency has been implemented using Axtur software, an *in-house* optimization code for axial flow and radial outflow turbines developed by professors Macchi and Lozza at the Energy Department of the Politecnico di Milano. For a more detailed

description of the software, the reader can refer to [31]. The results of the analysis computed by Axtur are the following:

Table 3.6: Baseline design parameters for charge turbine

Turbine parameter	**Charge**	
Inlet flow rate	50	kg/s
Inlet pressure	1950	kPa
Inlet temperature	25	°C
Nominal expansion ratio	18.5	-
Nominal speed	10500	rpm
Mean diameter	0,34	m
Number of stages	3	-
Nominal efficiency	93.58	%
Nominal power	5	MW

The rotational speed (referred to the compressor), type of fluid, flow rate, inlet pressure, temperature and number of stages are fixed input data. For the discharge phase, the final sizing will be treated later (Table 3.13). The equivalent isentropic turbine efficiency computed by Axtur is 93.58% for the charge phase. This analysis confirms the turbine efficiency estimated for the preliminary analysis of 94%. Considering the above outcomes, the characteristic curve of the expander is created, defined by the classic law of the ellipse in the compression ratio/reduced flow rate. The characteristic curves of the turbine in the charge (Fig. 3.23) and discharge phases have been constructed from the graph in Fig. 3.22, considering the variation of the dimensionless parameters in the two phases, but maintaining the same trend (as done for the compressor).

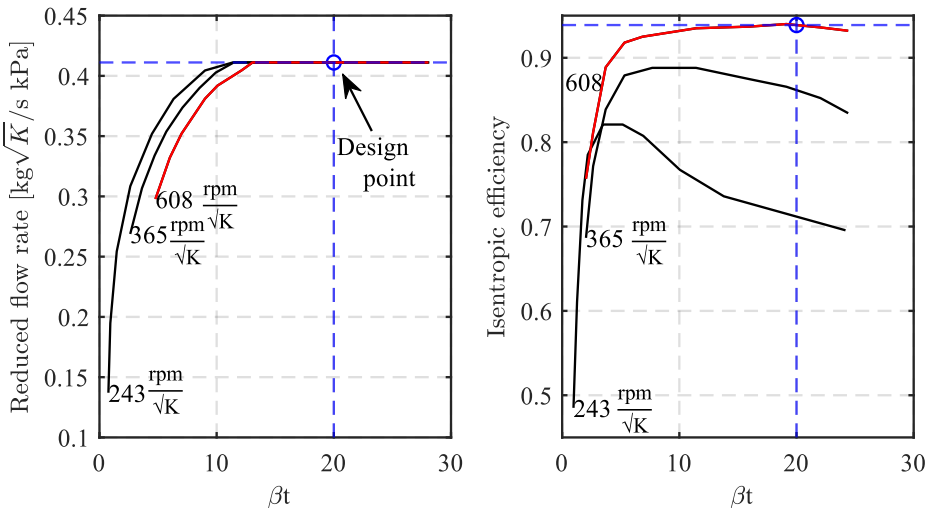

Fig. 3.23: Example of turbine's curves for charge mode

Calculation model

The 0-D implemented model takes as inputs the expansion ratio, inlet conditions and reduced speed, giving as outputs the efficiency and the inlet pressure that is needed with specific operating conditions. In this way, all thermodynamic quantities at the discharge of the expander can be evaluated. Specific reduced speed curves are available for certain fractions of the nominal one; for different values, a linear fitting is implemented.

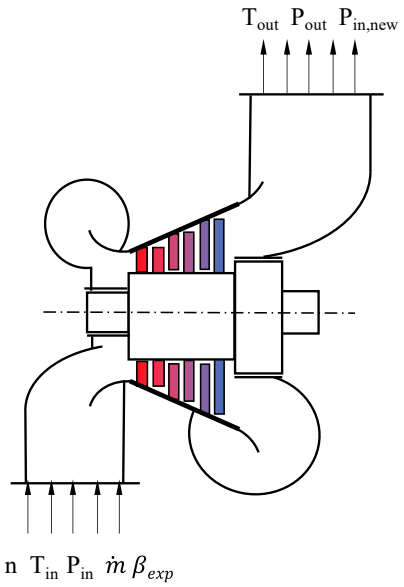

Fig. 3.24: Turbine model schematic

3.2.3 Packed bed ideal model

The reservoirs of interest typically comprise a cylindrical pressure vessel containing the solid storage medium in the form of a packed bed of pebbles of gravel in a uniform matrix of ceramic as shown in Fig. 3.25. The vessel is insulated both internally and externally and is arranged vertically to minimise buoyancy effects, with gas entering from the top for the hot reservoir (during charge) and from the bottom for the cold one.

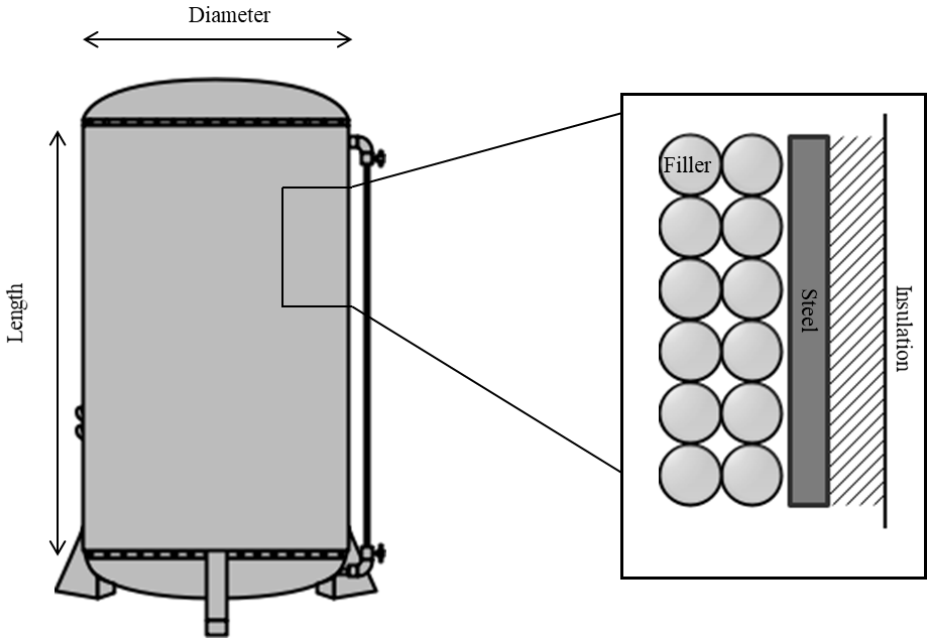

Fig. 3.25: Packed bed structure

Charging and discharging consist of shifting hot and cold regions in the tank by circulating heat transfer fluid through the solid storage medium. Plug flow is the ideal way of circulating HTF to prevent mixing and to keep well-stratified storage. Losses in the available energy stem from heat leakage to or from the environment, frictional pressure drop through the packed bed and irreversibility associated with heat transfer between the gas and solid. In the present work, heat leakage is assumed negligible, and the focus is instead upon heat transfer. This is justified since, in principle, any degree of insulation can be achieved. In this sub-section, a preliminary ideal heat transfer model for the CR and HR is proposed, which will be coupled with compressor, turbine, and heat exchangers model to simulate in Section 3.3 the dynamic behaviour of the storage plant during charge and discharge.

Solid media

The packed bed can be made of either structured, like in nuclear reactors, or non-structured solid filler. Non-structured filler enables to use of low-cost solids like pebbles. If a single size of spheroidal solids is used, the void fraction of the bed is typically around 0.3-0.4 [32]. Small solid size is preferable to improve stratification since it increases total fluid/solid heat exchange area and reduces the Biot number of solids. For stratification purposes, the Biot number of the particles has to be as low as possible so that heat transfer is only governed by convection ($Bi<0.1$), resulting in a sharper thermal front and better stratification. As long as fluidization is avoided, reducing

particle size also improves flow uniformity by increasing pressure loss and by preventing flow channelling near the walls. In cylindrical beds, this latter phenomenon can be avoided by respecting a minimum tank-to-particle diameter ratio of 30-40 [33]. To minimize the storage volume, given the temperature ratio and flow rate of HTF crossing the bed, high density and high heat capacity per unit of mass, as well as thermal stability and price are key parameters for a good filler. For this reason, Basalt is chosen to be the storage media. Its main properties, as well as the temperature-dependent specific heat capacity, are reported in Fig. 3.26 and Table 3.7:

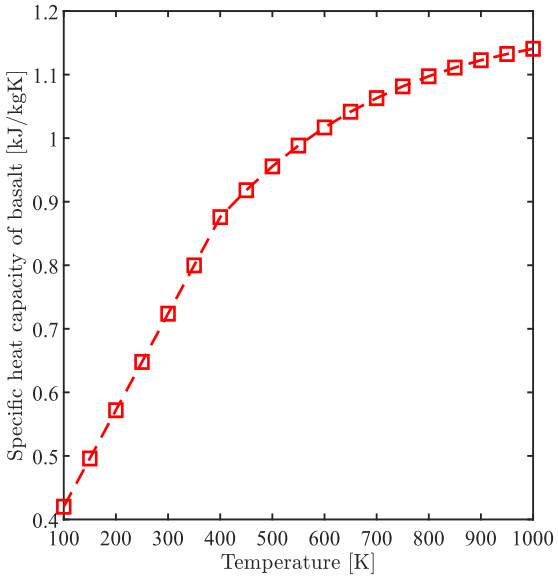

Fig. 3.26: Specific heat capacity of Basalt @(T) [34]

Table 3.7: Basalt properties

Property		
Density	3011	kg/m^3
Thermal conductivity (150 to 1000 K)	1,5	W/mK
Max. thermal expansion (1000K)	0,8	%

Thermal conductivity and density of the specified filler material can be assumed constant between maximum and minimum operating temperature according to [35]. Concerning the specific heat capacity, two different functions are extrapolated from experimental data [34] to better fit the heat capacity behaviour at different temperature range: from -170°C to 130°C a linear interpolation is

the actual best fitting, with the coefficients reported below. For data set between 130°C to 830°C, there is no longer a linear feedback with increasing temperature. The calorimetric data can be reproduced, within their error margins, with Maier–Kelley equations [36]:

$$C_s = a + bT + c/T^2 + d/T^{0.5} \text{ [J/kgK]} \quad (3.10)$$

Table 3.8: Coefficients of Maier-Kelley equation for Basalt

Coefficients from 100 to 400 K	
a	0.2681
b	0.001519
c	0.008797
d	-2,15e-05
Coefficients from 400 to 1000 K	
a	2.337
b	-0,0002773
c	22020
d	-29,76

Ideal thermocline

During the charging or discharging process, the heat transfer zone between gas and solid, called the thermocline, moves respectively downwards or upwards inside the storage. Upstream from the thermocline, a new zone at a relatively uniform temperature is generated. The outlet temperature of packed-bed storage is constant as long as the thermocline remains in the tank. During a typical operation, the thermocline has to "stay" inside the storage to keep the outlet temperature as constant as possible. Otherwise, the turbine or compressor would be respectively fed with increasing or decreasing fluid temperature (with relative efficiency drop). An ideal reservoir would be one for which there are no irreversibilities due to heat transfer or fluid friction. Thermodynamic losses associated with irreversible heat transfer will be reduced using very small particles and a high heat transfer coefficient, given the flow rate and specific heat capacity of the material. As $h \to \infty \; and \; d_p \to 0$, the gas-solid temperature difference disappears, and the progress of the thermal front is ideal.

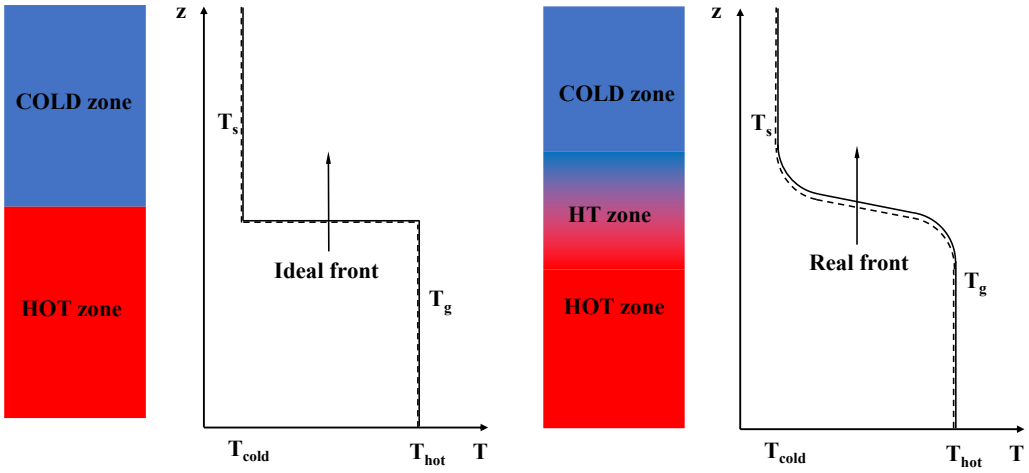

Fig. 3.27: Comparison between ideal and real thermocline

The nominal speed of the heat front can be computed as:

$$V_n = \frac{\dot{m}\overline{cp_g}}{N_{tank}A(1-\varepsilon)\rho_s\overline{c_s}} \qquad (3.11)$$

The position of the temperature wave at a time t after the beginning of charge is found by simply progressing each part of the initially discontinuous profile by a distance $z = V_n\, t$.

Mass imbalance

During the charge/delivery process, a large amount of gas is stored or released in the pore volume of packed beds due to the change in gas density owing to the translation of thermocline. In the PTES system, the density of Argon in the HR, considering a compression ratio of 20, decreases by 70.1 %, while that of the CR increases by 87.34 %; however, since the HR is pressurized, its mass variation is predominant, in absolute terms. The mass variation in the packed bed certainly causes an unbalanced mass flow rate between the inflow and outflow. In closed-loop PTES systems, this implies different gas flow rates between compressor and expander. A buffer vessel is required to store/release gas to stabilize the system pressure during charging/discharging, balancing the changes of mass in the two reservoirs, as shown in Fig. 3.28 and Fig. 3.29:

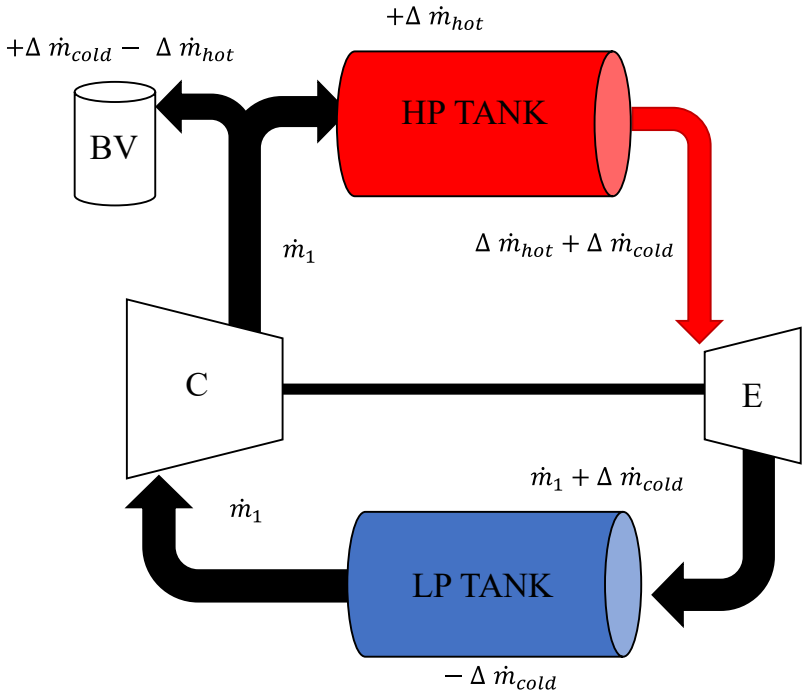

Fig. 3.28: Mass flow schematic during charge

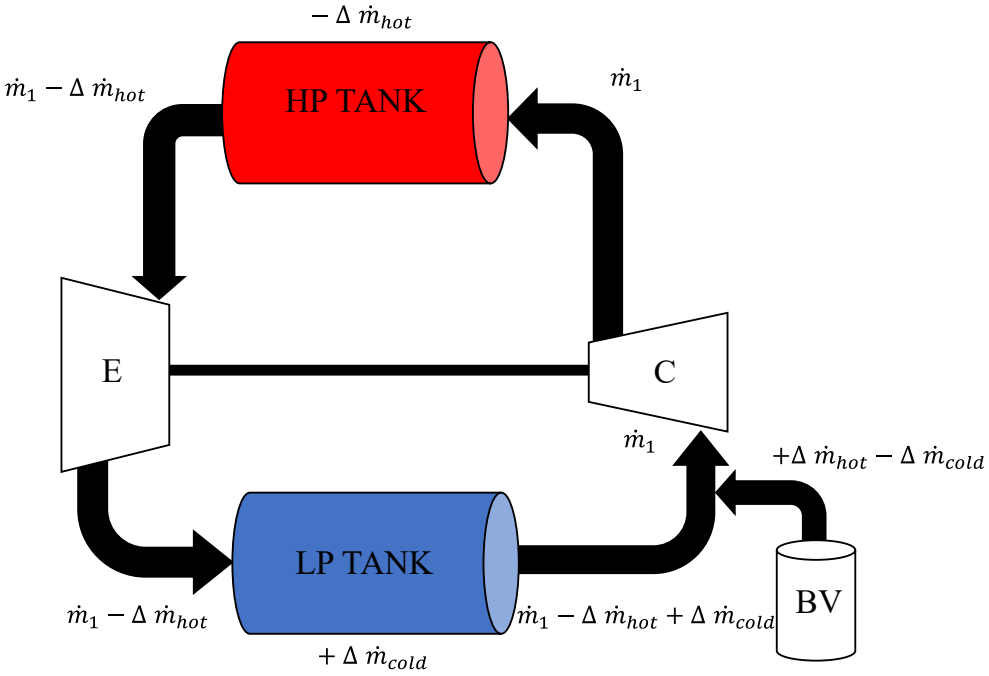

Fig. 3.29: Mass flow rate schematic during discharge

However, the flow imbalance, also according to Liang et al. [37], is relatively small but must be considered regarding the matching between turbine and compressor.

Calculation model

Considering an ideal reservoir, the implemented model's input and outputs are listed below:

Inputs	Outputs
$T_{in,g}$	$T_{out,g}$
$T_{in,bed}$	$P_{out,g}$
$P_{in,g}$	$M_{out,bed}$
Time (t)	outlet flow rate
$M_{in,\ bed}$	Charge or discharged energy at time=t

The calculation method takes into consideration only the temperature propagation effect on the overall density inside the tank:

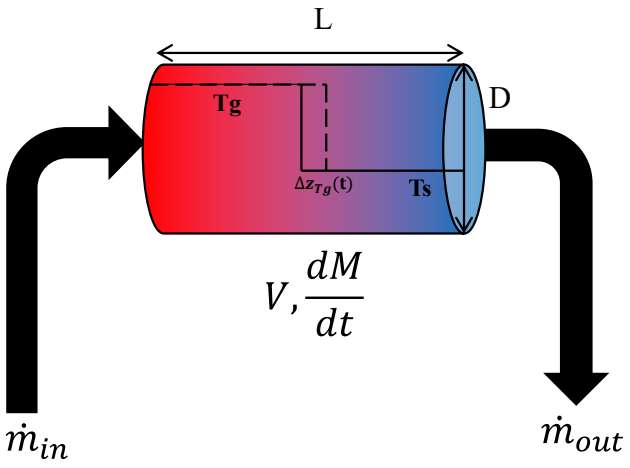

$$\dot{m}_{in} - \dot{m}_{out} = \frac{dM}{dt} \tag{3.12}$$

$$M = \int_0^L \rho_g(z,t) N_{Tank} \frac{\pi D^2}{4}\, dz \tag{3.13}$$

$$\dot{m}_{in} - \dot{m}_{out} = \frac{d}{dt}\int_0^L \rho_g(z,t) N_{Tank} \frac{\pi D^2}{4}\, dz \qquad (3.14)$$

An ideal reservoir would have no thermal resistance between the gas and solid, and the thermal front would remain as a step distribution from Tg to Ts, as it progressed through the reservoir. Straightforward energy balance gives the speed of the front as:

$$V_n = \frac{\dot{m}\overline{cp_g}}{N_{Tank} A(1 - \varepsilon)\rho_s \overline{c_s}} \qquad (3.15)$$

$$\Delta z_{Tg} = V_n(t - t_0) \qquad (3.16)$$

$$\rho_g(t) = \frac{[\rho_g(T_s, P_{tank})(L_{bed} - \Delta z_{Tg}) + (\rho_g(T_g, P_{tank})\Delta z_{Tg}]}{h_{bed}} \qquad (3.17)$$

$$\dot{m}_{in} - \dot{m}_{out} = \frac{L_{bed}\, \pi\, \frac{D^2}{4}[\rho_g(t) - \rho_g(t = t_0)]}{t\ -\ t_0} \qquad (3.18)$$

Concerning pressure drops and energy stored, these parameters can be computed in this manner:

$$E(t) = \int_0^L c_s(z,t)\rho_s(z,t)(1-\varepsilon)\pi \frac{D^2}{4} N_{Tank} \Delta T dz \qquad (3.19)$$

$$\frac{\Delta P}{L_{bed}} = 150 \frac{(1-\varepsilon)^2}{\varepsilon^3} \frac{\mu\, u_s}{{d_p}^2} + 1.75 \frac{1-\varepsilon}{\varepsilon^3} \frac{\rho_g\ {u_s}^2}{d_p}\ [Pa] \qquad (3.20)$$

3.2.4 Heat exchanger model

Without this component, cyclic operation between charge and discharge won't be possible since the bed initial temperature will increase with respect to the design one, due to the irreversibilities

related to the expansion and compression processes, as shown in Fig. 3.6. The schematization is shown in Fig. 3.30.

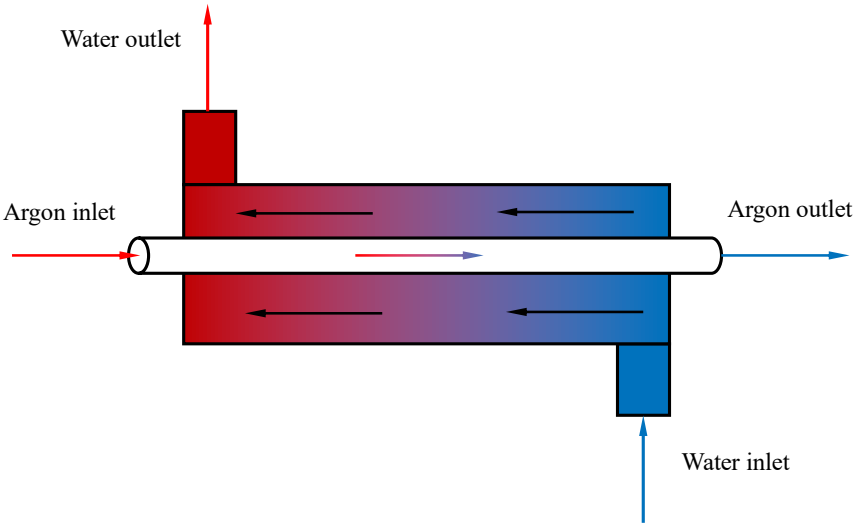

Fig. 3.30: Schematization of selected counter-flow configuration

High RTEs require a gas cooler with a heat transfer efficiency > 97%. The heat transfer efficiency is defined as:

$$\varepsilon = \frac{\dot{Q}}{\dot{Q}_{\infty}} = \frac{\dot{Q}}{(\dot{m}c_p)_{min}(T_{hot,in} - T_{cold,in})} \tag{3.21}$$

where $T_{H,in}$ and $T_{C,in}$ are the temperatures of the incoming currents, respectively hot (gas) and cold (water). $(\dot{m}c_p)_{min}$ is the lower of the thermal capacities of the flowing currents on the two sides of the exchanger, in this case, the gas one. The gas-to-ambient water heat exchanger is modelled using the effectiveness method. The number of thermal units (NTU) can be computed as follows:

$$NTU = \frac{UA}{(\dot{m}c_p)_{min}} \tag{3.22}$$

Where U is the overall heat transfer coefficient between the two fluids; typical values for forced circulation inside the heat exchanger for gas-liquid can vary between 20-250 W/m^{2}K based on the Dittus-Boelter Nusselt number correlation on each side and considering steel thermal resistance negligible. The effectiveness of the heat exchanger can be calculated following the steps below:

$$C_R = \frac{(\dot{m}c_p)_{min}}{(\dot{m}c_p)_{max}} \tag{3.23}$$

$$\epsilon = \frac{\left(1 - e^{(-NTU(1-C_R))}\right)}{1 - C_R\, e^{(-NTU(1-C_R))}} \tag{3.24}$$

$$T_{out,gas} = T_{in,gas} - \epsilon\left(T_{in,gas} - T_{in,water}\right) \tag{3.25}$$

Fixing a water flow rate of 50 kg/s, and an overall heat transfer coefficient of 0.07 kW/K, it is possible to achieve overall effectiveness of 98.2% for the worst condition (turbine discharge outlet with 1.1 bar pressure) with an overall heat transfer area of 5000 m^2.

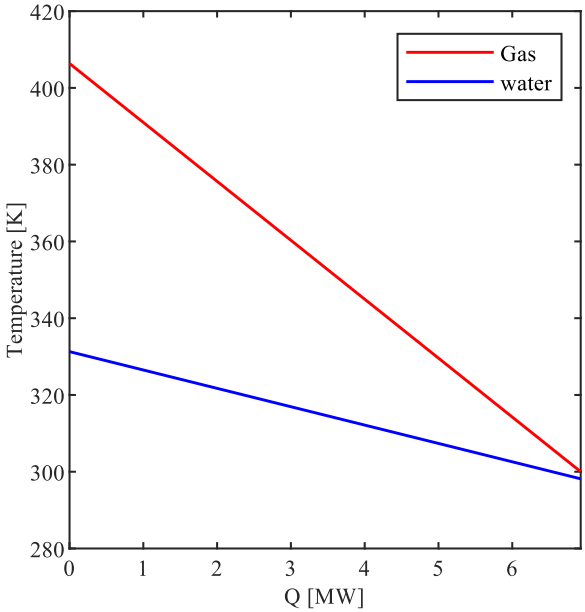

Fig. 3.31: T-Q diagram heat exchanger 2, referred to a compressor ratio β= 13

Buffer vessel

The buffer vessel is a key component for the correct operation of the plant. It is required because the total mass of gas within the two reservoirs changes during the charge and discharge period due to the average temperature variation along the reservoir. This will lead, if no flow rate is extracted or delivered from/to the system to undesired pressurization, with fouling problems. To stabilize the system pressure in a fixed point of the plant, which is chosen to be the inlet of the charge and discharge compressor (minimum pressure of the system), a certain amount of gas is delivered/extracted from the system depending on the net mass deficit or surplus between the two tanks. The hot storage contribution is predominant in the total change of mass since it is under high-pressure operation (at the beginning of a charge cycle, an overall mass of 2798 kg is enclosed inside it, which is 76.4% of the total). This leads to an overall decrease in the average density of the system as the hot tank heats up, and a consequential increase of pressure level. A removal of flow rate is required during the charging process and a supply during the discharge (density in the hot storage re-increases during this period). Moreover, a different pressure ratio of the compressor and expander during the charging and discharging processes can be obtained by adjusting the hot tank pressure using the same BV utilized for mass balance. By emptying or filling the tank with the additional gas from the BV, the pressure can be adjusted during the operation, and different pressure levels can be achieved during discharge to maximize the RTE; this point will be treated more in detail in 3.3.1. A single small buffer vessel can be used for the dynamic control of the entire system, operating with variable pressure and constant temperature (heat extraction will be necessary). During the charge phase, the BV will extract flow rate increasing its pressure, while during the discharge phase, if the pressure level is the same, the same amount of gas will be delivered again back to the system. If pressurization or depressurization will be needed, the BV has to be designed to fulfil the total amount of gas to sustain the four phases: extraction during charge, depressurization, delivery and again pressurization.

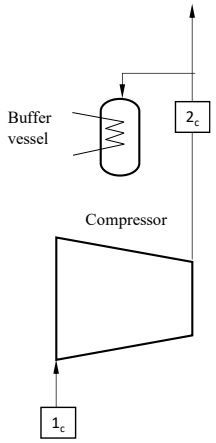

Fig. 3.32: BV schematic during charge

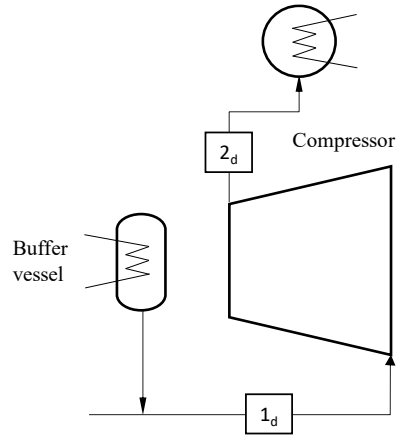

Fig. 3.33: BV schematic during discharge

3.2.5 Turbine-compressor fluid dynamic matching

Once the design of the machines has been defined, and the characteristic curves of the compressor and expander are known, it is possible to determine the operating point of the machine by solving the fluid-dynamic coupling of the components since, for big machines, both compressor and expander are placed on the same shaft. This means to evaluate the quantities (flow rates, pressures, temperatures, rotational speed) which make it possible to identify the operating point of each machine on its characteristic curve. The solution of the problem is strongly influenced by the configuration of the group: single-shaft or double-shaft and by the load curve: electric generator, operating machine, propellers. The case of a single-shaft machine for electric generation is examined as shown in Fig. 3.36. In this case, the parallelism of the generator ensures a constant rotational speed. Given the speeds to optimise the turbomachines, a transmission or generator with enough poles will be required to guarantee coupling at speeds greater than 3000 rpm. The characteristic curves of the compressor and turbine are usually shown graphically as a function of the reduced parameters as treated in the previous sections. Regarding the performance of the compressor, the characteristic curves provide the compression ratio as a function of the reduced flow rate for different values of the reduced speed. Also, the efficiency of the compressor can be represented as the compression ratio varies or as the reduced flow rate varies for different values of the reduced speed. The characteristic curve of the turbine instead presents a common trait characterized by the constant reduced flow rate that is realized when choking conditions are reached, while below the critical expansion ratio they differ with the reduced speed. Since the turbine frequently operates under choking conditions, it is reasonable to assume a single characteristic for the turbine $\frac{\dot{m}\sqrt{T_{T,in}}}{P_{T,in}} = K$,regardless of the small differences that occur at low

expansion ratios. Usually, in gas-turbine matching, the flow rate difference between compressor and turbine is negligible and it can be assumed the same for the two machines, but in the selected PTES configuration, the unbalanced flow rate in the tanks as well as the flow rate delivered from or to the buffer vessel to keep the minimum pressure constant alters this hypothesis and must be taken in consideration, even if the difference is small.

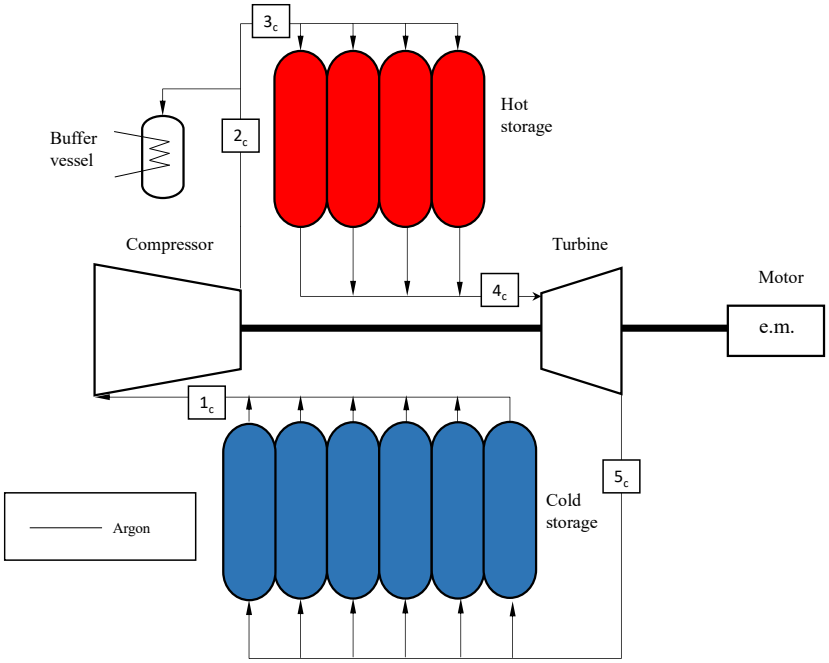

Fig. 3.34: PTES plant layout during charge

Considering the plant layout depicted in Fig. 3.34, in this sub-section a detailed description of the procedure applied to the determination of the equilibrium operating point of the system is presented. The iteration starts by arbitrarily fixing a point on the plane of the compressor, considering fixed rotational speed; in this way, the following parameters can be evaluated immediately:

$$\left(\frac{\dot{m}\sqrt{T_{T,1}}}{P_{T,1}},\ \frac{N}{\sqrt{T_{T,1}}}, \beta c, \eta c\right)$$

Remember that turbine and compressor inlet temperature are set by the initial condition of the tanks during the two different phases; after the heat exchange between gas and solid, the outlet gas temperature corresponds to the initial temperature of the solid if the thermocline remains inside

the tank itself. It is possible, once calculated the pressure losses of the hot storage (from the thermodynamic state at compressor outlet), assumed those in the cold storage together with the flow rate to/from the buffer vessel, to report the turbine curve on the compressor plane as:

$$\frac{\dot{m}_4\sqrt{T_{T,4}}}{P_{T,4}} = K \tag{3.26}$$

$$\beta = \frac{\dot{m}_{rid,c}(1 + (\Delta\dot{m}_{BV} - \Delta\dot{m}_{HOT,tes})/\dot{m}_1)\dfrac{\sqrt{T_{T,4}}}{\sqrt{T_{T,1}}}}{K(1 - \dfrac{\Delta P_{HOT,tes}}{P_2})} \tag{3.27}$$

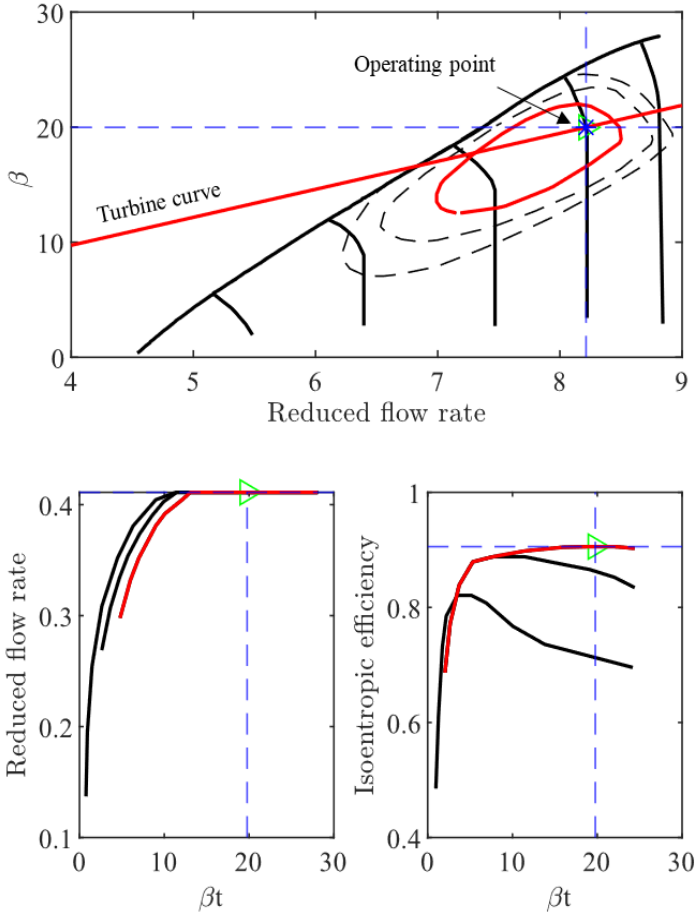

Fig. 3.35: Turbine's curve represented in the compressor plane

in this way, it is possible to determine graphically the value of the compression ratio that represents the only degree of freedom of the system. However, this procedure is not that smart to apply due to computational time: the turbine curve depends on the flow rate to/from buffer vessel, which is computed iteratively since the unbalance flow rate in the tanks depends on the heat front speed, that depends on the inlet thermodynamic quantities, which are not known a priori and need to be verified with the fluid-dynamic matching. For this reason, an iterative step-by-step procedure (Fig. 3.37) has been implemented, following the same logic as the graphical determination, and considers the convergence of the flow rates and pressure values. The procedure is the same for charge and discharge, considering the additional heat exchangers and the different input design parameters. Indeed, the compressor will set the flow rate, while the turbine the pressure ratio as shown in Fig. 3.36.

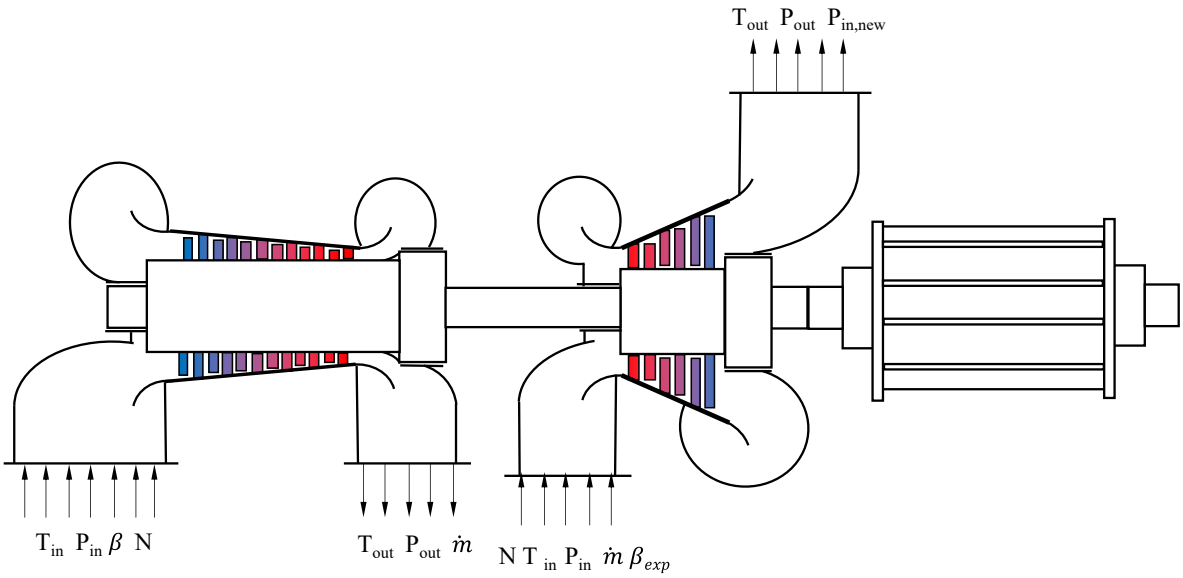

Fig. 3.36: Compressor/turbine matching scheme

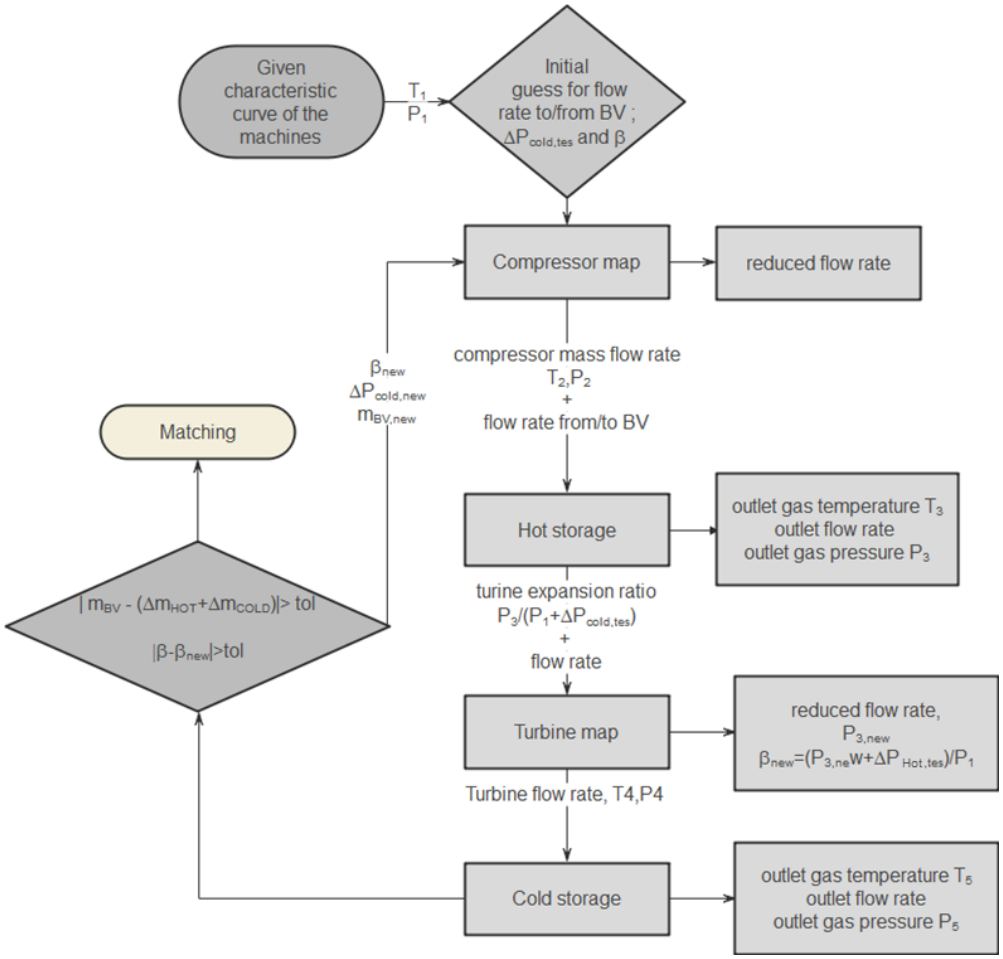

Fig. 3.37: Computational schematic for turbine-compressor matching for PTES system during charge

3.3 Dynamic analysis

In the following section, the operation of the system in dynamic regime will be analysed, considering the parameters listed in Table 3.9. The models of the various components are those described before and will not be commented on further. Setting same the pressure ratio of the compressor between charge and discharge may not be the best choice. After the charging process, the compression ratio of the delivery can be reset by storing some gas in the BV and recharging the system by the adjustment compressor during the idle time. The purpose of this analysis is to investigate the behaviour of the operating parameters during the time and to set the optimal compression ratio in the discharge phase which maximises the RTE. The calculation scheme and the modelling of the pressurisation/depressurisation are given in the following section.

Table 3.9: Outline design parameters from steady state analysis

Ambient		
T_{amb}	298.15	K
P_{amb}	1.01325	bar
Packed bed		
Filler	Basalts	
ρ_s	3011	
d_p	5	mm
c_s	c_s (T_s)	J/kgK
D	4	m
N° vessels (cold/hot)	6/4	-
Cold storage volume	250	m^3
Hot storage volume	475	m^3
ε	0,4	-
ψ	1	
Compressor and turbine		
Process	Operating map	
Isentropic Efficiency	Operating map	
Fluid		
Working fluid	Argon	
Properties	Refprop®	
Nominal flow rate in charge mode	50	kg/s
Nominal flow rate in discharge mode	125	kg/s
Heat exchanger		
$\Delta P\%$	2	%
$T_{out, gas}$	298.15	K
Cooling medium	Water	-
Plant characteristics		
Nominal compression ratio during charge	20	-
Expected net power absorbed during charge	16	MW
Delivered power during discharge[5] (same β with respect to charge)	25.8	MW
Expected RTE	64.73	%
Expected ρP	328.8	kJ/m^3
Expected ρE	72.56	kWh/m^3
Nominal charge time	5	h
Nominal discharge time	2	h

[5] The word “expected” is used taking into consideration the possible change in the efficiencies described in the next section

3.3.1 Pressurization and depressurization

Once the charging phase is over, which takes place with a compression ratio of 20 (considering the results obtained in section 3.1.2), to vary the one in the discharge phase it is necessary to think of a system able to depressurise and subsequently repressurise the hot tank, which is always at maximum pressure. The following scheme is proposed for this task:

To pressurise/depressurise, two flows are sufficient:

- During the depressurisation of the hot storage tank, the BV is pressurised by receiving Argon from the discharge compressor, see Fig. 3.38
- During the pressurisation of the hot storage, the BV discharges Argon at the inlet of the charge compressor by pressure difference, see Fig. 3.39

The gas tank (BV) serves both to balance the pressure upstream of the compressor during operation and to pressurise/depressurise the hot storage during the charge/discharge phases.

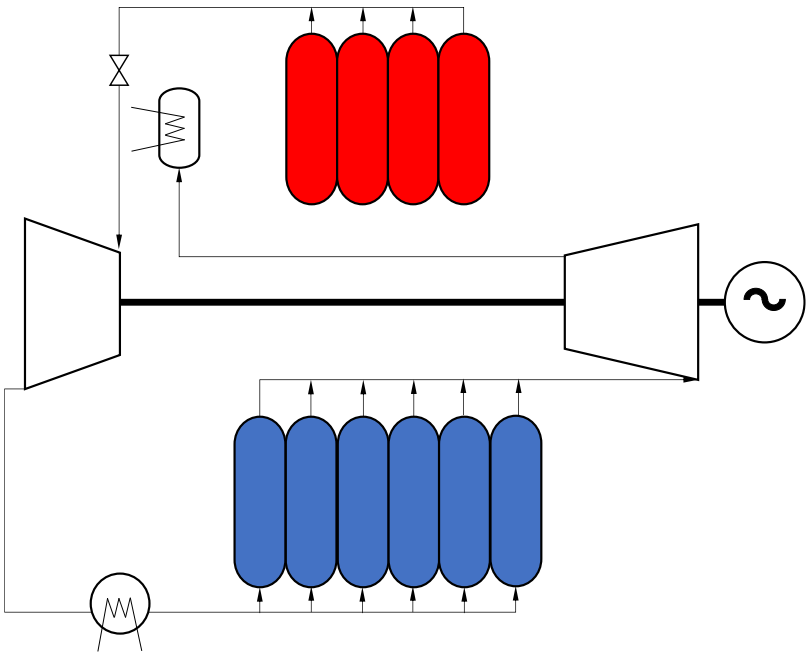

Fig. 3.38: Depressurization scheme

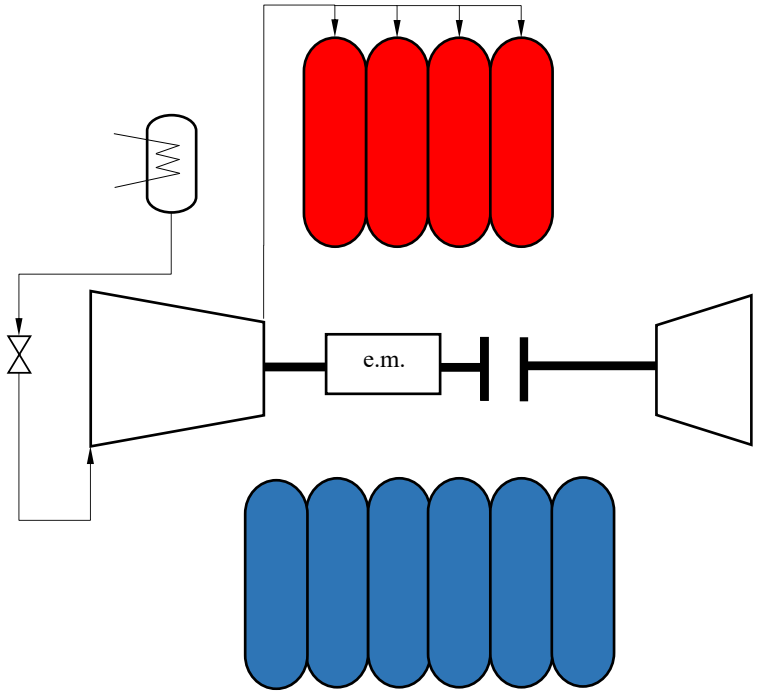

Fig. 3.39: Pressurization scheme

In the depressurisation phase, there is no matching between the compressor and turbine, because the flow processed by the compressor does not enter the expander, but enters directly in the tank. It would be useful to put a valve to laminate the pressure at the turbine inlet to the nominal one. The flow rate of the compressor is determined by the speed of rotation and the pressure at the outlet, which is the pressure in the BV with the addition of any pressure drop imposed by a control valve. During pressurization instead, a clutch joint is needed to separate the compressor from the turbine. The flow rate of the compressor is again determined by the speed of rotation and the pressure at the outlet, which is the pressure in the hot tank with the addition of any pressure drop imposed by a control valve. The important thing is to have the machines rotating at nominal speed (assumption). Doing a complete dynamic analysis of the system would be a mess since the acceleration ramp of the shafts would be considered. Therefore, the size of the tank must be set to accommodate the mass difference between the two phases. An immersed exchanger in the BV is necessary to keep it at ambient temperature regardless of the condition. When the tank fills up, it tends to heat up because it receives hot flows that increase the inside pressure. When it empties instead, it tends to cool down. The total volume of the BV can be computed as:

$$\Delta M_{BV} = \varepsilon \left[\left(V_{hot,TES} (\rho(T_{in,bed}, P_{tank,hot,charge}) - \rho(T_{g,in}, P_{tank,hot,charge}) \right) + \left(V_{cold,TES} (\rho(T_{g,in}, P_{tank,cold,charge}) - \rho(T_{in,bed}, P_{tank,cold,charge}) \right) + \left(V_{hot,TES} (\rho(T_{g,in}, P_{tank,hot,charge}) - \rho(T_{g,in}, \beta_{dis,max} P_1) \right) \right] \quad (3.28)$$

$$V_{BV} = \frac{\Delta M_{BV}}{\rho(T_{amb}, \beta_{dis,max} P_1{}^6)} \quad (3.29)$$

Hot tank pressure determination

The following scheme in Fig. 3.40, reports the procedure to compute the hot tank pressure during operation of pressure adjustment:

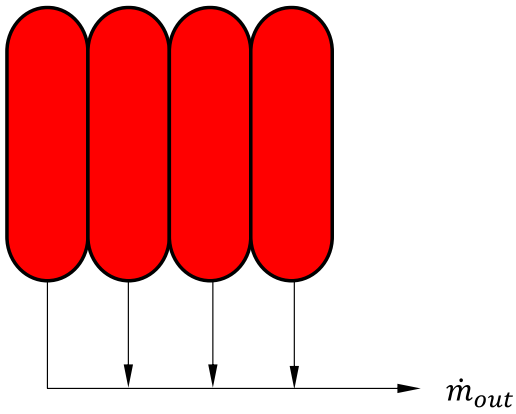

Fig. 3.40: HP tank pressure variation scheme

$$\frac{\partial U}{\partial t} = -\dot{m}_{out} h_{out} \quad (3.30)$$

[6] The maximum pressure of the BV is chosen to be the maximum one achievable by the discharge compressors to avoid stall problem during the depressurization of the hot tank

$$U = V_{tank}\left[\rho_s(1-\varepsilon)\left(T - T_{ref}\right)c_s + \rho_g\varepsilon\left(T - T_{ref}\right)c_{v,g}\right] \quad (3.31)$$

$$\int_{T_{in}}^{T_{fin}} \partial U = \int_0^t -\dot{m}_{out}h_{out}dt \quad (3.32)$$

$$\frac{M_{in,g} - \dot{m}_{out}t}{V_{tank}} = \rho \xrightarrow[then]{} \frac{P}{\rho} = R_g T_{fin} \quad (3.33)$$

When emptying/filling the hot tank, the process is close to be isothermal. Considering the scheme reported above, when a mass flow rate is drawn or injected into a finite volume of gas, the system not only increases/decreases its pressure but also heats up/cools down according to the direction and temperature of the flow. In the specific system treated in this thesis, however, the increase/decrease in temperature is negligible since the internal energy of the solid predominantly influences the internal energy of the entire system. A variation of the mass of gas during pressurization/depressurization leads to a variation in temperature less than 1°C considering a compression ratio of 20. It is therefore correct to directly correlate a decrease/increase in density of the hot storage with an increase/decrease in pressure (at constant temperature) inside it through the ideal gas law.

3.3.2 Sensitivity analysis: dynamic regime

Based on the standard parameters in Table 3.10 and the modelling methods for the single components described in this chapter, the working behaviour of the PTES system running for a complete charge/discharge cycle dynamic regime is simulated.

Table 3.10: Dynamic analysis design parameters

Nominal compression ratio during charge	20	-
Nominal pressure ratio during discharge	From 13 to 19	-
Nominal charge time	5	h
Nominal discharge time	2	h

The numerical routine is again iterative and takes into consideration the convergence for the pressure losses values, flow rate delivered to/from the BV and compression ratio from the

matching between turbine and compressor. The procedure is described below in Fig. 3.41, and it starts once the user has defined the charge and discharge times for the cycle and the initial state of the beds. If for example only one discharge cycle is required, it is necessary to define the temperature profile at the beginning of such period, which will be the last temperature profile of the previous cycle. The iterative procedure is the same as the one described for the fluid-dynamic matching between the turbine/compressor unit. The results of the simulation with varying compression ratios in the discharge phase are shown and analysed in terms of compression ratio, expansion ratio, pressure losses and variations of the mass in the storages and BV. The objective remains to maximise the round-trip efficiency of the system.

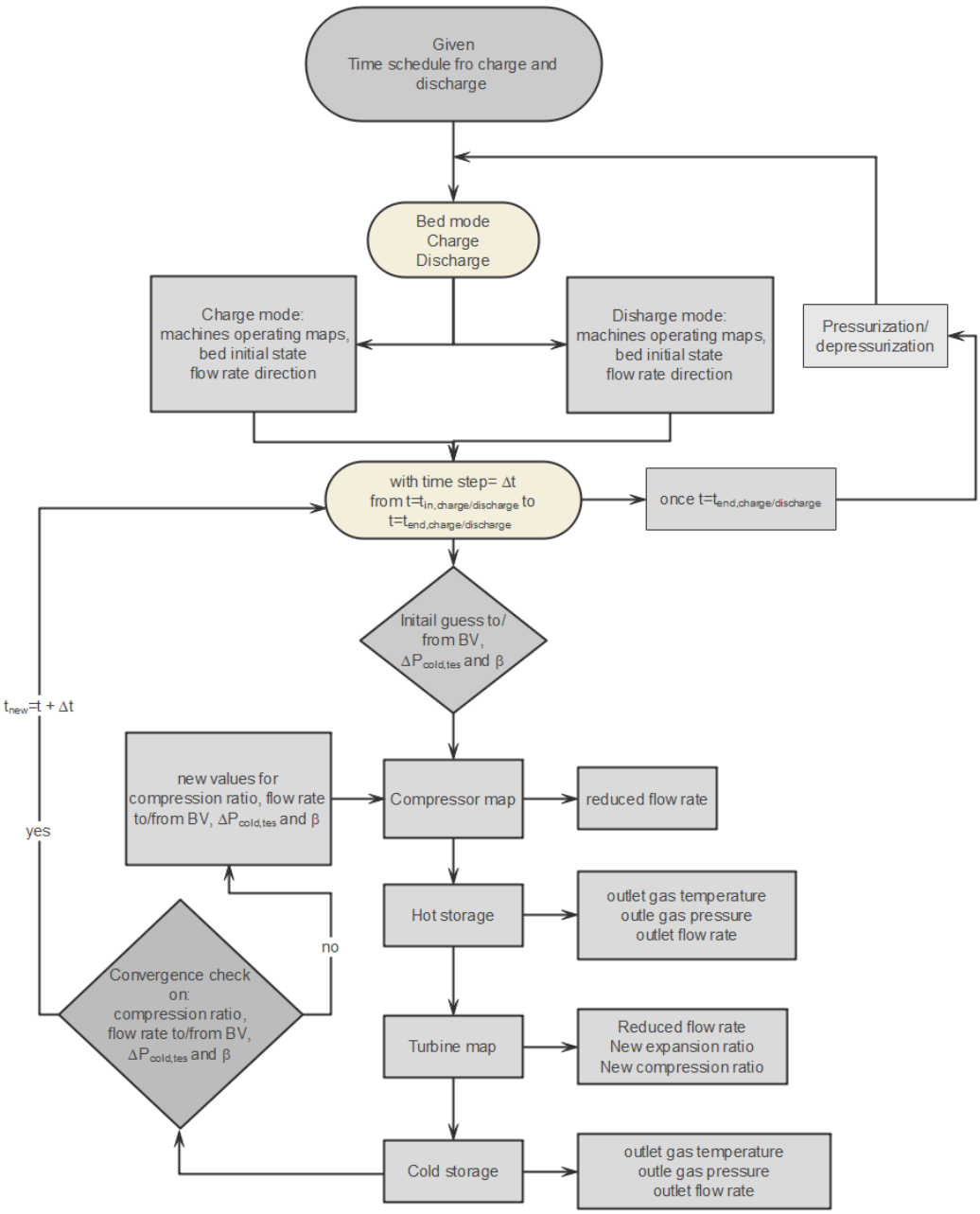

Fig. 3.41: Numerical scheme for dynamic simulation

3.3.3 Results and discussion

It can be found that the pressure loss in the CR decreases during the charging and increases during the discharging process, while the opposite phenomenon is observed in the case of the HR (Fig. 3.42 and Fig. 3.43). This is because, during the charging period, the cold region in the CR grows gradually, owning to higher density which results in a decrease in the pressure loss. During the discharging process instead, the cold region retracts gradually, and the pressure loss increases. For similar reasons, the increase of the hot region in the HR leads to a higher volume flow rate, hence increasing the pressure loss during the charging and decreasing it during the delivery. The rate of variation during time is dependent on the temperature and pressure level of the reservoir and on the inlet flow rate of the working fluid, once fixed the geometrical parameters of the two reservoirs.

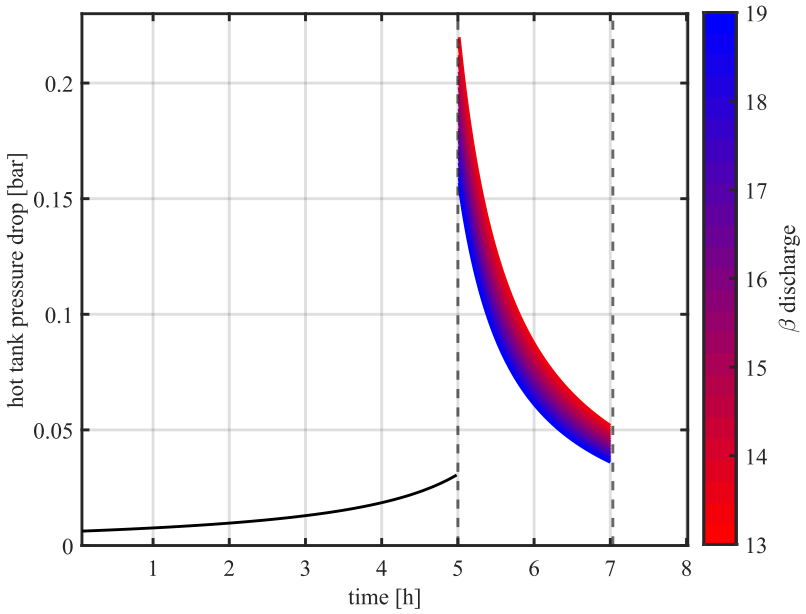

Fig. 3.42: Hot tank pressure drop

It can be also observed that the different number of vessels between CR (6) and HR (4), helps in reducing the difference in magnitude between the pressure drops during the operation.

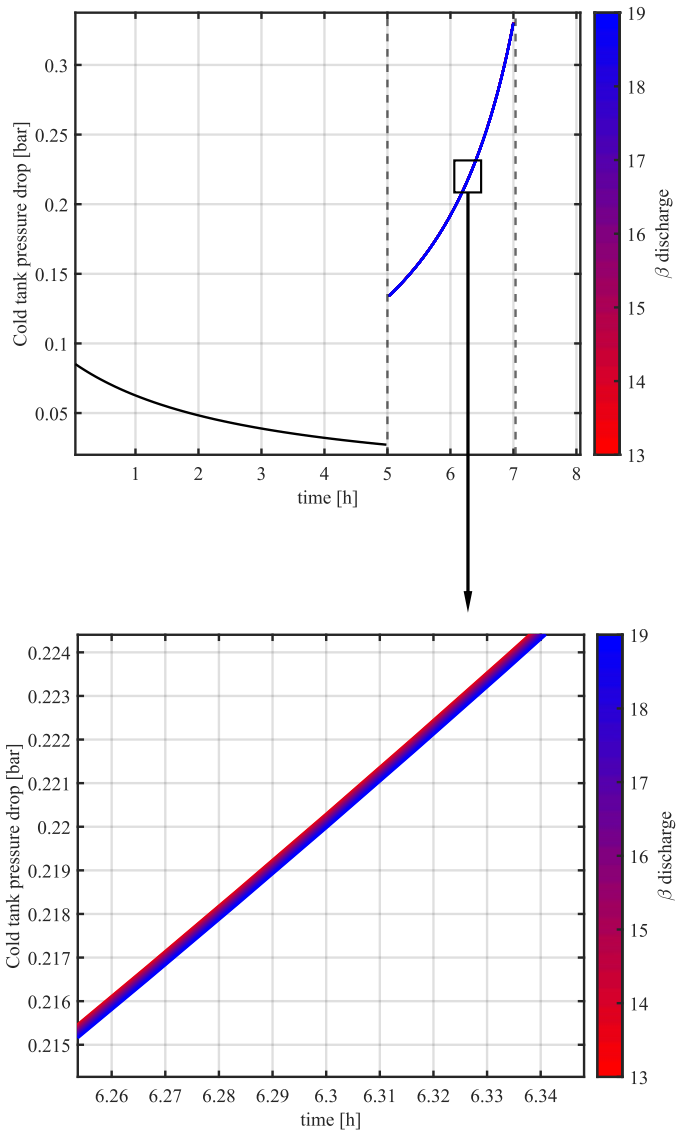

Fig. 3.43: Cold tank pressure drop

Since the minimum cycle pressure is not influenced by the compression ratio, the pressure losses inside the CR are practically independent of this parameter. The discontinuity shown at the charge/discharge ending time, are due to pressurization and depressurization, which re-establishes the pressure level and, consequently, the value of the related parameters depending on the pressure selected. The pressure ratios trend over time are shown in Fig. 3.44 and Fig. 3.45, and their variation is influenced by two different parameters: flow rate difference and pressure losses. Keep in mind that the temperatures at the inlet of the machines are constant due to the ideal thermal

front that propagates inside the bed. The mass flow imbalance between the two machines stays always below 0.25 kg/s, and its effect on the matching between turbine and compressor is minimal (Fig. 3.46)[7]. During the charge period the mass flow rate processed by the turbine is slightly higher than the one of the compressors; combining this information with the trend of the hot tank pressure drop, the compressor ratio is rather stable. The expansion ratio instead increases due to a decrease in cold tank pressure drop and a slight increase in the flow processed. Similar deductions can be done for the delivery period with inverse trends.

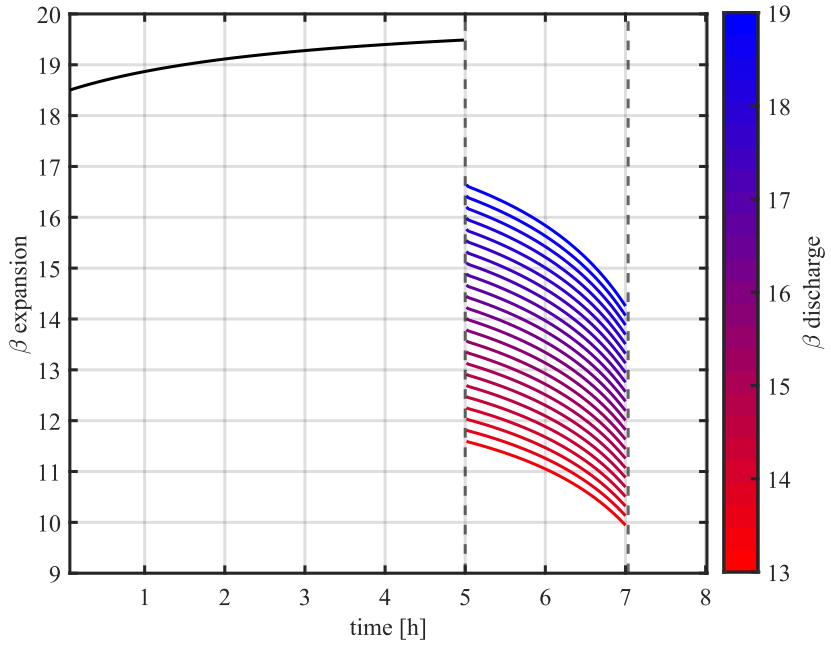

Fig. 3.44: Expansion ratio

[7] The net unbalanced flow rate in Fig. 3.46 is the net sum of the differences between inlet and outlet flow rate in the two reservoirs.

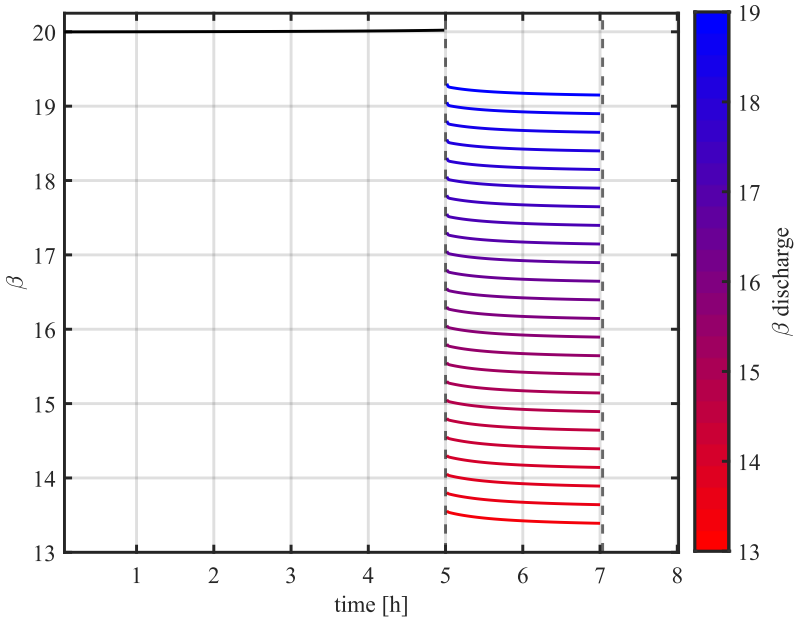

Fig. 3.45: Compression ratio

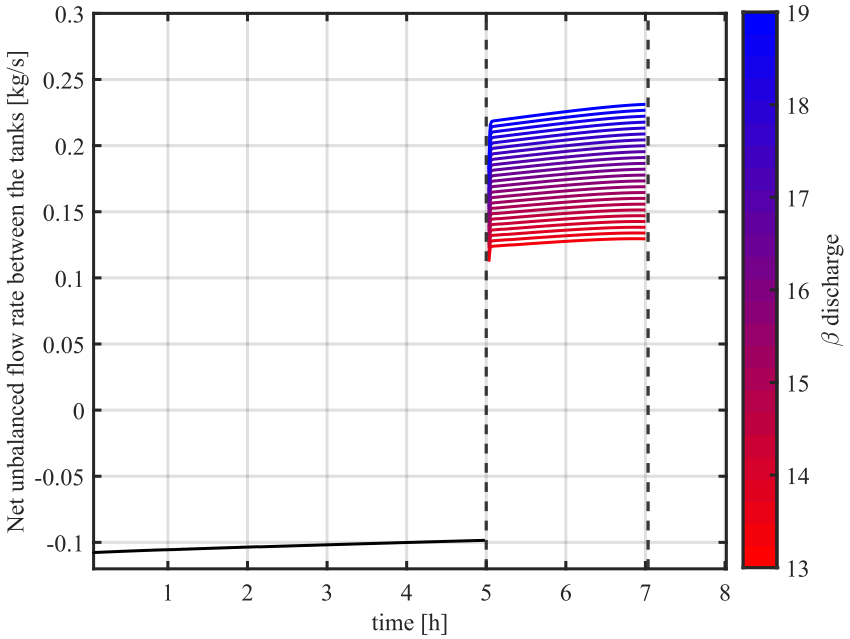

Fig. 3.46: Net flow rate unbalance between the two tanks: if negative the flow must be extracted from the system, if positive the opposite

Looking at the variation of mass inside the storages, during the first charge phase, the decrease of the hot tank's mass is predominant compared to the increase of the cold one as depicted in Fig. 3.47. The same relation but reversed is found during the discharge phase. According to 3.2.3, net flow rate imbalance between HR and CR must be extracted and delivered to the BV during the charge phase to avoid an increase of pressure, while the opposite during the discharge phase. The pressurization/depressurization phases cause a jump in the mass, depending on the pressure level selected. This mass is exchanged again with the BV.

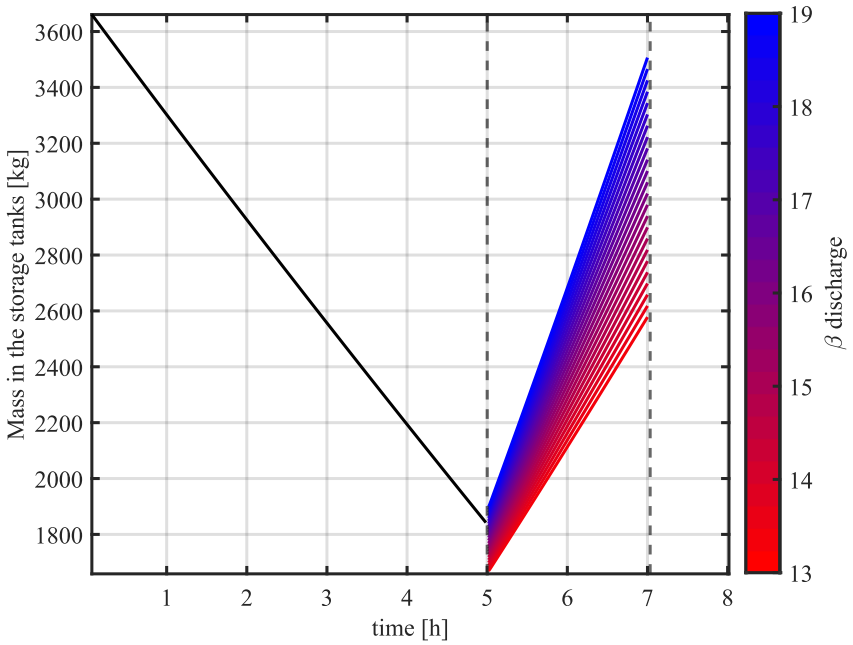

Fig. 3.47: Variation of total mass over during time

Since the BV, according to 3.3, is designed to withstand the difference of mass for the overall operating time, including the pressurization/depressurization transient, the maximum pressure of the tank must stay below the limiting pressure of the compressor feeding the tank itself, which is the discharge one. As the discharge pressure ratio increase the total volume of the BV decreases as a consequence of the higher maximum pressure achievable when it is fully filled with gas and the lower pressure difference between the two phases. At time=t_0, the initial mass inside the BV is the required one to achieve the minimum pressure. BV mass and pressure over time are shown in Fig. 3.48.

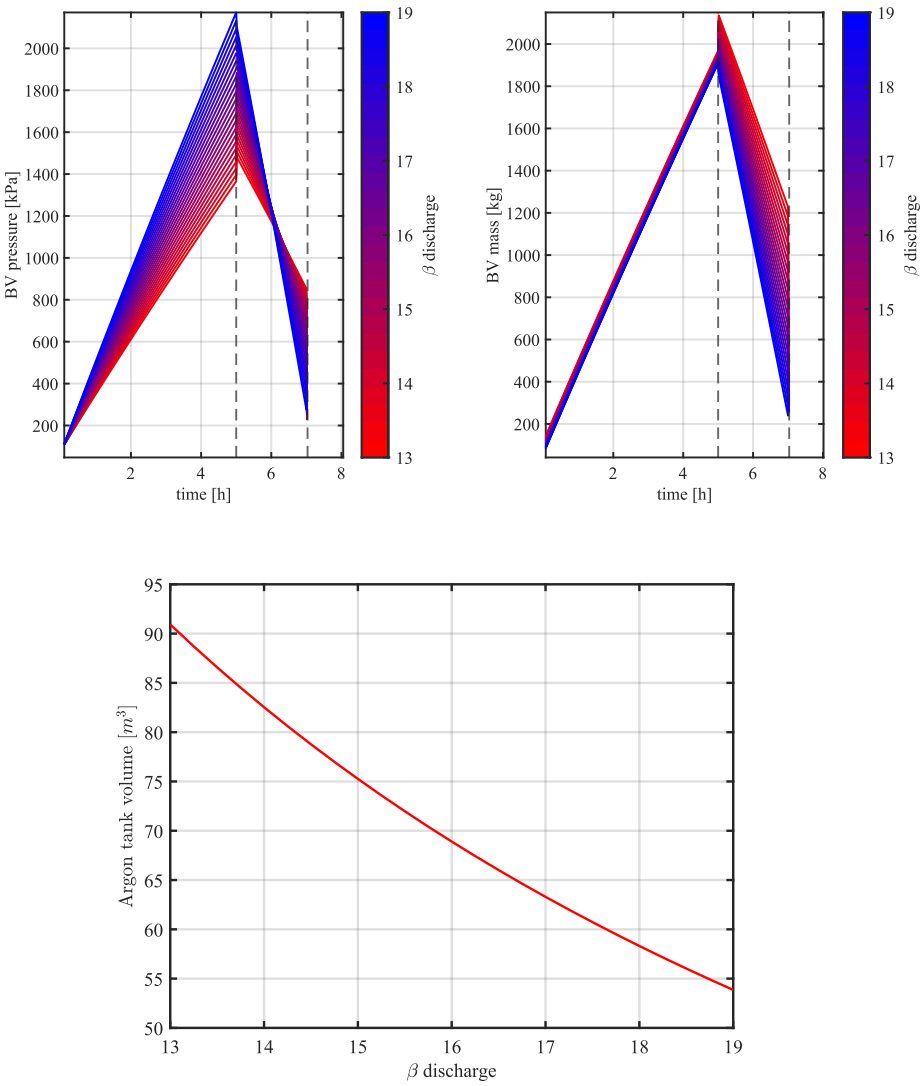

Fig. 3.48: BV mass, pressure, and volume variation

Final considerations must be done regarding the RTE. An optimum efficiency can be found at a pressure ratio of 15.75 during the discharge. The shaft power to be higher compared to a compression ratio of 20, because the variation amplitude of the compression power is greater than that of the expansion power when the discharging compression ratio increases from 15.75 to 20. The unbalanced flow rate and the variation of the pressure drops during time causes a reduction in power output during discharge, which causes a decrease in the RTE with respect to the one expected without considering the dynamic behaviour of the system. from 64.73% to 62.99%.

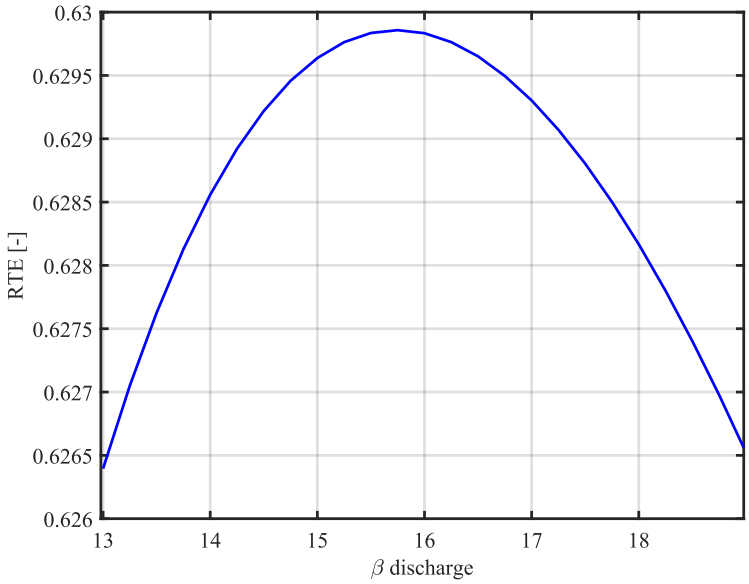

Fig. 3.49: Round-trip efficiency optimization results

Fig. 3.50 shows that the powers of the PTES compressor, expander and shaft are rather stable during the charging process, with a slight overall decrease in the shaft power absorption; during the delivery process, the compressor power and the expander power decrease gradually, thus leading to a decrease in shaft power, following the respective pressure ratios trends. Final rating parameters are summarized in Table 3.11 for the overall plant. Process flow diagrams for both phases are shown in Fig. 3.51, while Table 3.12 and Table 3.13 summarize the design parameters for the discharge turbomachinery. Since the flow rate processed is higher, the machines are bigger in terms of mean diameter compared to the charge machines and run slower (7500 vs 10500 rpm) to gain optimal specific speed and diameter in different operating conditions. The turbine efficiency is higher since the size parameter increases with the increase in dimension.

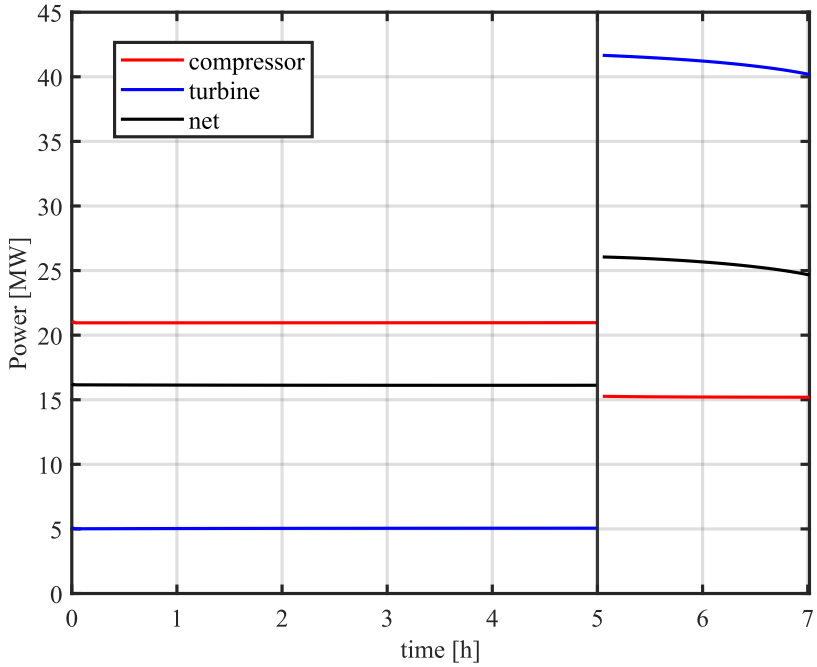

Fig. 3.50: Power levels over time

Table 3.11; Rating parameters of the plant

Parameter		
Average net power absorption during charge	16.13	MW
Average net power delivering during discharge	25.9	MW
Nominal charge time	5	h
Nominal discharge time	2	h
Total Storage volume	725	m^3
BV volume	72	m^3
RTE	62.99	%
Average power density	326.83	kJ/m^3
Energy density	69.36	kWh/ m^3

Table 3.12: Baseline design parameters for discharge compressor

Compressor parameter	Charge	
Inlet flow rate	125	kg/s
Inlet pressure	105	kPa
Inlet temperature	-171	°C
Nominal pressure ratio	15.75	-
Nominal speed	7500	rpm
Mean diameter	0.693	m
Number of stages	9	-
Efficiency islands	86/84/82[8]	%
Nominal power	15	MW

Table 3.13: Baseline design parameters for discharge turbine

Turbine parameter	**Discharge**	
Inlet flow rate	125	kg/s
Inlet pressure	1669	kPa
Inlet temperature	821	°C
Nominal expansion ratio	14.97	-
Nominal speed	7500	rpm
Mean diameter	0.45	m
Number of stages	3	-
Nominal efficiency	94.13	%
Nominal power	41.5	MW

For charge and discharge machines, the performance parameters (power, flow rate and turbine speed) are comparable with typical industrial gas turbines in the same power range. A comparison can be done with the Siemens Energy gas turbine portfolio [38]. SGT- 400 and SGT-600 can be compared respectively with the charge and discharge machines.

[8] Assumed for off-design condition

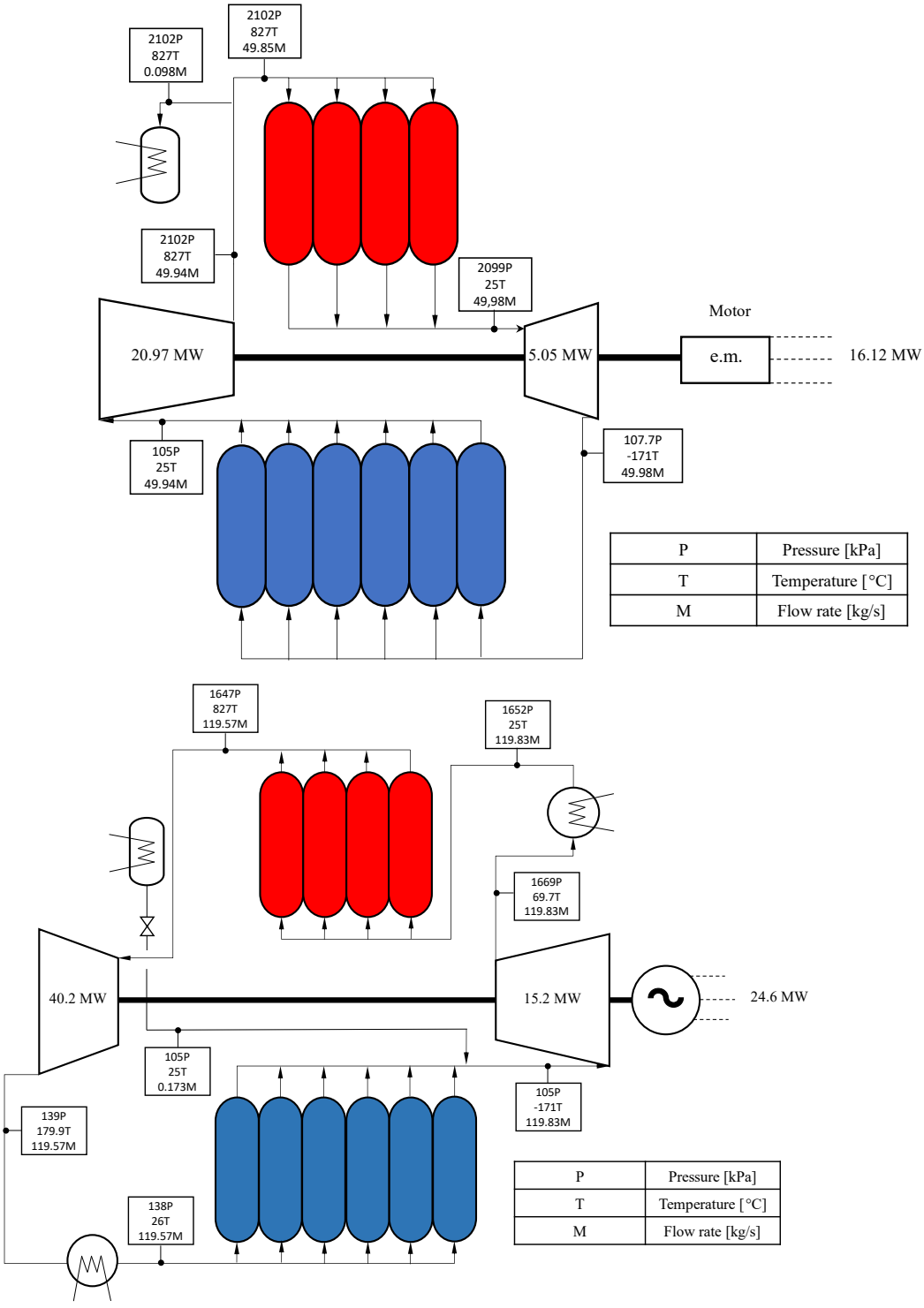

Fig. 3.51: Flow diagram for charge/discharge

4 Packed bed dynamic model

In this fourth chapter, the numerical model used to predict packed-bed energy storage performance is presented. First, the different models that can be adopted, depending on the conditions and hypothesis selected, are listed in a literature review. Then, the selected analytical and numerical models are presented and described, followed by some useful correlations enabling quantifying the main physical phenomena involved in the packed bed.

4.1 Literature review

Numerous numerical models for packed-bed energy storage have been presented in the literature as summarized by Ismail et al. [39] and then grouped and presented completely by Esence et al. in [40]. All of them are derived from energy equations applied to the components of the storage system, assuming no mass exchange and no heat production inside the storage. The heat exchange between the fluid and the solid is assumed proportional to the average difference in temperature (Newton's law). The physical properties of the materials may be considered constant and uniform or not depending on the authors. The additional assumptions and deriving simplifications (presented in Table 4.1) lead to various kinds of numerical models. First, the models may be grouped into two main categories depending on whether significant thermal gradient inside the solids is considered or not. In the present review, only the models with no thermal gradient inside the filler sphere will be presented. Then, differentiation can be made according to the number of dimensions (1D or 2D) and to the number of phases (fluid, solid, walls) accounted for.

4.1.1 Models with negligible thermal gradient within the solid

This approach is used when the conduction resistance in the solids of the packed bed is negligible compared to the convection resistance. This assumption is assessed thanks to the dimensionless Biot number, defined for packed solid-fluid heat transfer as [41]:

$$Bi = \frac{h}{k_s S_v} \leq 0.1 \tag{4.1}$$

Where S_v is defined as the particle surface-to-volume ratio:

$$S_v = \frac{4\pi {r_p}^2}{\frac{4}{3}\pi {r_p}^3} = \frac{6}{d_p} \tag{4.2}$$

The Schumann model

The Schumann's model is a reference for many authors. This one-dimensional two-phase model of heat transfer in porous media was originally developed by Schumann, 1929 [42]. It consists in two energy equations, one for the fluid and the other for the solid, linked by a convective heat exchange term. According to Fig. 4.1, the straightforward energy balance between gas and solid gives:

$$\dot{m}_g c_{p,g} \frac{\partial T_g}{\partial z} + A\varepsilon\rho_g c_{p,g} \frac{\partial T_g}{\partial t} = hA(1-\varepsilon)S_v\left(T_s - T_g\right) \tag{4.3}$$

$$\rho_s A(1-\varepsilon)c_s \frac{\partial T_s}{\partial t} = hA(1-\varepsilon)S_v\left(T_s - T_g\right) \tag{4.4}$$

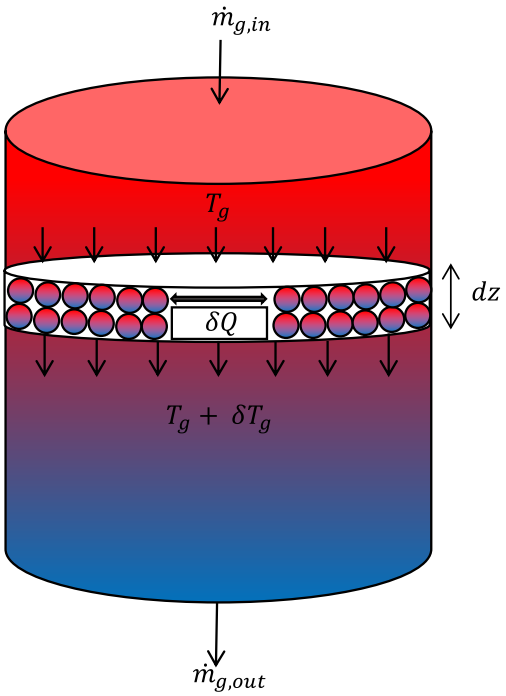

Fig. 4.1: Schumann model heat transfer schematic

The Schumann model is valid under conditions presented in Table 5. An analytical solution of this model was proposed by Schumann himself. This analytical solution is valid when the volumetric heat capacity of the fluid is negligible compared to one of the solids (i.e. for gas/solid systems); the solids are initially at a zero uniform temperature and the material properties, the inlet fluid temperature and the fluid flow rate are assumed constant.

One-dimensional single-phase models: simplification of the Schumann model

Single-phase models, directly derived from the Schumann model, were mainly introduced by the work of Vortmeyer et al. [43] and consist in modelling the packed bed with a single equation. Two kinds of single-phase models involving different assumptions and simplifications depending on whether the fluid is liquid or gaseous may be considered. With gaseous HTF, it is reasonable to assume that the internal energy of the fluid is negligible compared to the one of the solids ($\rho_g \cdot c_{pg} \ll \rho_s \cdot c_{ps}$). Therefore, a Schumann-type model with additional diffusion terms (with uniform effective thermal conductivities) but without the internal energy term of the fluid may be considered. Based on this, a single-phase one-dimensional model may be obtained by only

assuming that the second derivatives in space of the fluid and the solid temperatures are equal ($\partial^2T_s/\partial^2z = \partial^2T_g/\partial^2z$), which can be reasonably assumed in most packed bed storage systems:

$$(1-\varepsilon)\rho_s c_s \frac{\partial T_s}{\partial t} + \varepsilon\rho_g c_{p,g} u \frac{\partial T_s}{\partial z} = \left[k_{eff,s} + k_{eff,g} + \frac{(\varepsilon\rho_g c_{p,g} u)^2}{hS_v}\right]\frac{\partial^2 T_s}{\partial^2 z} \qquad (4.5)$$

It should be noticed that thermal destratification due to non-infinite HTC is included in the diffusion term of single-phase model. As a consequence, the additional simplifications of these models enable to reduce computational effort but don't enable to dispense with the determination of the HTC.

One-dimensional three-phase model

In order to account more finely for the influence of the walls, a dedicated energy equation may be added, as done by Hoffman [44]. The model takes into account heat capacity and axial conduction in the tank's walls. If this equation is added to the general two-phase one-dimensional model presented, the new one-dimensional three-phase model becomes:

$$(1-\varepsilon)\rho_s c_s \frac{\partial T_s}{\partial t} = h\frac{A_{s,tot}}{V_{tot}}\left(T_s - T_g\right) \qquad (4.6)$$

$$\varepsilon\rho_g c_{p,g}\left(\frac{\partial T_g}{\partial z} + u\frac{\partial T_s}{\partial z}\right) = h\frac{A_{s,tot}}{V_{tot}}\left(T_s - T_g\right) + h_{w,int}\frac{A_{w,tot}}{V_{tot}}\left(T_w - T_g\right) \qquad (4.7)$$

$$\rho_w c_{s,w}\frac{\partial T_w}{\partial t} = h_{w,int}\frac{A_{w,int}}{V_{w,tot}}\left(T_g - T_w\right) + h_{w,ext}\frac{A_{w,ext}}{V_{w,tot}}\left(T_\infty - T_w\right) \qquad (4.8)$$

Internal and external wall heat transfer coefficients are associated with shape factors calculated, respectively, with the internal and external surface area of the walls ($A_{w,int}$ and $A_{w,ext}$). Hypothesis and conditions for the different reported models are schematized in Table 4.1.

Table 4.1: Assumptions and simplifications for each model

Hypothesis	Schumann	1D single-phase (gaseous)	1D three-phase
Negligible thermal gradient inside the solid (Bi<0.1)	✓	✓	✓
Homogeneous porous medium	✓	✓	✓
1D system with fluid circulating according to plug-flow	✓	✓	✓
Adiabatic storage	✓	✓	✗
Negligible diffusion compared to convection	✓	✓	✓
Fluid and solid temperature second derivatives in space close to each other	✗	✓	✗
Fluid and solid temperatures close to each other	✗	✓	✗
Uniform HTC around solid	✓	✓	✗

4.2 White semi-analytical method

The Schumann model has been chosen for the modelling of the heat transfer, as a simplified but accurate method for gaseous fluid. Accurate simulations require numerical integration of these equations together with the mass continuity and momentum equations in order to account for gas density and other property variations. Neglecting the unsteady pressure term, Schumann equations may then be expressed in the normalised form according to [45]:

$$\frac{\partial \vartheta_g}{\partial \xi} = \vartheta_s - \vartheta_g \tag{4.9}$$

$$\frac{\partial \vartheta_S}{\partial \eta} = \vartheta_g - \vartheta_s \tag{4.10}$$

Where $\vartheta_{g,s} = \left(T_{g,s} - T_{in,s}\right)/\left(T_{in,gas} - T_{in,s}\right)$ and ξ and Φ are the dimensionless length and time variables given by:

$$\xi = \frac{z}{l} \tag{4.11}$$

$$\Phi = \frac{t}{\tau} \tag{4.12}$$

The length and time scales used for this normalisation are, respectively:

$$l = \frac{\dot{m}\, c_{p,g}}{hA(1-\varepsilon)S_v} \tag{4.13}$$

$$\tau = \frac{\rho_s c_s}{hS_v} \tag{4.14}$$

Time and length scales are evaluated taking into account the variation of solid and gas properties with temperature. The dimensionless space and time are computed for each time step. Note that the dependence of Φ on z is neglected since stems from the unsteady accumulation of internal energy within the gas and can be ignored due the low heat capacity of the gas per unit of volume compared with that of the solid.

Fluid-solid intra-particle heat transfer coefficient

The fluid/solid HTC is a key parameter that governs the charge and discharge power and the thermal stratification of the storage. This parameter is expressed in the classical surface form (*h*

in W/m^{2}K). Regarding the determination method, the correlation of Wakao et al. [46] was developed on a large range of experimental data from different setups, is easy to implement, widely used in the literature and in the average of the other correlations. It seems to be a relevant choice to calculate the HTC in packed beds, at least in a first approach. The correlation proposed is the following:

$$Nu = 2 + 1.1\, Pr^{0.33}\, {Re_p}^{0.6}$$

$$Re_p = \frac{\rho_g u_s}{d_p}\ ,\ P_r = \frac{\mu_g c_{p,g}}{k_g} \qquad (4.15)$$

Its range of validity is for Re_p between 15 and 8500, in laminar regime. The correlation is evaluated considering a D-C (Dispersion Concentric model), and can be used coupled with Schumann model with a relative error lower than 0.5% [46]. The differences between the two models are depicted in Fig. 4.2.

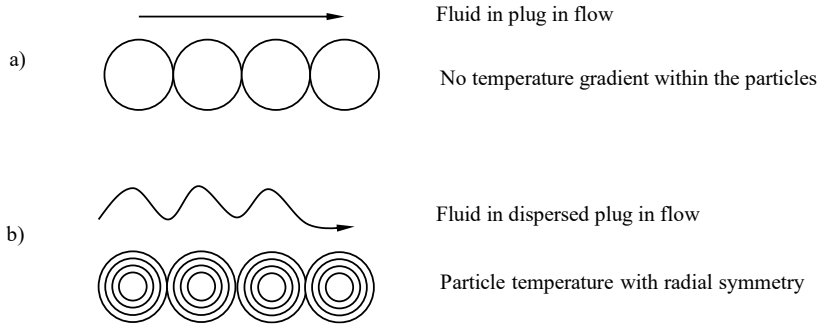

Fig. 4.2: a) Schumann model schematic b) D-C model schematic

The heat transfer coefficient can be calculated as follows:

$$h = \frac{Nu\, k_g}{d_p} \qquad (4.16)$$

Numerical method

The numerical method used to integrate is similar to that presented in [45] but stability and computational efficiency have been improved by employing a semi-analytical approach developed by White [47], with some modifications to decrease computational time. The Schumann equations describe the dependence of gas and solid temperature evolution with space and time variation inside the storage bed. To build a solid numerical routine, a space and time grid is necessary to integrate the governing equations (4.9) and (4.10). The computational grid is shown in Fig. 4.3.

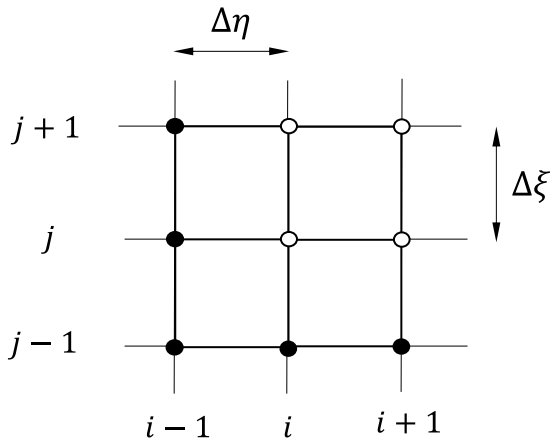

Fig. 4.3: Computational grid; i represents the time step and j the spatial step. Temperatures are known at nodes marked with ● and unknowns at nodes market with ○

Starting from Eq. 4.10, the task is thus to obtain values of temperatures in the unknowns nodes. This is achieved by integrating Eq. 4.10 between nodes $(j-1\,,\ i)$ and $(j\,,\ i)$ whilst holding Ts constant at their average values:

$$\int_{\vartheta_{g,j-1}^{i}}^{\vartheta_{g,j}^{i}} \frac{\partial \vartheta_g}{\bar{\vartheta}_s - \vartheta_g} = \int_{\xi_{j-1}}^{\xi_j} \partial\xi \qquad (4.17)$$

$$ln\left(\frac{\bar{\vartheta}_s - \vartheta_{g,j}^{i}}{\bar{\vartheta}_s - \vartheta_{g,j-1}^{i}}\right) = -\Delta\xi \qquad (4.18)$$

$$\vartheta_{g,j}^{i} = \bar{\vartheta}_s \left(1 - e^{-\Delta\xi}\right) + \vartheta_{g,j-1}^{i} e^{-\Delta\xi} \tag{4.19}$$

The same procedure can be applied to Eq. (4.11) to evaluate the solid temperature:

$$\vartheta_{s,j}^{i} = \bar{\vartheta}_g \left(1 - e^{-\Delta\Phi}\right) + \vartheta_{g,j}^{i-1} e^{-\Delta\Phi} \tag{4.20}$$

With the average temperatures of solid and gas respectively:

$$\bar{\vartheta}_g = \frac{\vartheta_{g,j}^{i} + \vartheta_{g,j}^{i-1}}{2} \tag{4.21}$$

$$\bar{\vartheta}_s = \frac{\vartheta_{s,j}^{i} + \vartheta_{s,j-1}^{i}}{2} \tag{4.22}$$

The resulting pair of equations may be expressed in the form of a linear system. By inverting a 2x2 matrix is possible to evaluate the solid and gas temperature at node $(j\,, i)$.

$$\begin{pmatrix} 1 & 0.5\left(e^{-\Delta\xi} - 1\right) \\ 0.5\left(e^{-\Delta\Phi} - 1\right) & 1 \end{pmatrix} \begin{pmatrix} \vartheta_{g,j}^{i} \\ \vartheta_{s,j}^{i} \end{pmatrix} = \begin{pmatrix} 0.5\left(1 - e^{-\Delta\xi}\right)\vartheta_{s,j-1}^{i} + e^{-\Delta\xi}\vartheta_{g,j-1}^{i} \\ 0.5\left(1 - e^{-\Delta\Phi}\right)\vartheta_{g,j}^{i-1} + e^{-\Delta\Phi}\vartheta_{s,j}^{i-1} \end{pmatrix} \tag{4.23}$$

The advantage of this approach is that the 'stiffness' is integrated out of the equations enabling much larger time steps to be taken than with a straightforward finite difference discretisation. Generally, solutions are 'grid' independent for space and time steps less than 20% of l and τ respectively. For the specific case studied in this thesis in terms of geometry and flow, for grid size higher than 4000, temperature profiles for charge and discharge can be considered independent from this parameter. Finally, the mass flow varies very slightly through the reservoir due to the change in the mass of stored gas brought by the passage of the thermal front. Eq. (4.24) is thus implemented in the form:

$$\dot{m}_{g,j}^{i} = \dot{m}_{g,j-1}^{i} + \varepsilon A \frac{\Delta z}{\Delta t}\left(\rho_{g,j}^{i-1} - \rho_{g,j}^{i}\right) \tag{4.24}$$

The initial conditions for the single charge cycle are:

$$T_g(t=0) = T_s(t=0) = T_{inital,bed}$$
$$T_g(z=0) = T_s(z=0) = T_{in,gas} \quad (4.25)$$

The initial conditions for the discharge cycle are:

$$T_g(t=0) = T_g(t_{end})$$
$$T_s(t=0) = T_s(t_{end}) \quad (4.26)$$
$$T_g(z=L_{bed}) = T_s(z=L_{bed}) = T_{in,gas}$$

The boundary conditions are:

$$\frac{\partial T_g(z=h_{bed})}{\partial z} = 0$$
$$\frac{\partial T_s(z=0)}{\partial z} = \frac{\partial T_s(z=L_{bed})}{\partial z} = 0 \quad (4.27)$$

4.3 Results and discussion

Input design parameters for the two storages are presented in Table 4.2 and are the same used previously for the calculation with the ideal thermal front model. The real heat transfer phenomena and the consequent temperatures profile for HR and CR are depicted in Fig. 4.4 and Fig. 4.6. The packing is assumed to be composed of uniformly sized, spherical pebbles, which are characterised by an average equivalent diameter d_p. The presence of the wall leads to variations in the packing structure, but this effect is neglected for simplicity. Consequently, the void fraction is considered around 0.4 in the entire bed. It has been suggested that radial non-uniformities can be neglected for values of $D/d_p > 40$. In this study, D/d_p is in the order of 800 (D=4 m and d_p=0.005 m) [45].

Table 4.2: Design input data for the two reservoirs

Packed bed	Hot reservoir	Cold reservoir	
Filler	Basalt	Basalt	-
ρ_s	3011	3011	kg/m^3
d_p	5	5	mm
c_s	c_s (T_s)	c_s (T_s)	J/kgK
k_s	1.5	1.5	W/mK
D	4	4	m
N° vessels	4	6	-
Bed height	5.1	6.3	m
Total volume	250	475	m^3
ε	0.4	0.4	-
ψ	1	1	-
Initial temperature	25	25	°C
Charge flow rate	50	50	kg/s
Discharge flow rate	125	125	kg/s
Time and space grid points	4000	4000	-
T_{max}	820	25	°C
T_{min}	25	-171	°C
Inlet pressure for charge and discharge	2000	107	kPa

As already explained before, the mass flow rate of working fluid increases from inlet to outlet in the hot storage and decreases in the cold one during the charge period (since hot storage experiences a decrease in the mass and the cold an accumulation), while the opposite trend are found during dicharge. The thermal front speed V_n (which can be found from an energy balance) is also a function of the axial coordinate:

$$V_n = \frac{\dot{m}\, c_{p,g}}{N_{Tank} A (1 - \varepsilon) \rho_s c_s} \qquad (4.28)$$

4.3.1 Hot reservoir

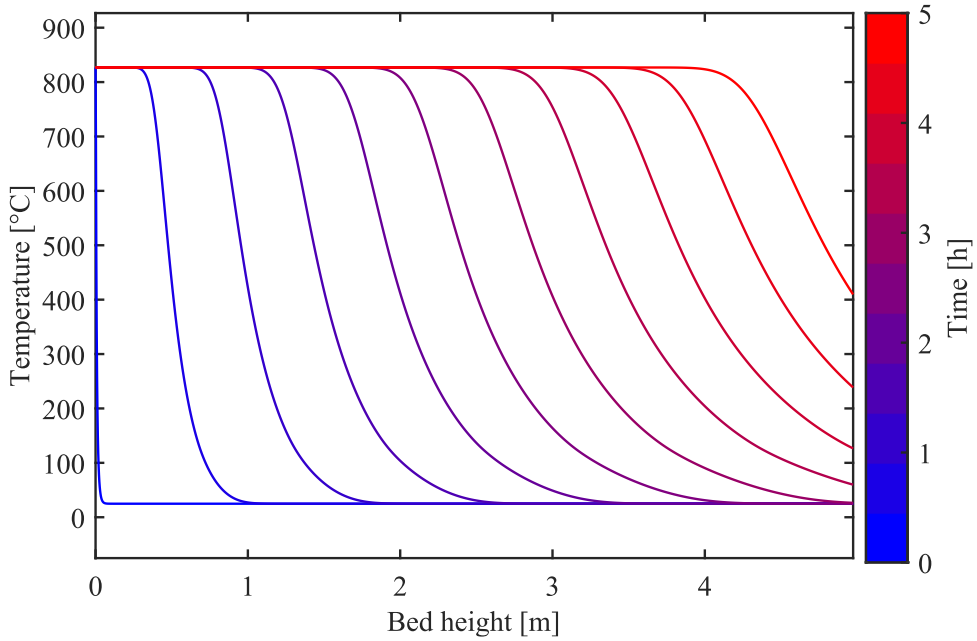

Fig. 4.4: Gas thermal front spreading in HR during a full-charge period with nominal tank volume and d_p=5mm,

For the HR, during charge, the velocity of the thermal front decreases as time proceeds, leading to a change in the front length as shown in Fig. 4.4. The wave speed depends on the solid specific heat capacity which increases with temperature and on the flow rate, which increases layer by layer. The overall effect is dominated by the specific heat capacity, which leads to a spreading of the front, overcoming the steepening caused by the increase in flow rate along with the axial position. The spreading is significant in the HR due to the huge difference in maximum and minimum temperature inside the reservoir itself (ΔT_{hot}=795°C) with the consequent huge increase of specific heat capacity of the solid (from 0.61 kJ/kgK to 1.2 kJ/kgK). The difference between solid and gas temperature is about 5°C due to the heat transfer characteristics of the stratified thermocline and the small particle diameter as illustrated in Fig. 4.5.

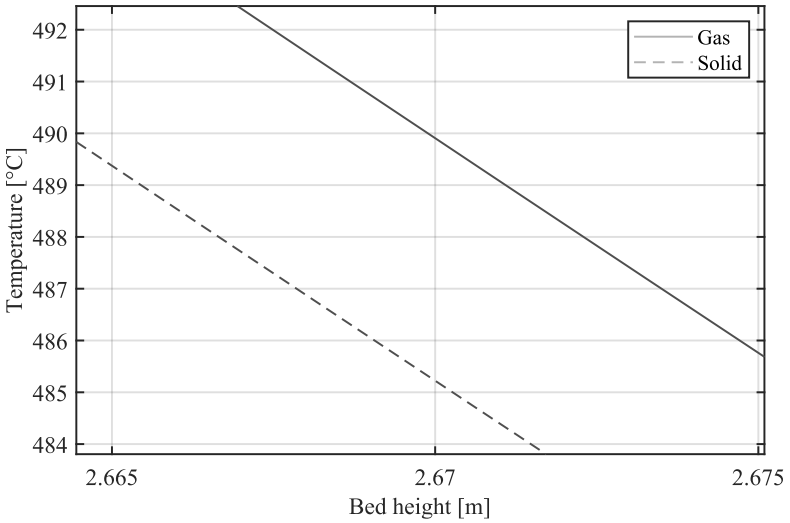

Fig. 4.5: Temperature profiles difference (t=9000s)

After 3.5h the front comes out from the bed and increases the outlet gas temperature.

4.3.2 Cold reservoir

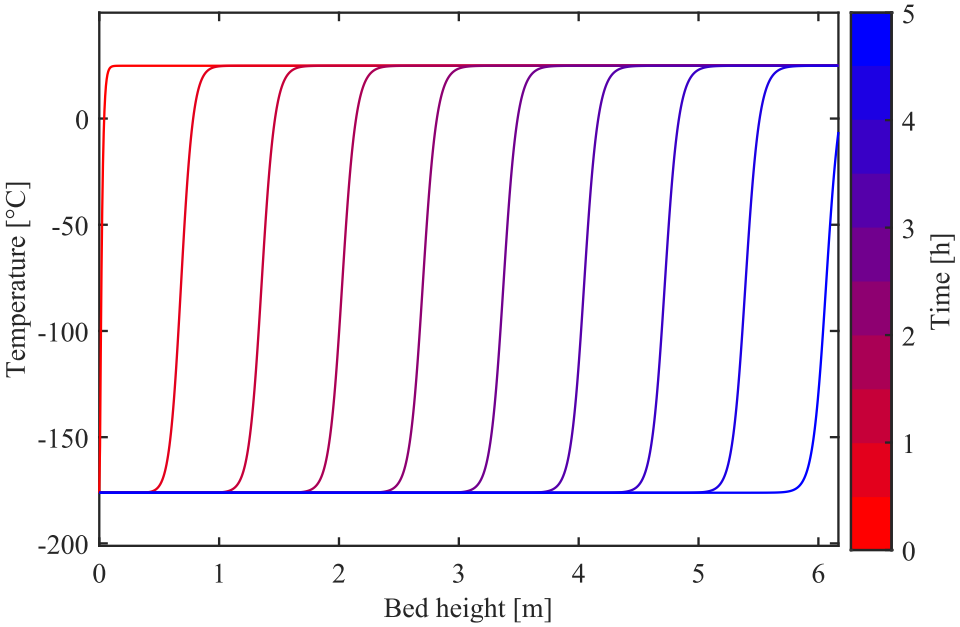

Fig. 4.6: Gas thermal front spreading in CR during a full-charge period with nominal tank volume and d_p=5mm,

For the CR instead, during the charge, the velocity of the thermal front increases as time proceeds, since the flow rate decreases layer by layer but the effect of the decrease in the specific heat capacity with temperature is predominant, steepening the temperature profile. The difference between solid and gas temperature is around 5°C as shown in Fig. 4.7. The thermal front results compared to the one in HR due to the lower specific heat capacity of the solid and the smaller difference in maximum and minimum temperature inside the reservoir itself (ΔT_{cold}=201°C), with the consequent small increase of specific heat capacity in this temperature range (from 0.42 kJ/kgK to 0.61 kJ/kgK).

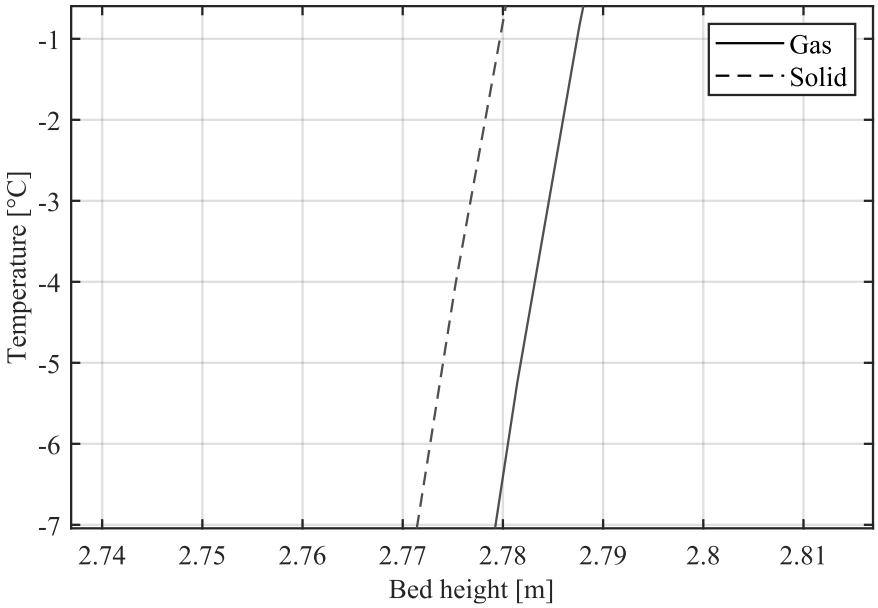

Fig. 4.7: Solid/Gas temperature profiles difference (t=4500s)

After 5h of operation, the front remains nearly inside the bed and the outlet gas temperature remains almost constant for the entire charge period due to the characteristics of the reservoir.

4.4 Model validation

A wide body of publications describes numerical models for sensible heat storage in packed beds, but only a few include experimental validation. Noteworthy among these are Coutier et al.[48] and Beasley et al. [49]. The present sub-section presents a validation of the heat transfer model using previously published experimental results by this group [33], on an air-based packed bed of rocks, as done also by Hänchen et al.[50] to validate their numerical method (see Fig. 4.9). Measurements were made on a pilot tank built out of a vertically oriented packed bed of crushed

steatite (magnesium silicate rock). Operational parameters are listed in. Table 4.3. Since D/d=7.4, the plug flow assumption introduces inaccuracies because of wall effects, as higher velocities are developed in the low porosity areas next to the boundaries. This effect is only relevant for narrow tanks and can usually be neglected for D/d>40. A bypass flow close to the wall has been introduced to account for this effect. As an approximation, it is assumed that the bypass flow passes the column without thermally interacting with the packed bed, thus the flow passing through the packed bed is reduced by a given amount. The numerically modelled and experimentally measured gas temperature profiles across the pilot storage tank are shown in Fig. 4.8, after 1200, 3000, and 4800 seconds. Good agreement was achieved with a bypass flow rate equivalent to 15% of the total mass flow rate. The choice of h has a strong influence on the profile shape. The correlation by Coutier et al. [48] shows the heat transfer coefficient between the air and the packed bed as a function of the air mass flow rate per unit cross section, $G = \frac{\dot{m}}{A}$, and particle diameter d. The choice of the selected correlation [3] provided a better match than others considered.

$$h = \frac{700}{6(1-\varepsilon)} G^{0.76} d_p^{0.24} \qquad (4.29)$$

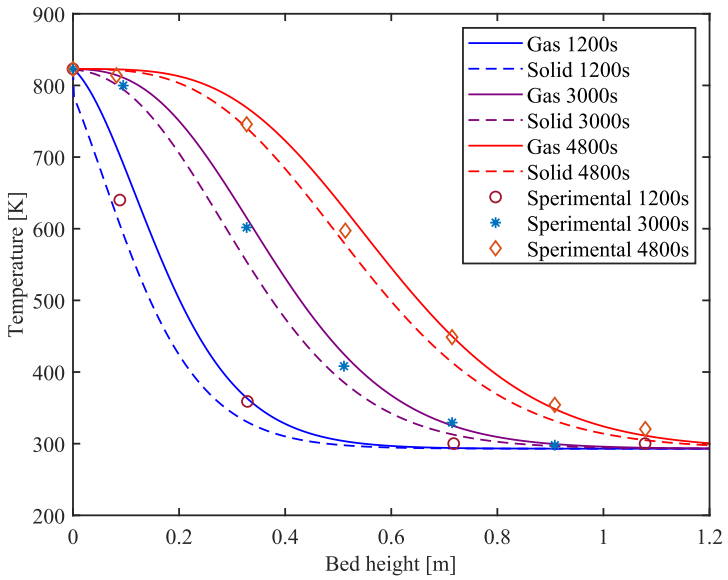

Fig. 4.8: Numerically modelled and experimentally measured temperature profiles across the pilot storage tank [33]*, after 1200, 3000 and 4800 s.*

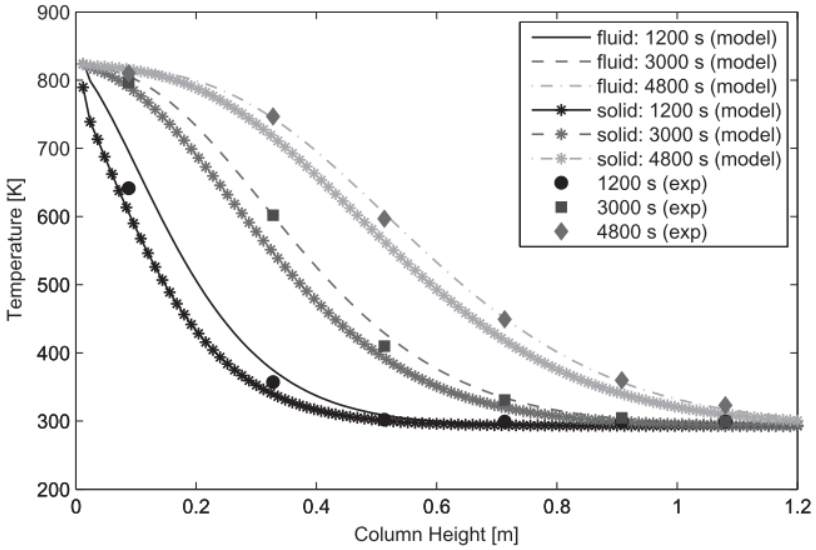

Fig. 4.9: Hänchen [50] *numerically modelled and experimentally measured temperature profiles across the pilot storage tank* [33]*, after 1200, 3000 and 4800 s.*

Table 4.3: Operational parameters of the experimental setup

Parameter	**Value**	
$T_{in,g}$	823	K
$T_{in,s}$	293	K
Fluid	Air	-
G	0.225	kg/m^2s
H_{bed}	1.2	m
D	0.148	m
ε	0.4	-
ρ_s	2680	kg/m^3
d_p	0.02	m
c_s	1068	J/kgK
k_s	2.5	W/mK
% of by-pass flow	15	%

4.5 Parametric study

The following sub-section will evaluate the influence of different operating parameters on the thermal performance of the packed bed, including the fluid flow rate, length to diameter ratio of the packed bed and the particle diameter. The performance of the packed bed during charge and discharge can be expressed by the thermal efficiency. The overall energy balance between charge and discharge gives:

$$\begin{cases} E_{input,charge} = E_{stored} + E_{loss,exit,charge} + E_{loss,wall}{}^{9} \\ E_{stored} = E_{outflow,charge} + E_{loss,wall} \end{cases} \quad (4.30)$$

The energy balance is referred to the control volume containing only the storage tank, as shown in Fig. 4.10:

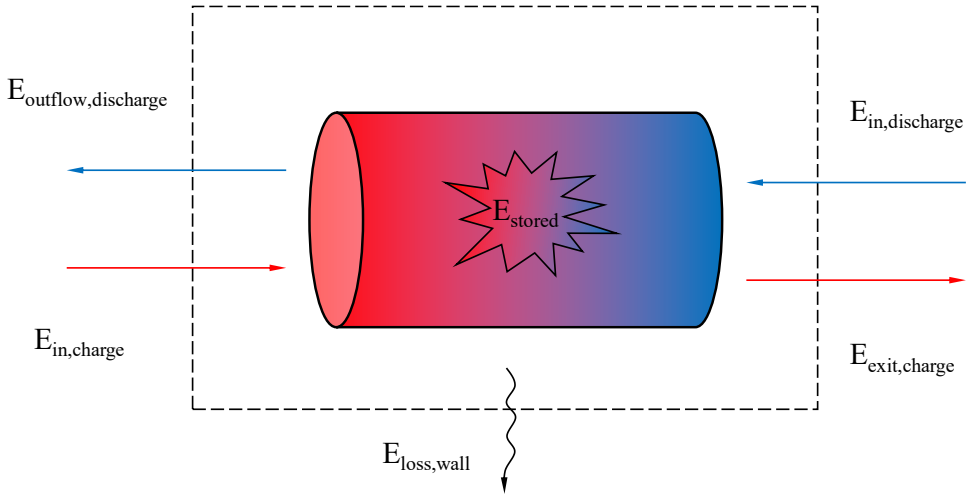

Fig. 4.10: Energy balance for the packed bed

For the input and output flows, the energy is thus:

$$E_{input/outflow} = \int_{0}^{t_{end}} \int_{T_0}^{T_{in/out(t)}} \dot{m}_g \, c_{p,g} dT dt \quad (4.31)$$

[9] For the purpose of this thesis, the wall is considered perfectly insulated

For the stored energy, the integration is over the length of the storage tank:

$$E_{stored} = \int_0^{L_{bed}} \rho_s c_s A(1-\varepsilon)(T_s(z) - T_0)dz \qquad (4.32)$$

The exit loss is defined as:

$$E_{exit} = \int_0^{t_{end}} \int_{T_0}^{T_{out,ch(t)}} \dot{m}_g \, c_{p,g} dT dt \qquad (4.33)$$

considering the Schumann model hypothesis, the wall losses are neglected. The charging efficiency is defined as:

$$\eta_{th,charge} = \frac{E_{stored}}{E_{input}} \qquad (4.34)$$

and describes the fraction of the input and pumping energy required to charge the storage tank. A low value of η_{charge} indicates an ineffective heat transfer or energy lost by hot fluid leaving the tank, i.e., a tank charged with energy that can no longer be stored. The discharging efficiency is defined as:

$$\eta_{th,discharge} = \frac{E_{outflow}}{E_{stored}} \qquad (4.35)$$

and describes the ratio of the energy extracted from the storage tank relative to the energy stored and the pumping energy required for extraction. The overall efficiency is defined as:

$$\eta_{th,overall} = \frac{E_{outflow}}{E_{input}} \qquad (4.36)$$

4.5.1 Fluid flow rate

Higher flow rates lead to significantly higher/lower (depending on the storage) temperatures at the bed exit considering the same discharge time of 2h, with the overall tank length almost reaching the inlet temperature of the gas. The nominal speed of the thermal front increases with the flow rate, decreasing the nominal time to discharge the CR and the HR with fixed volumes. The flow rate of HTF has a significant influence on the heat transfer coefficient as well as the pumping work required to cross the storage. Higher flow rates lead to better heat transfer between the two phases, but higher pressure drop inside the vessel.

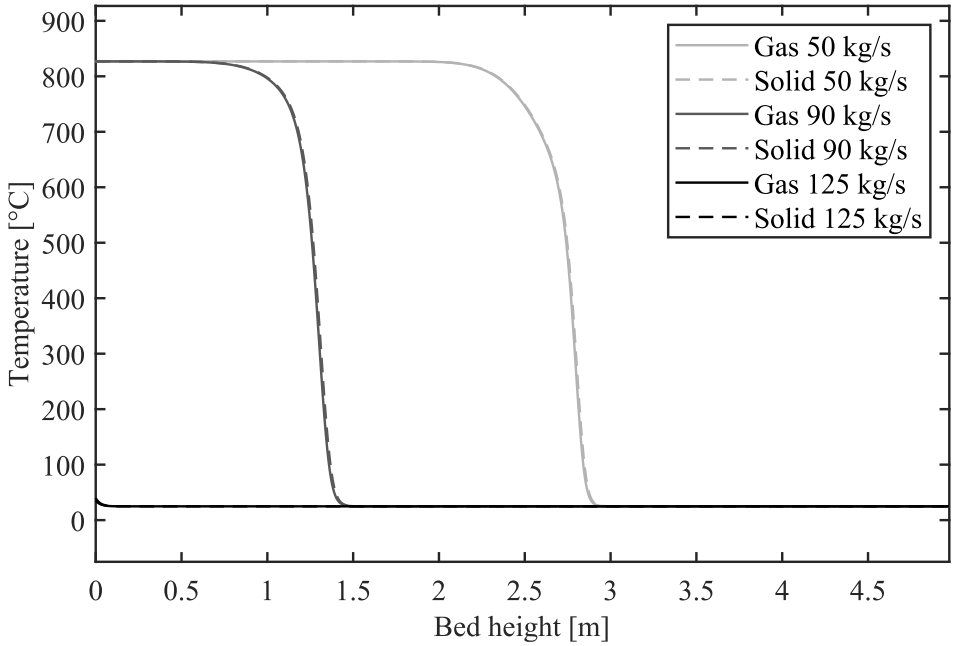

Fig. 4.11: HR temperature profiles at the end of 2h discharge cycle, dp=5mm

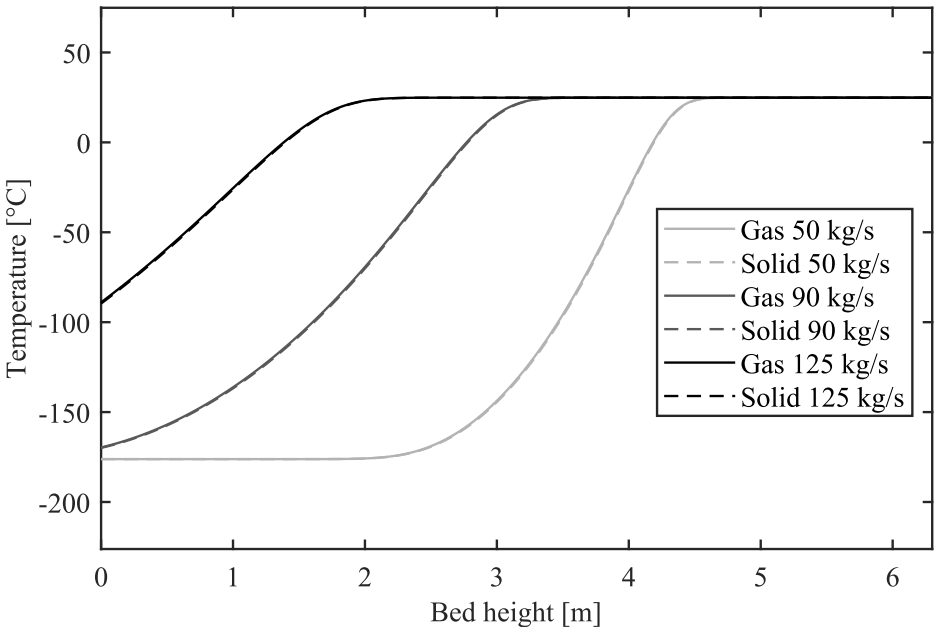

Fig. 4.12: CR temperature profiles at the end of 2h discharge cycle, dp=5mm

Considering the same discharge time, a higher flow rate will increase the overall thermal efficiency since the delivery flow will extract energy from almost the entire length of the bed as shown in Fig. 4.13 and Fig. 4.14. The overall efficiency will tend to be a number lower than one due to the non-ideal heat transfer between the two phases, leading to an exit loss during the charge period. Concerning the HR, the charge efficiency is lower due to higher exit losses with respect to the CR, but the spreading of the thermal front in the CR during the discharge decreases the delivery efficiency and the overall one of the latter. The increase in the thermal efficiency will be paid in terms of pressure drops.

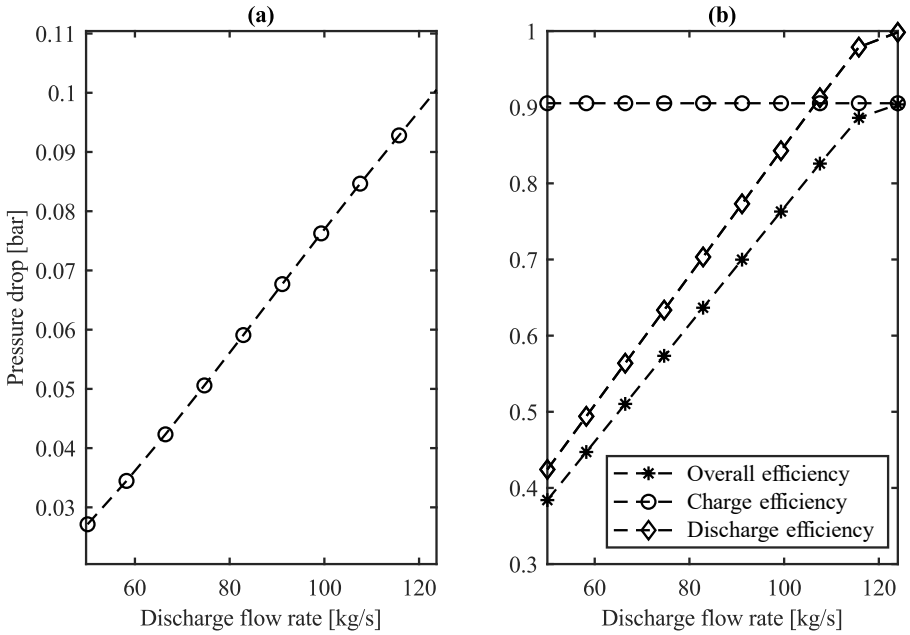

Fig. 4.13: a) HR average pressure drop during discharge vs. Discharge flow rate b) Thermal efficiencies vs Discharge flow rate; dp=5mm and t_{disch}=2h

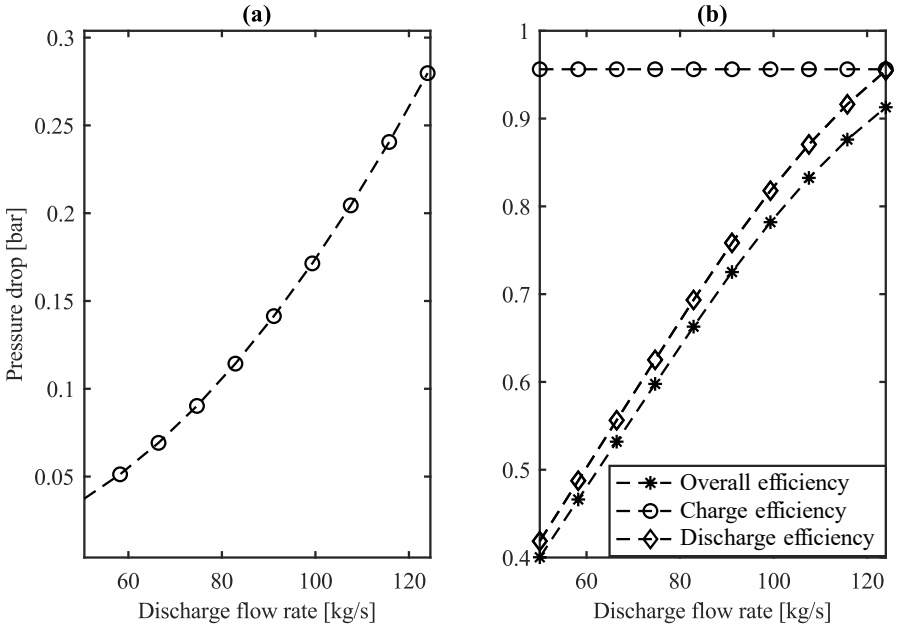

Fig. 4.14: a) CR average pressure drop during discharge vs. Discharge flow rate b) Thermal efficiencies vs Discharge flow rate; dp=5mm and t_{disch}=2h

Hot Reservoir

Regarding the HR, the temperature profiles during discharge are shown in Fig. 4.15. With the increase of flow rate from 50 kg/s for the charge period to 125 kg/s during the delivery, the heat transfer coefficient will grow, but the flow rate will decrease layer by layer as well as the specific heat of the filler material since the tank cools down. The overall effect is a steepening of the temperature profile minute by minute caused by the increase in the front speed. When the thermocline exits the bed, the temperature of the turbine (discharge mode) will decrease.

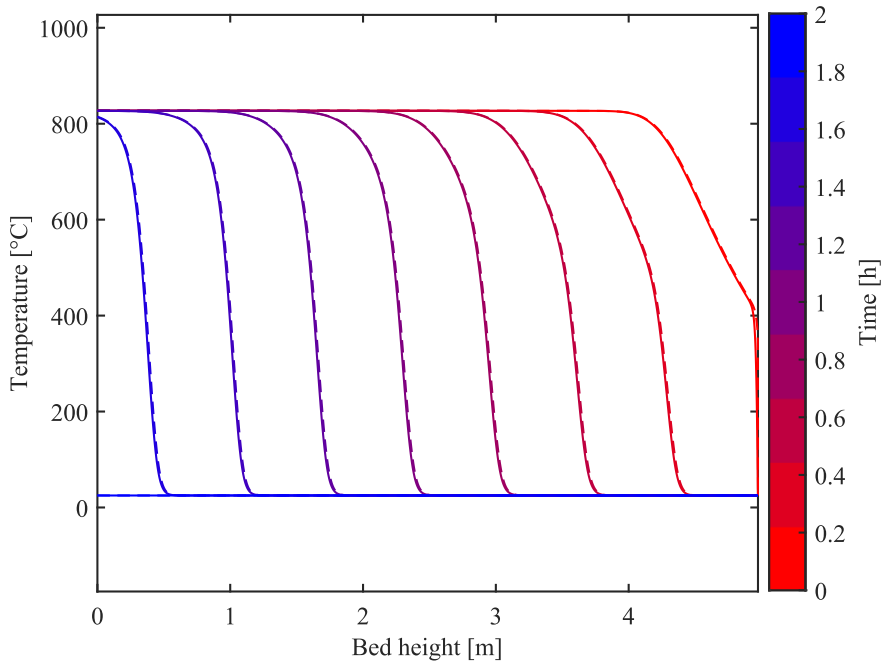

Fig. 4.15: Thermal front steepening in HR during a full-discharge period with nominal tank volume and d_p=5mm, —— Gas temperature – – – Solid temperature

Cold reservoir

For the CR, the temperature profiles during charge are shown in Fig. 4.16. The overall effect is a spreading of the temperature profile minute by minute caused by the heating of the tank and the increase in flow rate. When the thermocline exits the bed, the temperature of the compressor (discharge mode) will increase.

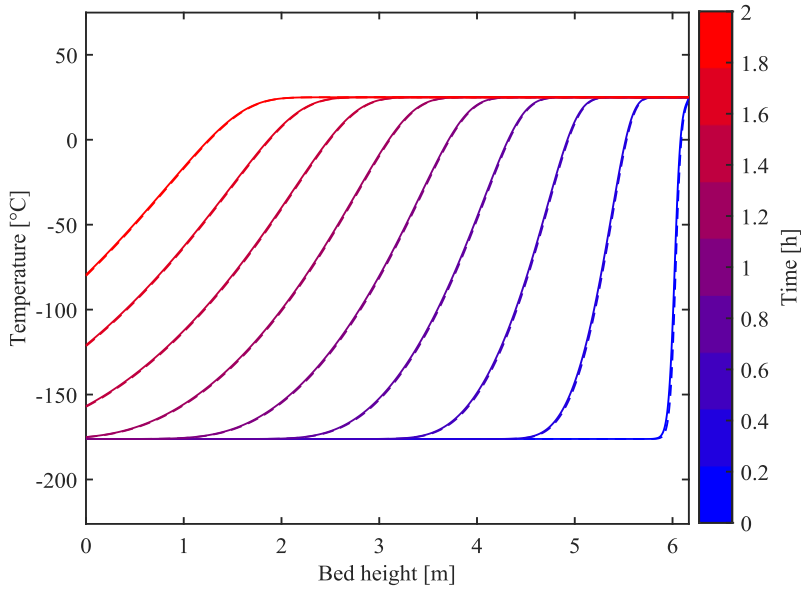

Fig. 4.16: Thermal front spreading in HR during a full-discharge period with nominal tank volume and d_p=5mm, —— Gas temperature – – – Solid temperature

4.5.2 Particle diameter

Fig. 4.17 and Fig. 4.18 show the temperature distributions of the solid and fluid phases across the storage height at half of the charge cycle with different particle sizes varied in the range between 5÷20 mm during charge and discharge.

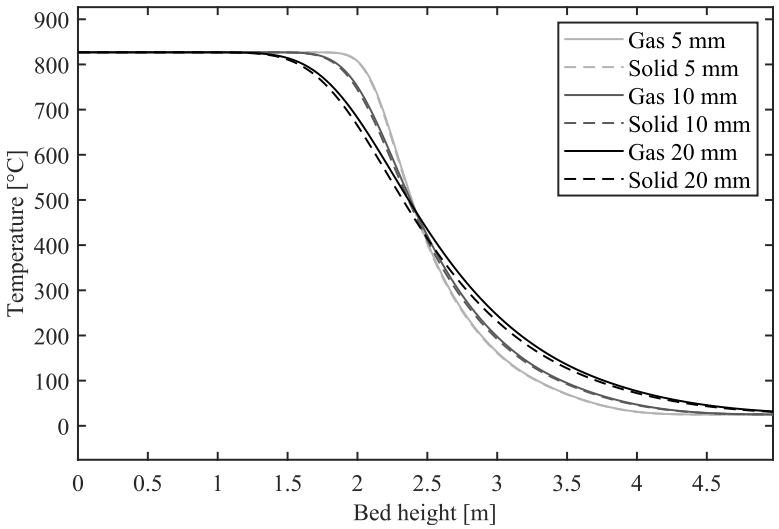

Fig. 4.17: Temperature distributions (HR) for varying particle diameter t=2.5h (charge)

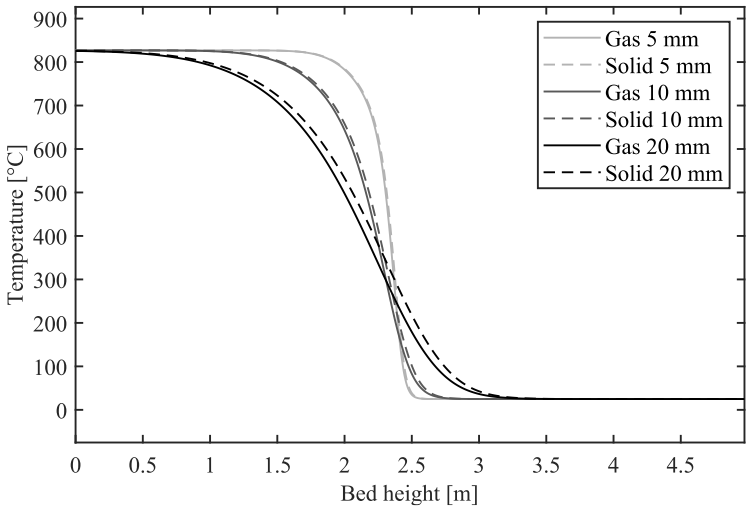

Fig. 4.18: Temperature distributions (HR) for varying particle diameter t=1h (discharge)

Smaller particle diameter leads to a steeper temperature profile, i.e., a narrower temperature front. Moreover, the difference between the solid and fluid temperature noticeably narrows for smaller particles. This is a clear indication of an improved convective heat transfer between fluid and solid. The amount of pumping work increases significantly for small particle sizes. However, the maximum overall efficiency is obtained for the smallest particle diameter, due to the sharper temperature front which allows for the more efficient extraction of the stored energy in the HR.

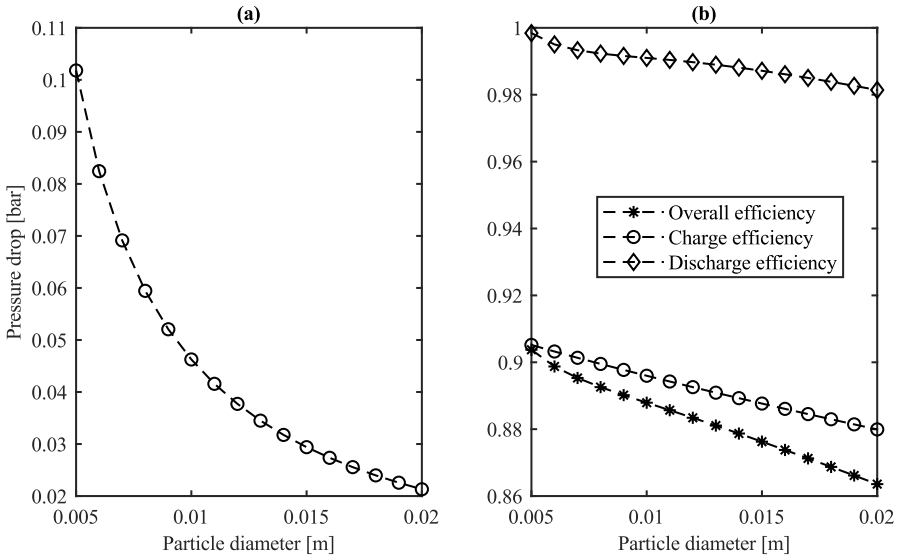

Fig. 4.19: HR pressure drop during discharge and overall efficiency vs. Particle diameter

For the CR, the same trend as the HR is found. The pressure drops are more relevant compared to the one of the HR. Their magnitude is higher, and the thermal energy stored is lower. As for the HR, the discharge efficiency is more penalized than the charge one, which is almost not influenced by the particle diameter since the profile results to steepen enough for a narrow range of $d_{p.}$

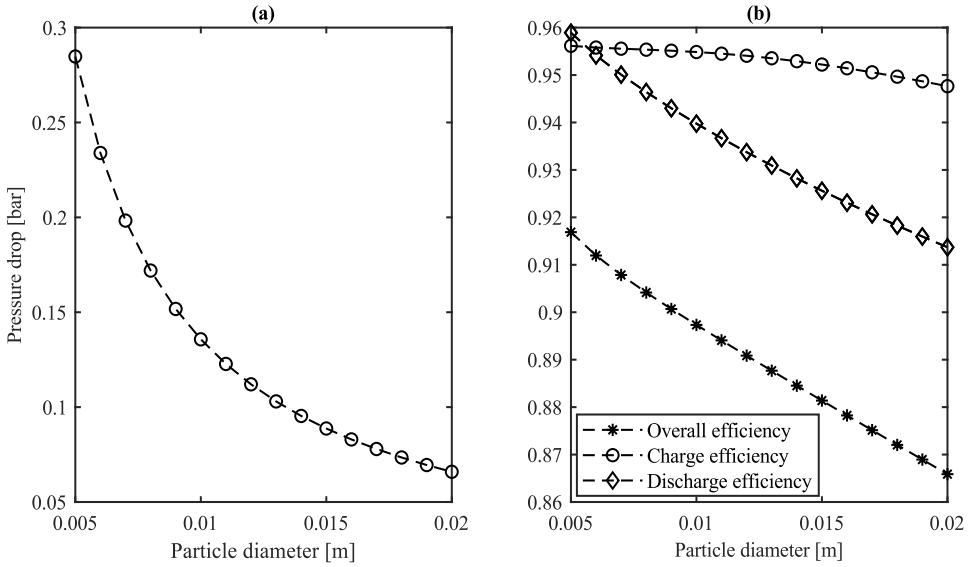

Fig. 4.20: a) CR average pressure drop during discharge vs. Particle diameter b) Thermal efficiencies vs Particle diameter; t_{ch}=5h and t_{disch}=2h

4.5.3 Bed's length to diameter ratio

Fig. 4.21 and Fig. 4.22 show the gas outlet temperature as a function of axial coordinate in the last layer for different storage length to diameter ratio for the HR. Once defined the total volume and the number of tanks, the length of the bed can be determined geometrically, given the diameter for the single bed (cylindrical shape).

$$L_{bed} = \frac{V_{tot}}{N_{tank}\pi\frac{D^2}{4}} \tag{4.37}$$

The temperature of the fluid leaving the last layer in charge mode increases by decreasing the storage height, leading to larger losses at the outlet.

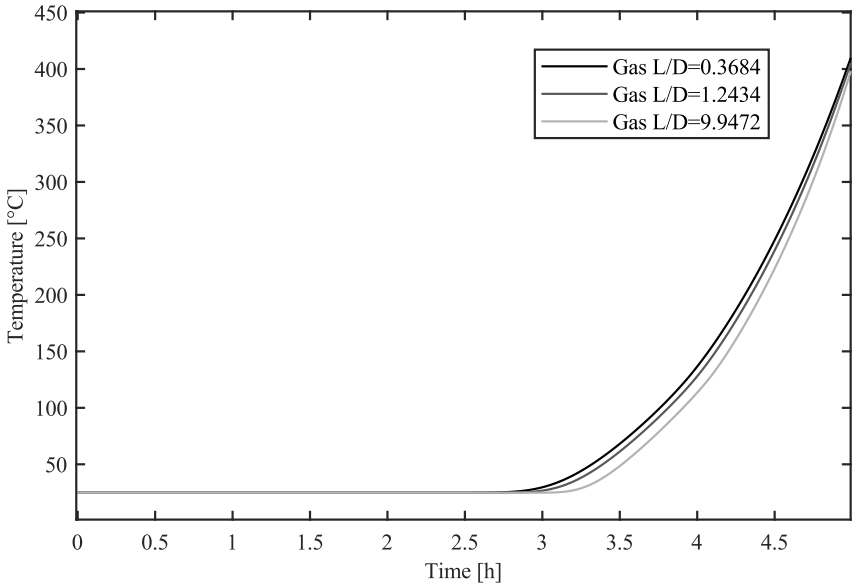

Fig. 4.21: Argon temperature during the charging period as a function of time in the last layer for varying storage height to diameter ratio

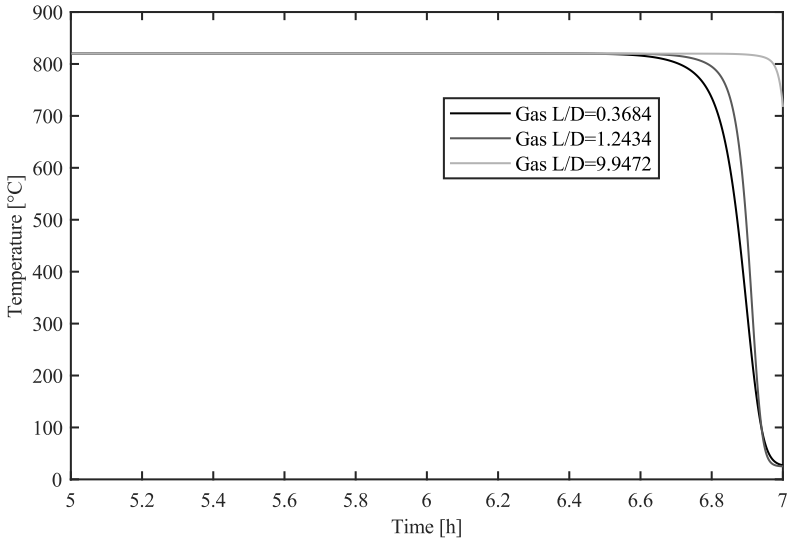

Fig. 4.22: Argon temperature during the discharging period as a function of time in the last layer for varying storage height to diameter ratio

The discharge efficiency rises due to the sharper temperature profile, but the pressure drop inside the tanks become too high if the bed diameter becomes higher than 2.5m. The charging efficiency shows a small increase with tank height, since the exit temperature change is not significant.

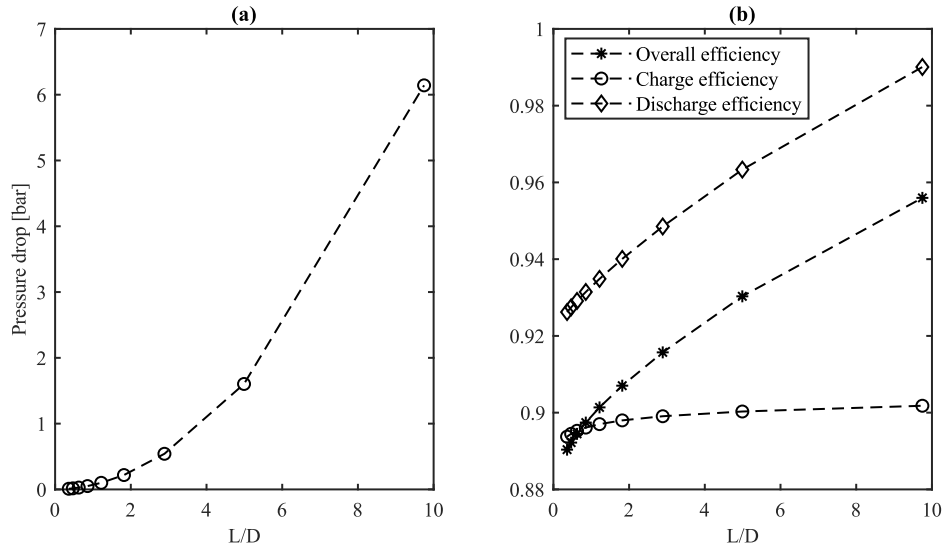

Fig. 4.23: a) HR average pressure drop during discharge vs. L/D b) Thermal efficiencies vs L/D; t_{ch}=5h and t_{disch}=2h

The same considerations that emerged for HR can be associated with CR, but the huge increase of pressure drops makes it impossible to decrease the diameter below 3m, overwhelming the effect of the lower exit losses.

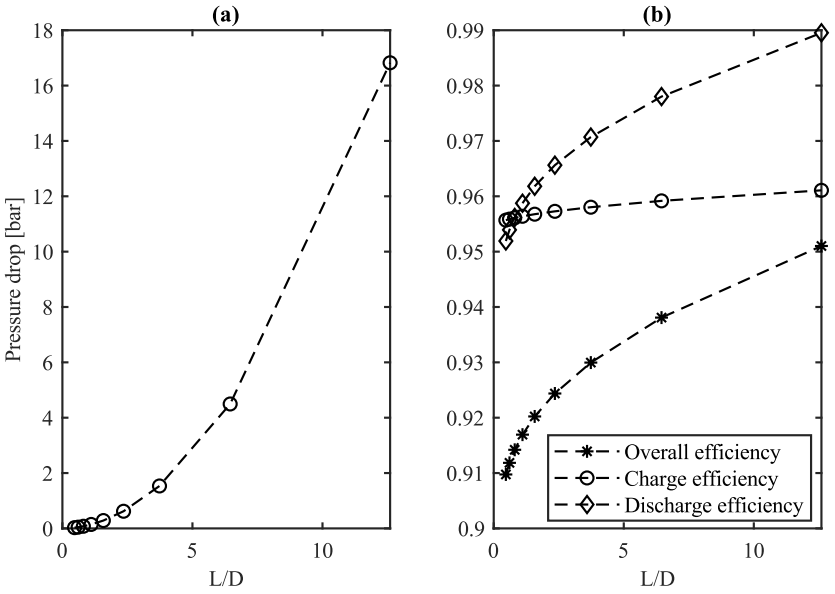

Fig. 4.24: a) CR average pressure drop during discharge vs. L/D b) Thermal efficiencies vs L/D; t_{ch}=5h and t_{disch}=2h

The initial design setup of particle diameter, bed diameter and flow rate are consistent and confirmed by the thermal analysis of the packed bed. The diameter of the bed could be decreased

to increase thermal efficiency in both of the storages, but this change must be verified in terms of effect drop on the RTE of the overall system caused by the increase of pressure drops. A diameter between 3 and 4 m can be the optimal solution for this application in terms of compromise between thermal efficiency and pressure drops.

5 Plant simulation with dynamic heat transfer

In this fifth chapter, the real heat transfer phenomena inside the packed bed is combined with the components of the plant. As far as the real thermocline is considered, a dynamic thermal instability arises during the continuous operation of the plant. When the thermocline exits the bed length, the inlet temperature of the machines varies over time, as depicted in Fig. 5.1.

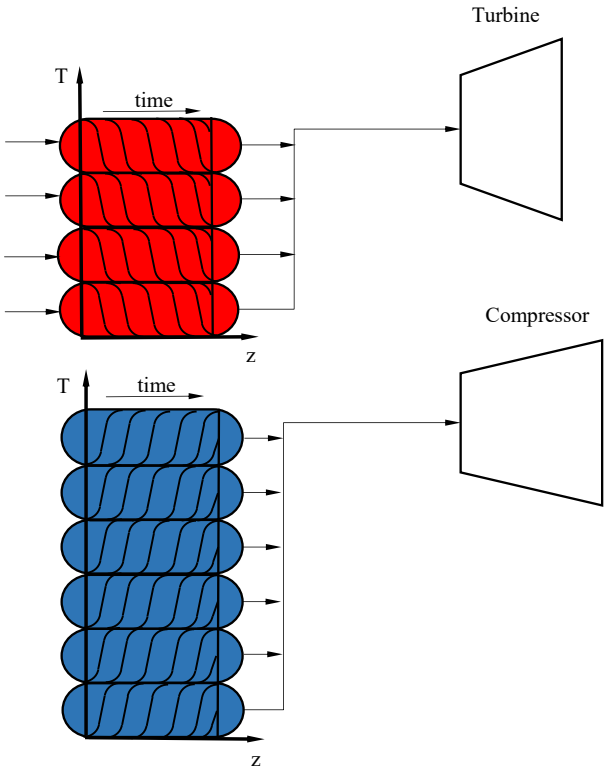

Fig. 5.1: Schematic of the effect of thermocline on machines inlet temperatures during charge

This, combined with the effect of variation in pressure losses and flow rate described in the previous sections, causes a variation of the operating point of the machines, triggering a change

in the pressure ratio and flow rate of the power cycle. The configuration selected for this analysis is the optimized one obtained at the end of the dynamic analysis, so: β_{ch}=20 and β_{disch}=15.75.

5.1 Cyclic effect of thermocline

The outflow temperature from the HR increases continuously after a period of stable state (approximately 3.5 h) during the charging process. The outflow temperature from the CR also has a similar unstable behaviour but the temperature variation trend is opposite to that of the HR. When the thermocline exits the bed height, the inlet, and consequently outlet temperature of the machines will increase, causing the entry of a second thermal front inside the bed, as shown in Fig. 5.2 and Fig. 5.4, increasing the temperature in the primary part of the bed. When the maximum temperature exceeds the design one, the thermal stability of the materials must be verified and controlled during the operation. The charge must be stopped after 4h for two limiting technical reasons: the maximum cycle temperature would exceed 910°C (creating thermal stability problems) and the compressor operating point would reach the pumping limit (Fig. 5.3) if the charge is extended to the nominal 5h.

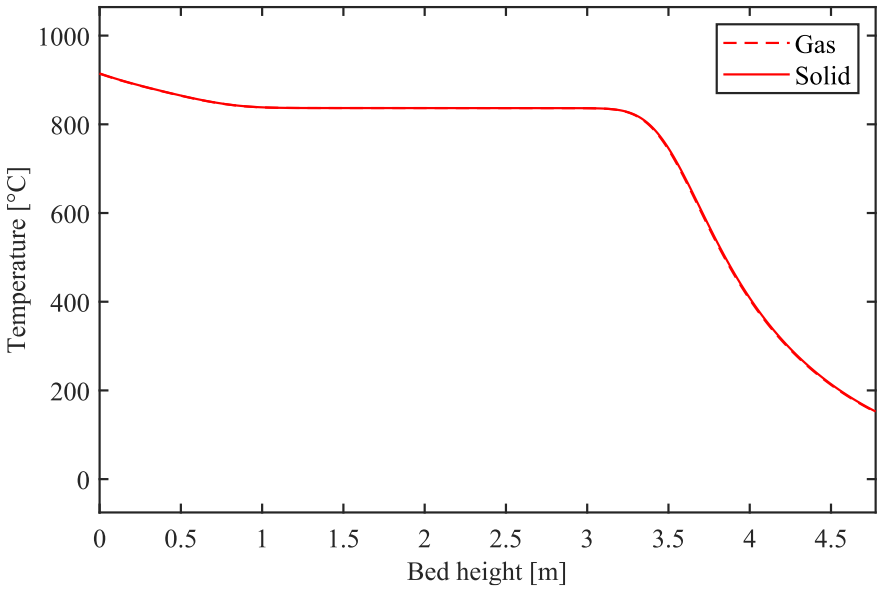

Fig. 5.2: HR temperature profile at the end of 4h considering the real thermal front

Concerning the discharge, after 1.9h the power absorbed by the compressor is higher with respect to the one delivered by the turbine (the two reservoirs are not synchronized) and the discharge phase is stopped, even if the two reservoirs do not reach the initial uniform temperature state of 25°C.

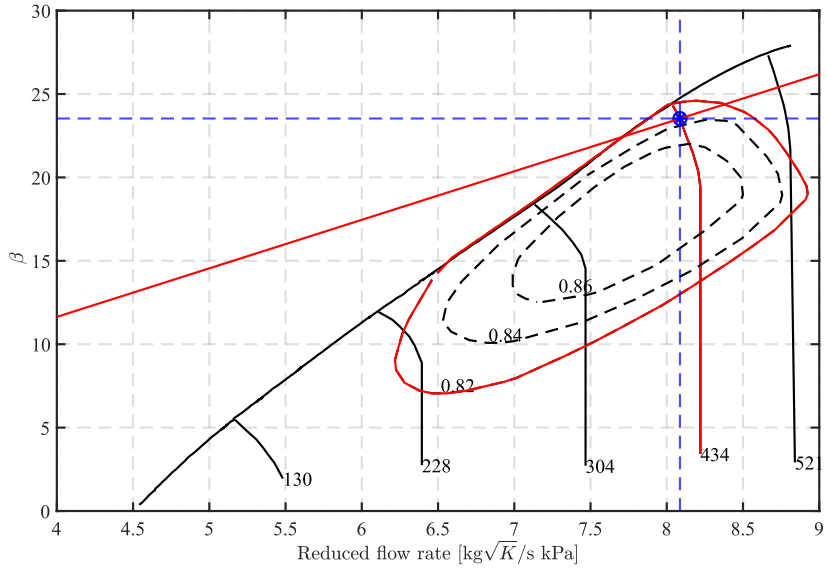

Fig. 5.3: Compressor/turbine operating point after 4h

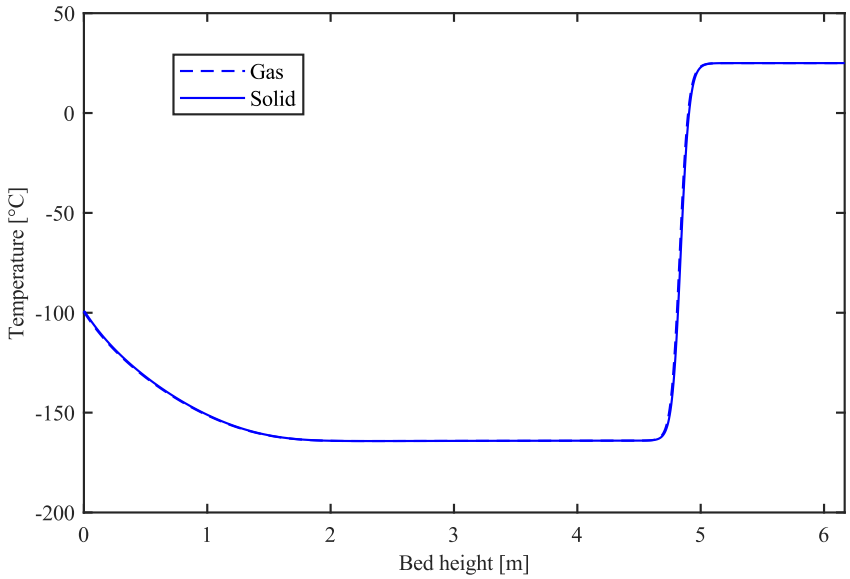

Fig. 5.4: CR temperature profile at the end of 4h considering the real thermal front

This unstable behaviour of the outlet bed temperature will create problems during the delivery phase: first, the machines will experience (both) a decrease in the inlet temperature, until the thermal level in the bed is re-established (Fig. 5.5). Then, when the front leaves the bed length, again the inlet temperature of the compressor/turbine will increase/decrease.

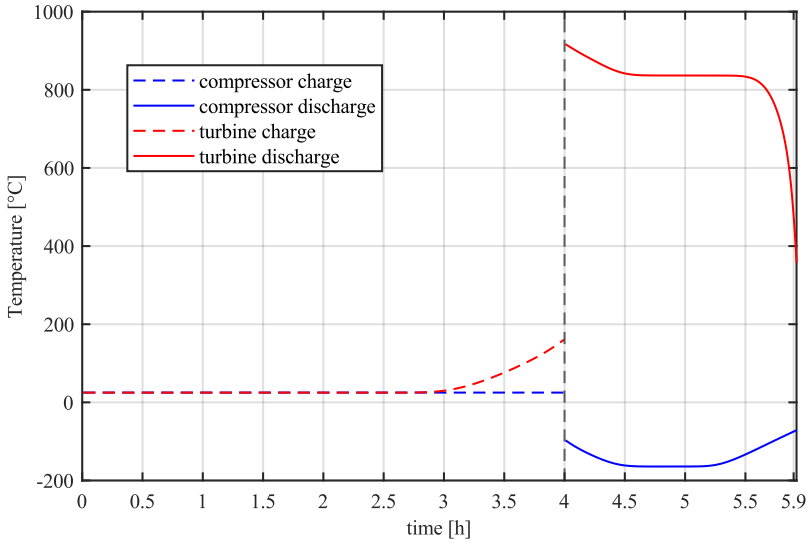

Fig. 5.5: Inlet temperature of the machines over time

This effect influences the operating points in terms of turbine curve and compressor reduced speed, changing over time the operating point and, accordingly, the pressure (Fig. 5.7), flow rate (Fig. 5.6) and power level (Fig. 5.8).

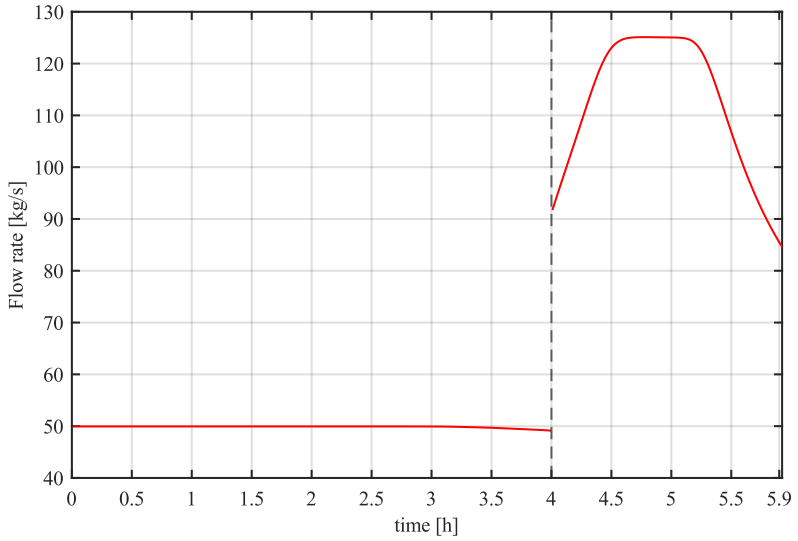

Fig. 5.6: Compressor flow rate over time

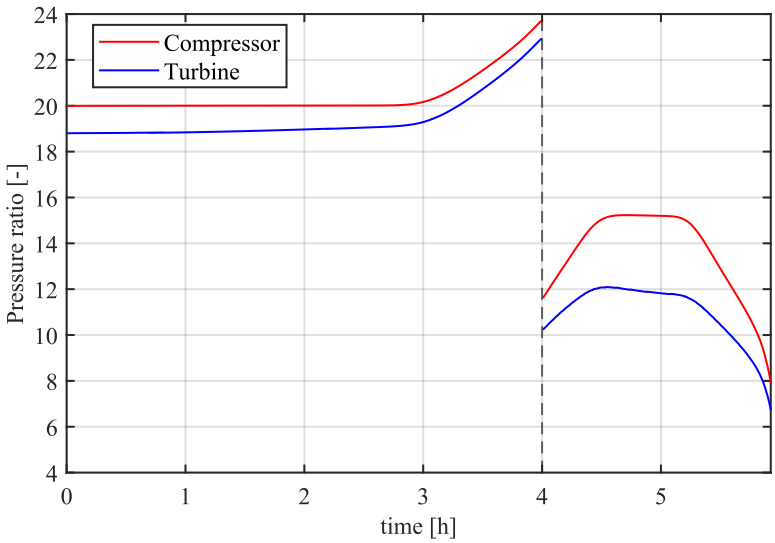

Fig. 5.7: Compression ratio over time

The overall effect is a reduction in RTE, which results 56.3% with a consequent ρE of 51.85 kWh/m^3. Moreover, the increase of the maximum temperature of the cycle must be considered during the design procedure and the cost analysis. Two possible solutions can be applied to mitigate the consequences of the increase in the inlet temperatures of the machines during charge (higher T_{max} and risk of stall in the compressor), which are described in the next two sub-sections.

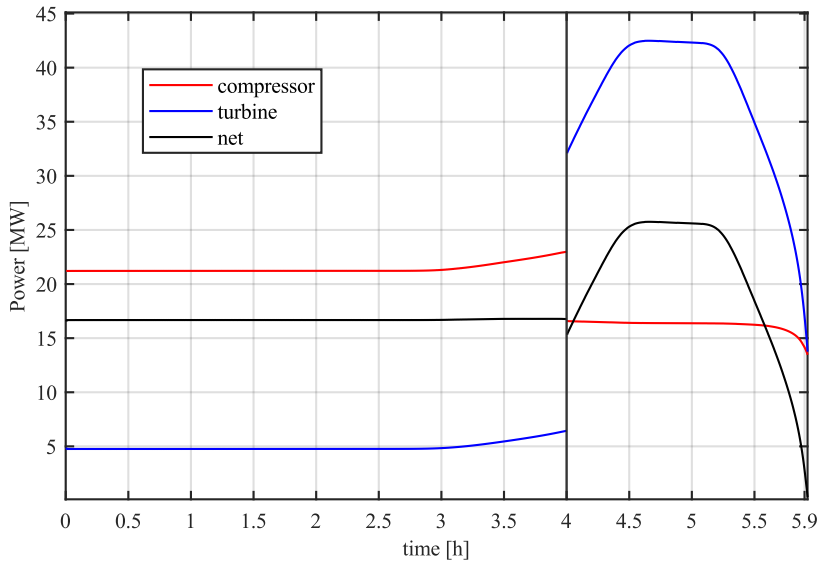

Fig. 5.8: Power level over time

5.2 Possible solutions

5.2.1 Heat exchangers

The two heat exchangers employed to dissipate the heat caused by the irreversibility in the delivery phase can be used to control the outlet gas temperature from the bed also during the first charge period: keeping the system under thermal control and stabilizing the compressor and expander power during charge and the discharge. The effect of the exit of the thermocline during the discharge phase cannot be mitigated and causes a decrease in the power delivery and a consequent decrement of the RTE. The final plant layout during charge is depicted in Fig. 5.9, while the layout during the discharge phase remains unmodified. The time of discharge can be extended to 2.7h, in this way the two beds can potentially reach the initial state before the charge, considering the real thermal front. However, due to the different shapes of the thermoclines during discharge, HR and CR results to be not synchronized. After 2.1h the power absorbed by the compressor is higher with respect to the one delivered by the turbine and the discharge phase is stopped, even if the two reservoirs do not reach the initial uniform temperature state of 25°C.

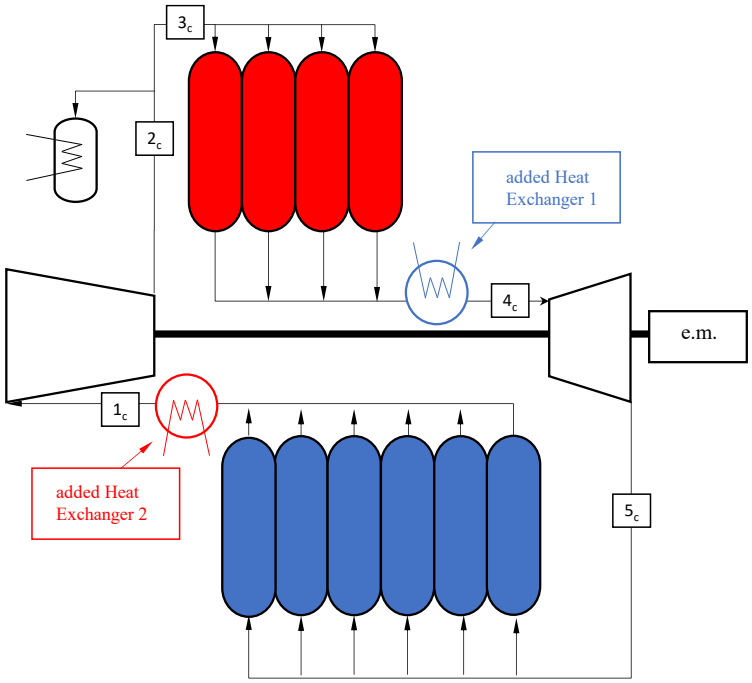

Fig. 5.9: Final plant layout during charge

It can be noticed that the pressure drops, in both CR and HR, show the same trend with respect to the ideal thermal front results, with minor differences regarding the shape of the curves, that are influenced by the real shape of the thermal gradient inside the beds (Fig. 5.10). For the CR, it must be pointed that, when the front comes out form the bed, the pressure drop starts decreasing again, since the flow rate processed by the compressor decreases.

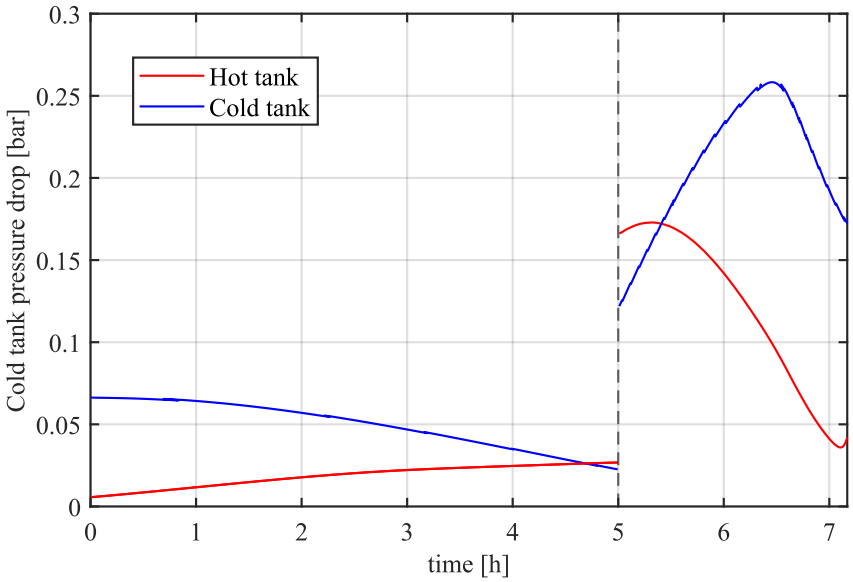

Fig. 5.10: Pressure drops considering the real thermal front

Regarding the compression and expansion ratio (Fig. 5.11), which before were only influenced by pressure drops, now are affected also by the inlet temperature change over time. During the charge phase, compression and expansion ratio are rather stable since the inlet temperatures of the two machines are kept constant by the additional HXs and the only influencing factors are the evolutions over time of the pressure drops and flow rate (Fig. 5.14). The flow rate difference between turbine and compressor is minimal, since the unbalanced flow rate stays always below 0.5 kg/s.

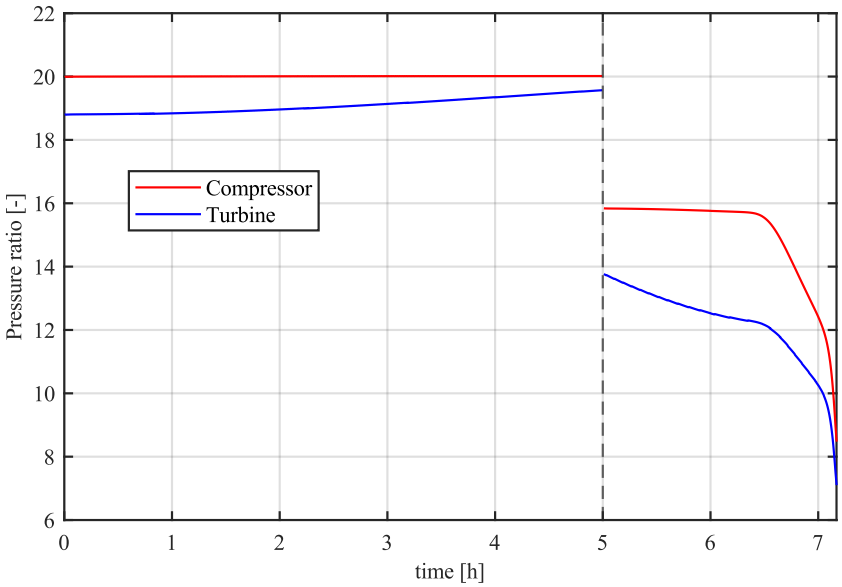

Fig. 5.11: Pressure ratio considering the real thermal front with charge HX

During the delivery phase, as the temperature of the thermocline exits the beds, the TIT will decrease (Fig. 5.12). As the TIT falls, the maximum pressure of the cycle decreases as well as the compression ratio. Meanwhile, the compressor inlet temperature will increase leading to a decrease in the flow rate (Fig. 5.14). The operating point of the compressor and the turbine, after 7.1h, is illustrated in Fig. 5.13.

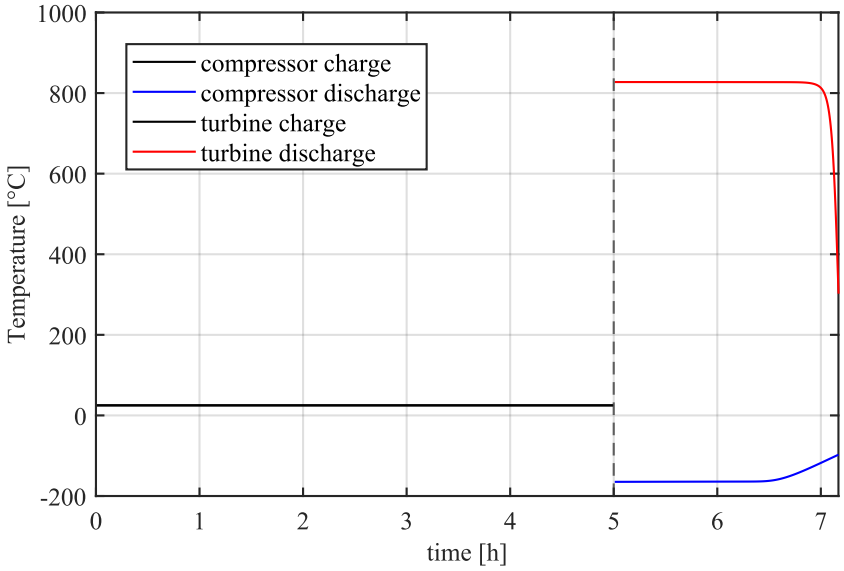

Fig. 5.12: Inlet temperature considering the real thermal front with charge HX

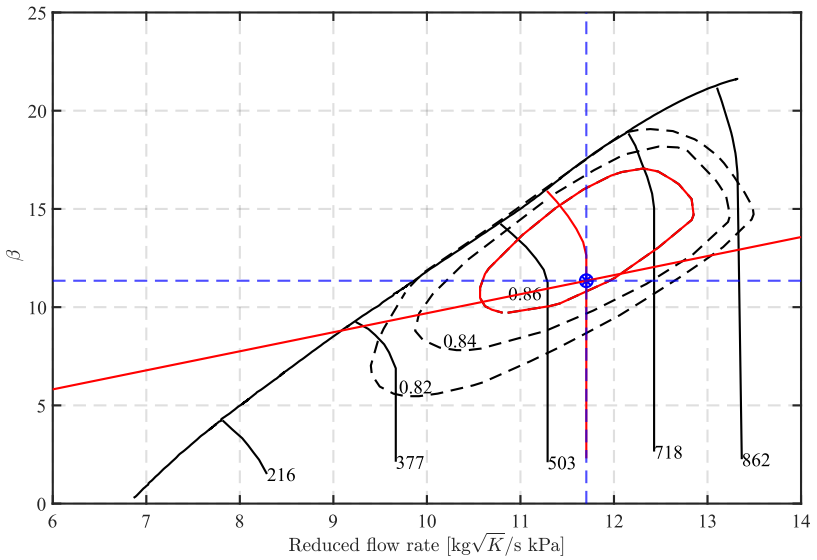

Fig. 5.13: Compressor/turbine matching at the end of discharge

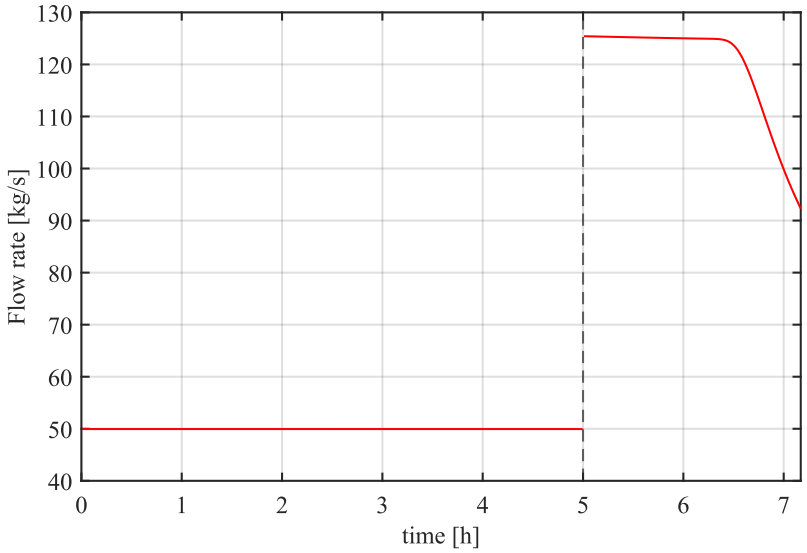

Fig. 5.14: Compressor flow rate over time considering the real thermal front with charge HX

The increase in the compressor inlet temperature combined with the reduction in the thermodynamic quantities at the inlet of the turbine brings the net power delivered into a considerable reduction (Fig. 5.15), affecting the RTE. Since the two storages are not synchronised like the case in which the ideal thermal front is considered, the HR temperature decrease is faster compared to the CRincrease. This leads to a negative net power delivering from 7.1h to 7.5h. In

this case, the discharge must be stopped at 7.1h. Meanwhile, the two tanks can be brought without energy consumption to 25°C. The overall reduction in RTE compared to the case in which no heat exchanger is employed in the charge is lower. A final RTE of 59.86% is achievable, with consequent energy and power density (average) respectively 67.32 kWh/m^3 and 293.16 kJ/m^3.

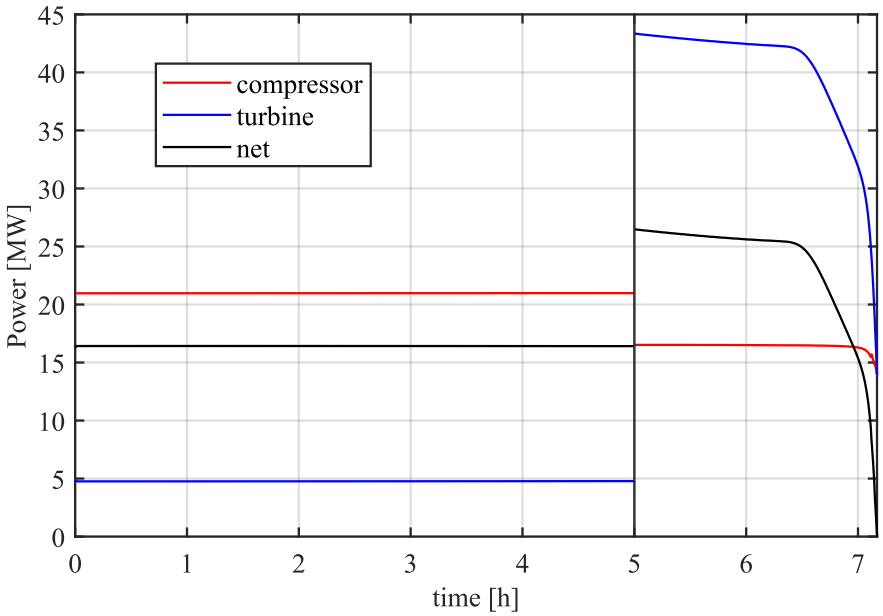

Fig. 5.15: Power levels over time considering the real thermal front with charge HX

The unbalanced flow rate and the total mass in the storage tanks over time are represented in Fig. 5.16 and Fig. 5.17.

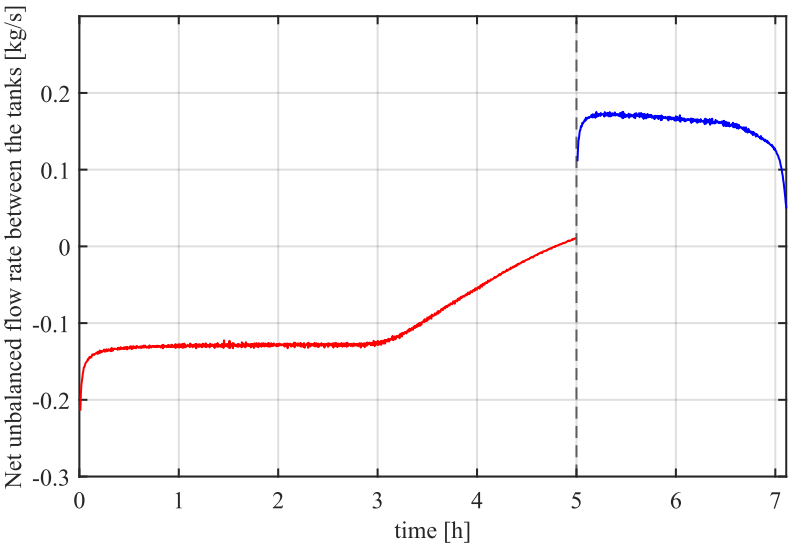

Fig. 5.16: Net unbalanced flow rate over time considering the real thermal front with charge HX

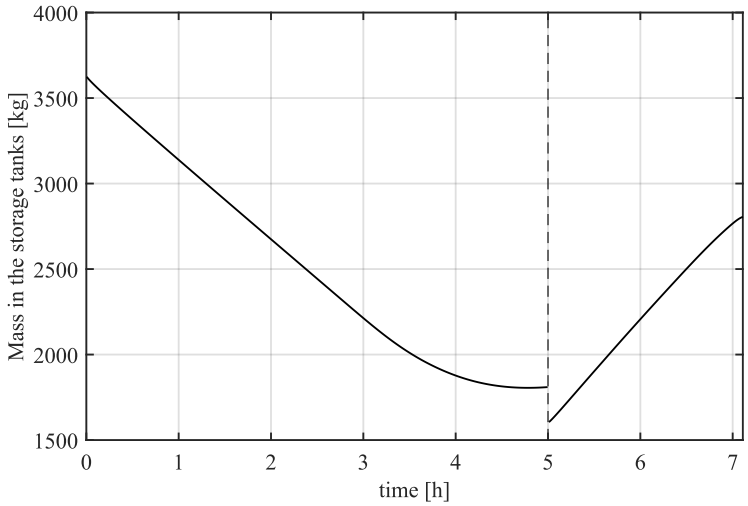

Fig. 5.17: Total mass over time considering the real thermal front with charge HX

5.2.2 Thermocline inside the beds

Another possible solution is to stop the charge and discharge cycle when one of the two thermoclines hits the end of the bed. In this way, both charge and discharge periods will be reduced, but the machines and the overall plant will operate under design conditions virtually all the time. This possible solution would increase the RTE (but would decrease the energy density

at fixed tank volume) with respect to the dissipative solution proposed before, but an additional problem arises: the shape of the two thermoclines differs from HR to CR, so the equilibrium point (when the time of charge/discharge is stopped) may change over time. On a single charge and discharge cycle, this solution would increase the RTE, but over time, the sustainability of the process (charge and discharge) must be verified in terms of the de-stratification of the thermoclines. This may be a good starting point for future studies.

6 Conclusions

This thesis can provide a starting point for the design, dimensioning and optimisation of PTES systems based on the Joule Brayton cycle operating with turbomachines. The results show that these systems certainly promise high energy density (67.32 kWh/m3) around with a fair RTE (59.86%) and power density (293.16 kJ/m^3), considering that they can be scaled virtually to any power and capacity, experiencing economies of scale. Comparisons between technologies should be treated with caution, but it is nonetheless reasonable to conclude that PTES has a very good energy density and a power density, that is not much below that of an industrial gas turbine (the main difference is the maximum cycle temperature difference between a gas turbine and a PTES system). Considering the industrial gas turbine SGT-600 [38] (with a power range comparable with the selected PTES configuration), the specifications are similar to the Argon turbine proposed in the discharge phase for the power generation:

- Power output: 24.5MWe
- Gross efficiency: 33.6%
- Turbine speed: 9500 rpm
- Pressure ratio: 14
- Exhaust mass flow: 81.3 kg/s
- **ρP[10]: 368 kJ/m^3**

However, the dynamic of the PTES storage process is complex and difficult to predict. The results of this thesis aim to develop a starting model to forecast this dynamism and its effects on the performance of the system. The model developed by the author is a flexible code, able to cope with different cycle configurations, exogenous conditions and working fluids, and optimized to sustain one charge and discharge cycle. For future works, the code can be extended to take into

[10] Considering large-scale, heavy-duty machines (up to 590 Mwe), the power density can reach values of 690 kJ/m^3

consideration rests between charge and discharge and multiple cycles, predicting the deterioration of the system over time. The outcomes are the following:

1) A model for the evaluation and optimization of discharge cycle's performance developed in MatlabR2020a®, through the fluid-dynamic turbine-compressor coupling (with relative operating maps), considering the ideal heat exchange inside the beds once fixed the charge design parameters (limited by maximum and minimum operating temperatures). The front progressing affects the matching in terms of change in pressure drops over time as well as the flow rates. With Argon as the working fluid, a compression ratio of 20 is a good limiting value with T_{max}=820 °C and T_{min}=-170 °C, considering reasonable values of turbomachines isentropic efficiencies. With this configuration, the optimal compression ratio during charge of 15.75, as the compression work increases more than the expansion one when the pressure ratio raises. A limiting value of RTE= 62.99% is obtained with the selected configuration.
2) A numerical model developed in MatlabR2020a® to predict the actual behaviour of the thermocline within the beds, in terms of temperature profiles resulting from both charging and discharging periods. The numerical model is validated with experimental data taken from the literature. The code can be used to select an optimal configuration in terms of particle diameter, L/D ratio of the tank and mass flow rate of working fluid. Typically, high flow rates, small particle diameter (1÷5 mm) and high L/D ratios increase the thermal efficiency of the bed. However, this is paid in terms of high-pressure drops, which can decrement the RTE. The optimal compromise must be studied between thermal efficiency and pressure reduction effects on the overall system.
3) The combination of the two models mentioned before accounts for the effect of real thermoclines progression on the system. Without controlling the temperature during the charge period by means of additional heat exchangers, the operation of the system is not sustainable over time: an increase in the maximum temperature is observed. The stability problem of the compressor during charge is critical as well as the power levels during discharge, affected by the heating of the primary zone of the bed at the end of the charge cycle, resulting in RTE=56.3% and ρE=51.85 kWh/m^3. The solution implemented is to add two additional heat exchangers during charge, to stabilise the system for correct and continuous operation over time. H.owever, the different thermal behaviour of the two reservoirs must be taken into account when selecting the discharge time. With this configuration, the RTE, ρE and ρP can be brought respectively to a value of 59.86%, 64.32 kWh/m^3 and 293.16 kJ/m^3. In any case, both RTE and energy density is lower compared to the ideal thermocline model result.

Future developments

Starting from the results of this thesis, future works could involve the analysis of different storage materials, configurations of the power cycle and working fluids, bearing in mind the issues involved. It will be necessary to analyse the system over a long time, with various charge and discharge cycles, choosing their timing in relation to the shapes of the thermoclines. Future studies may also analyse and rearrange the characteristics of the CR and HR to synchronize the two heat fronts over time. Last, a cost analysis may give further incentive towards some configurations over others.

7 Nomenclature

Acronyms

BV	Buffer Vessel
CAES	Compressed Air Energy Storage
CES	Chemical Energy Storage
COP	Coefficient of Performance
CR	Cold Reservoir
CS	Cold Storage
ES	Energy Storage
FBs	Flow Batteries
FES	Flywheels Energy Storage
GES	Compressed Air Energy Storage
HP	High Pressure
HR	Hot Reservoir
HS	Hot Storage
HTC	Heat Transfer Coefficient
HTF	Heat Transfer Fluid
HTGR	High-Temperature Gas cooled Reactors
HX	Heat Exchanger
LAES	Liquid Air Energy Storage
LP	Low Pressure
LPES	Liquid Piston Energy Storage
MES	Mechanical Energy Storage
MM	Molar Mass, kg/kmol
NTU	Number of Thermal Units
PHS	Pumped Hydro Storage
PTES	Pumped Thermal Electricity/Energy Storage
PV	Photovoltaic
RES	Renewable Energy sources
RTE	Round-Trip Efficiency
SMES	Superconducting Magnetic Energy Storage
TES	Thermal Energy Storage
TIT	Turbine Inlet Temperature

VES	Variable Energy Sources
WR	Work Ratio WR=wc/wt

Notation

T	Temperature
$\dot{m}$	Mass flow rate kg/s
$\dot{Q}$	Heat power, kW
$\dot{V}$	Volumetric flow rate, m^3/s
$\dot{W}$	Power, kW
A	Area, m^2
Bi	Biot number, $Bi = \frac{h}{k_s S_v}$
C	Cost
c_p	Specific Heat at Constant Pressure, J/kgK
C_R	Capacity ratio, $C_R = \frac{(\dot{m}c_p)_{min}}{(\dot{m}c_p)_{max}}$
c_s	Specific Heat capacity of the solid material, J/kgK
c_v	Specific Heat at Constant Volume, J/kgK
D	Packed bed diameter, m
d_p	Particle diameter, m
E	Energy, kWh
G	Mass flow rate per unit cross section, $G = \frac{\dot{m}}{A}$
h	Heat transfer coefficient W/m^2K
H	Enthalpy, kJ/kgK
k	Thermal conductivity W/mK
k_{eff}	Effective thermal conductivity W/mK
L	Bed height, m
M	Mass, kg
N	Number of tanks
n	Rotational speed, rpm
nr	Reduced speed, $\frac{n}{\sqrt{T_{T,in}}}$
Nu	Nusselt Number, $Nu = \frac{h\, d_p}{k_g}$
p/P	Pressure
Pr	Prandtl Number, $P_r = \frac{\mu_g c_{p,g}}{k_g}$
P_T	Total pressure
Q	Heat, kWh
R	Gas constant, J/mol K
Re	Reynolds Number, $Re_p = \frac{\rho_g u_s}{d_p}$

Sv	Particle surface-to-volume ratio, $S_v = \frac{6}{d_p}$
t	Time, s
tol	Tollerance
T_T	Total temperature
U	Overall heat transfer coefficient, kW/m^{2}K
u_s	Superficial (empty tube) velocity, $u_s = \frac{\dot{V}}{A}$
V	Volume, m^3
Vn	Nominal speed of the thermal front, $V_n = \frac{\dot{m}\overline{cp_g}}{N_{tank}(1-\varepsilon)\rho_s\overline{c_s}}$
W	Work, kJ/kg
Z	Compressibility factor, pV/nRT
z	Axial coordinate, m

Subscripts

HE	Heat Engine
amb	Ambient
bed	Packed bed
C	Compressor
ch	Charge
disch	Discharge
E/t	Expander/Turbine
el/e	Electric
exp	Expansion
g	Gas
gen	Generator
in	Initial/Inlet
is	Isentropic
max	Maximum
min	Minimum
out	Outlet
rid	reduced
s	Solid
tot	Total
w	Wall
end	End

Greek letters

χ	Round-Trip Efficiency
η	Efficiencies
ρE	Energy Desnity, kWh/m^3
ρP	Power Density kJ/m^3
θ	Cold reservoir temperature ratio when discharged
λ	Isentropic temperature ratio of the compressor
γ	Heat capacity ratio c_p/c_v
ρ_s	Solid density, kg/m^3
ρ_g	Gas density, kg/m^3
ψ	Sphericity, Surface of equivalent sphere / Surface of the particle
ε	Void fraction, Volume occupied by the interstice/ total Volume
β	Compressor pressure ratio
βt	Turbine Expansion ratio
μ	Gas dynamic viscosity, Pa s
ν	Gas kinematic viscosity, cm^2/s
ϑ	Dimensionless temperature, $\vartheta_{g,s} = \left(T_{g,s} - T_{in,s}\right)/\left(T_{in,gas} - T_{in,s}\right)$
Φ	Dimensionless time, $\Phi = \frac{t}{\tau}$
ξ	Dimensionless length, $\xi = \frac{z}{l}$
l	Length scale, $l = \frac{\dot{m}\, c_{p,g}}{hA(1-\epsilon)S_v}$
τ	Time scale, $\tau = \frac{\rho_s c_s}{hS_v}$

8 Bibliography

[1] IEA, “Net Zero by 2050 A Roadmap for the,” p. 222, 2021, [Online]. Available: www.iea.org/t&c/%0Awww.iea.org/t&c/no need for

[2] S. M. Hasnain, “Review on sustainable thermal energy storage technologies, part I: Heat storage materials and techniques,” *Energy Convers. Manag.*, vol. 39, no. 11, pp. 1127–1138, 1998.

[3] S. Øvergaard, “Definition of primary and secondary energy,” *Stand. Int. Energy Classif. Int. Recomm. Energy Stat.*, no. Energy Statistics, pp. 1–7, 2008.

[4] A. Benato and A. Stoppato, “Pumped Thermal Electricity Storage: A technology overview,” *Therm. Sci. Eng. Prog.*, vol. 6, pp. 301–315, 2018,

[5] P. F. Antúnez, “Modelling and development of thermo-mechanical energy storage,” *Dep. Eng.*, vol. Doctor ofP, no. September, 2018.

[6] J. D. McTigue, A. J. White, and C. N. Markides, “Parametric studies and optimisation of pumped thermal electricity storage,” *Appl. Energy*, vol. 137, pp. 800–811, 2015,

[7] A. Smallbone, V. Jülch, R. Wardle, and A. P. Roskilly, “Levelised Cost of Storage for Pumped Heat Energy Storage in comparison with other energy storage technologies,” *Energy Convers. Manag.*, vol. 152, no. May, pp. 221–228, 2017,

[8] D. O. Akinyele and R. K. Rayudu, “Review of energy storage technologies for sustainable power networks,” *Sustain. Energy Technol. Assessments*, vol. 8, pp. 74–91, 2014,

[9] T. C. Allison, “Thermal-Mechanical-Chemical Energy Storage Technology Overview,” 2020.

[10] W. D. Steinmann, H. Jockenhöfer, and D. Bauer, “Thermodynamic Analysis of High-Temperature Carnot Battery Concepts,” *Energy Technol.*, vol. 8, no. 3, 2020,

[11] A. White, G. Parks, and C. N. Markides, “Thermodynamic analysis of pumped thermal electricity storage,” *Appl. Therm. Eng.*, vol. 53, no. 2, pp. 291–298, 2013,

[12] T. Desrues, J. Ruer, P. Marty, and J. F. Fourmigué, “A thermal energy storage process for large scale electric applications,” *Appl. Therm. Eng.*, vol. 30, no. 5, pp. 425–432, 2010,

[13] J. Howes, “Concept and development of a pumped heat electricity storage device,” *Proc. IEEE*, vol. 100, no. 2, pp. 493–503, 2012,

[14] A. Benato, “Performance and cost evaluation of an innovative Pumped Thermal Electricity Storage power system,” *Energy*, vol. 138, pp. 419–436, 2017,

[15] T. R. Davenne and B. M. Peters, “An Analysis of Pumped Thermal Energy Storage With De-coupled Thermal Stores,” *Front. Energy Res.*, vol. 8, no. August, pp. 1–22, 2020,

[16] G. Alva, Y. Lin, and G. Fang, “An overview of thermal energy storage systems,” *Energy*, vol. 144, pp. 341–378, 2018,

[17] L. G. Socacio, “Acta technica napocensis,” *Acta Tech. Napocensis*, vol. 55, no. I, pp. 207–210, 2012.

[18] W. D. Steinmann, *Thermal energy storage systems for concentrating solar power (CSP) technology*. Woodhead Publishing Limited, 2015.

[19] A. J. White, J. D. McTigue, and C. N. Markides, “Analysis and optimisation of packed-bed thermal reservoirs for electricity storage applications,” *Proc. Inst. Mech. Eng. Part A J. Power Energy*, vol. 230, no. 7, pp. 739–754, 2016,

[20] K. Schwaiger *et al.*, “SandTES - An active thermal energy storage system based on the fluidization of powders,” *Energy Procedia*, vol. 49, pp. 983–992, 2014,

[21] M. Mehos *et al.*, “Concentrating Solar Power Gen3 Demonstration Roadmap,” *Nrel/Tp-5500-67464*, no. January, pp. 1–140, 2017,

[22] A. Andel, “Stiesdal,” 2021.

[23] L. Wang, X. Lin, L. Chai, L. Peng, D. Yu, and H. Chen, “Cyclic transient behavior of the Joule–Brayton based pumped heat electricity storage: Modeling and analysis,” *Renew. Sustain. Energy Rev.*, vol. 111, no. October 2018, pp. 523–534, Sep. 2019,

[24] IEA, “The California Duck Curve.” https://www.iea.org/data-and-statistics/charts/the-california-duck-curve

[25] S. Ergun, “Fluid flow through packed columns,” *Chem. Eng. Prog.*, vol. 48, pp. 89–94, 1952.

[26] M. P. Boyce, “Axial-flow Compressors,” *Gas Turbine Eng. Handb.*, p. 163, 2012, [Online]. Available: https://www.netl.doe.gov/sites/default/files/gas-turbine-handbook/2-0.pdf

[27] Z. Tian, C. Wang, and Q. Zheng, “Investigation of the Effects of Different Working Fluids on Compressor Cascade Performance,” *Appl. Sci.*, vol. 11, no. 5, p. 1989, 2021,

[28] Z. Tian, A. Malik, L. Wang, and H. Lu, “Effect of Working Fluid PhysicalProperties on Aerodynamic Performance of Subsonic Axial Compressor Rotor,” 2020.

[29] *Curve Caratteristiche delle Turbomacchine*. p. 1.

[30] M. Valorani, L. Magistrale, and A. Maer, “Corso di Motori Aeronautici,” 2011.

[31] M. Astolfi and E. Macchi, “Efficiency Correlations for Axial Flow Turbines Working With Non-Conventional Fluids,” *Asme Orc 2015*, pp. 1–12, 2015.

[32] G. Nellis and S. Klein, *Heat transfer*. 2009.

[33] A. Meier, C. Winkler, and D. Wuillemin, “Experiment for modelling high temperature rock bed storage,” *Sol. energy Mater.*, vol. 24, no. 1–4, pp. 255–264, 1991.

[34] M. A. Bouhifd, P. Besson, P. Courtial, C. Gérardin, A. Navrotsky, and P. Richet, “Thermochemistry and melting properties of basalt,” *Contrib. to Mineral. Petrol.*,

vol. 153, no. 6, pp. 689–698, 2007,

[35] P. Hartlieb, M. Toifl, F. Kuchar, R. Meisels, and T. Antretter, “Thermo-physical properties of selected hard rocks and their relation to microwave-assisted comminution,” *Miner. Eng.*, vol. 91, pp. 34–41, 2016,

[36] C. G. Maier and K. K. Kelley, “An equation for the representation of high-temperature heat content data1,” *J. Am. Chem. Soc.*, vol. 54, no. 8, pp. 3243–3246, 1932.

[37] L. Wang *et al.*, “Unbalanced mass flow rate of packed bed thermal energy storage and its influence on the Joule-Brayton based Pumped Thermal Electricity Storage,” *Energy Convers. Manag.*, vol. 185, no. December 2018, pp. 593–602, 2019,

[38] Siemens Energy, “Siemens Energy gas turbine portfolio,” 2020, [Online]. Available: https://assets.siemens-energy.com/siemens/assets/api/uuid:a42b9bc4-dc1e-4205-a27e-afa3de31b6f3/familybrochure-gasturbines-sev11-medium144dpi.pdf

[39] K. A. R. Ismail and R. Stuginsky, “Parametric study on possible fixed bed models for pcm and sensible heat storage,” *Appl. Therm. Eng.*, vol. 19, no. 7, pp. 757–788, 1999,

[40] T. Esence, A. Bruch, S. Molina, B. Stutz, and J.-F. Fourmigué, “A review on experience feedback and numerical modeling of packed-bed thermal energy storage systems,” *Sol. Energy*, vol. 153, pp. 628–654, 2017.

[41] T. L. Bergman, F. P. Incropera, D. P. DeWitt, and A. S. Lavine, *Fundamentals of heat and mass transfer*. John Wiley & Sons, 2011.

[42] T. E. W. Schumann, “Heat transfer: a liquid flowing through a porous prism,” *J. Franklin Inst.*, vol. 208, no. 3, pp. 405–416, 1929.

[43] D. Vortmeyer and R. J. Schaefer, “Equivalence of one-and two-phase models for heat transfer processes in packed beds: one dimensional theory,” *Chem. Eng. Sci.*, vol. 29, no. 2, pp. 485–491, 1974.

[44] J. F. Hoffmann, T. Fasquelle, V. Goetz, and X. Py, “A thermocline thermal energy storage system with filler materials for concentrated solar power plants: Experimental data and numerical model sensitivity to different experimental tank scales,” *Appl. Therm. Eng.*, vol. 100, pp. 753–761, 2016,

[45] J. A. Willmott, *Dynamics of regenerative heat transfer*. CRC Press, 2001.

[46] N. Wakao, S. Kaguei, and T. Funazkri, “Effect of fluid dispersion coefficients on particle-to-fluid heat transfer coefficients in packed beds: correlation of Nusselt numbers,” *Chem. Eng. Sci.*, vol. 34, no. 3, pp. 325–336, 1979.

[47] A. J. White, “Loss analysis of thermal reservoirs for electrical energy storage schemes,” *Appl. Energy*, vol. 88, no. 11, pp. 4150–4159, 2011,

[48] J. P. Coutier and E. A. Farber, “Two applications of a numerical approach of heat transfer process within rock beds,” *Sol. Energy*, vol. 29, no. 6, pp. 451–462, 1982.

[49] D. E. Beasley and J. A. Clark, “Transient response of a packed bed for thermal energy storage,” *Int. J. Heat Mass Transf.*, vol. 27, no. 9, pp. 1659–1669, 1984.

[50] M. Hänchen, S. Brückner, and A. Steinfeld, “High-temperature thermal storage using a packed bed of rocks - Heat transfer analysis and experimental validation,” *Appl. Therm. Eng.*, vol. 31, no. 10, pp. 1798–1806, 2011,